

GAS SENSING PROPERTIES OF CeO₂ NANOSTRUCTURES



UNIVERSITY *of the*
WESTERN CAPE

BY

RAMONTSENG KHUNOU

**A thesis submitted in fulfilment of the requirements for the Master's degree in the
Department of Physics, University of the Western Cape**

Supervisor: Dr. G. F. Malgas, University of the Western Cape

Co-supervisor: Prof. D. E. Motaung, University of Limpopo

Date submitted: 13 May 2020

KEYWORDS

Cerium-oxide

Nanoparticles

Nanostructures

Gas sensors

Semiconductor sensor

Sensitivity

Selectivity

Recovery time

Response time

Gas sensing mechanism

Metal oxides



UNIVERSITY *of the*
WESTERN CAPE

ABSTRACT

The industrial safety requirements and environmental pollution have created a high demand to develop gas sensors to monitor combustible and toxic gases. As per specifications of World Health Organization (WHO) and Occupational Safety and Health Administration (OSHA), lengthy exposure to these gases lead to death which can be avoided with early detection. Semiconductor metal oxide (SMO) has been utilized as sensor for several decades. In recent years, there have been extensive investigations of nanoscale semiconductor gas sensor.

In this project, pure cerium oxide (CeO_2) nanostructures was synthesized using a simple hydrothermal method and calcined at various temperatures. The CeO_2 nanostructures were analyzed using different characterization techniques, such as X-ray diffraction, Raman, photoluminescence, electron paramagnetic spectroscopy operating towards various target gases, such as carbon monoxide (CO), methane (CH_4), ethanol and hydrogen sulphide (H_2S), at various gas concentrations ranging from 5 to 100 ppm and various operating temperatures. Our findings exhibited optimizing of the optical, structural, point defects, through annealing has direct influence on the gas sensing properties, such as response, sensitivity, selectivity, and response and recovery times of the CeO_2 based sensor. As a result, the gas sensing characteristics, such as response, sensitivity and selectivity probed towards CO , CH_4 , ethanol and H_2S at different operating temperatures was probed. And among the sensors the CeO_2 annealed at $300\text{ }^\circ\text{C}$ demonstrated improved response and selectivity towards CH_4 at room temperature (i.e. $23\text{ }^\circ\text{C}$). The sensor response was twice higher than other tested gases, justifying superior selectivity. Such response and selectivity were justified by improved point

defects and higher surface area allowing more interaction of oxygen molecules and adsorption of gas molecules on the sensing surface. Thus, these findings elucidate that the current sensor, with its room temperature operation could be useful for low power consumption purpose and such sensor is a striking platform for economic point of view and CH₄ detection.



LIST OF ABBREVIATIONS

HRSEM:	High Resolution Scanning Electron Microscope
HRTEM:	High Resolution Transmission Electron Microscope
EDS:	Energy Dispersive Spectroscopy
XRD:	X-ray Diffraction
SAED:	Selected Area Electron Diffraction
EPR:	Electron spin resonance
PL:	Photolumiscence
XPS:	X-ray photoelectron spectroscopy
BET:	Brunauer-Emmett-Teller
ppm:	Parts Per Million
CO:	Carbon monoxide
CH ₄ :	Methane
IDA:	Interdigitated array
CeO ₂ :	Cerium oxide
MO:	Metal Oxide
MEMS:	Macro- and micro-electromechanical systems
NEMS:	Nanoelectromechanical systems

DECLARATION

I declare that “GAS SENSING PROPERTIES OF CeO₂ NANOSTRUCTURES” is my work, that it has not been submitted for any degree or examination in any other university and that all the resources I have used or quoted have been indicated and acknowledged using complete references.

Full name: Ramontseng Khunou

Date: 13 May 2020

Signed: *R Khunou*



UNIVERSITY *of the*
WESTERN CAPE

ACKNOWLEDGEMENTS

I would like to take this opportunity to thank all the people and organizations that were instrumental in me completing my thesis. Also extremely grateful for all the advice and guidance.

Dr. G. F. Malgas (Department of Physics, University of the Western Cape), for the excellent supervision of this thesis, his guidance, encouragement, for the many stimulating discussions.

Prof. D. E. Motaung, University of Limpopo, who acted as co-supervisor, for his constant encouragement and interest in my progress.

The staff of the Physics Department, University of The Western Cape, for their support and encouragement.

Sponsorship: I would also like to thank the University of the Western Cape and DST together with the Nanoscience program for funding my studies

To my immediate, extended family and friends, for their encouragement and support: My parents and brothers for believing in me, always loving and supporting me.

To God Almighty! Thank you without you nothing is possible

TABLE OF CONTENTS

KEYWORDS	ii
ABSTRACT	iii
LIST OF ABBREVIATIONS	v
DECLARATION	vi
ACKNOWLEDGEMENTS	vii
CHAPTER 1	1
BACKGROUND	1
1.1 INTRODUCTION	1
1.2 AIMS AND THE OUTLINES OF THE THESIS	4
1.3 REFERENCES	6
CHAPTER 2	10
2.1 HISTORY OF GAS SENSOR.....	10
2.2 GAS SENSOR TYPES	11
2.2.1 Calorimetric gas sensors	12
2.2.2 Electrochemical gas sensors	13
2.2.3 Optical gas sensors.....	14
2.2.4 Metal oxide semiconductors gas sensors	15
2.3 METAL OXIDES	16
2.3.1 Tin oxide (SnO ₂).....	16
2.3.2 Zinc oxide (ZnO)	18
2.3.3 Cerium oxide (CeO ₂)	19
2.4 FACTORS AFFECTING THE PERFORMANCE OF MO GAS SENSORS ..	20

2.4.1 Grain size effect	20
2.4.2 Temperature	22
2.5 GAS SENSOR PARAMETERS.....	23
2.5.1 Sensitivity	23
2.5.2 Selectivity	25
2.5.3 Response and recovery times.....	26
2.5.4 Stability	26
2.5.5 Other parameters	27
2.6 MECHANISM FOR GAS SENSING	28
2.7 REFERENCES	30
CHAPTER 3	41
SAMPLE PREPARATION AND ANALYTICAL TECHNIQUES	41
3.1 HYDROTHERMAL TECHNIQUE	41
3.2 CHARACTERIZATION TECHNIQUES	42
3.2.1 Scanning Electron Microscopy	43
3.2.2 Transmission Electron Microscopy	48
3.2.3 X-ray diffraction	48
3.2.4 Raman spectroscopy	54
3.2.5 X-ray photoelectron spectroscopy	56
3.2.6 Photoluminescence spectroscopy.....	58
3.2.7 Brunauer-Emmett-Teller Surface Area Analysis.....	59
3.3.9 Electron paramagnetic resonance spectroscopy.....	60
3.3 REFERENCES	62
CHAPTER 4	66

MORPHOLOGICAL, OPTICAL AND STRUCTURAL PROPERTIES OF CeO₂ NANOPARTICLES	66
4.1 INTRODUCTION	66
4.2 EXPERIMENTAL DETAILS	67
4.3 RESULTS AND DISCUSSION	69
4.4 REFERENCES	84
CHAPTER 5	89
GAS SENSING CHARACTERISTICS OF CeO₂ NANOSTRUCTURES	89
5.1 INTRODUCTION	89
5.2 EXPERIMENTAL DETAILS	90
5.2.1 Synthesis of CeO ₂ nanostructures.....	90
5.2.2 Pt interdigitated electrode.....	90
5.2.3 Depositing of nanoparticles on Pt interdigitated substrates.....	91
5.2.3 Fabrication and testing of the gas sensor.....	91
5.3 RESULTS AND DISCUSSION.....	92
5.3.1 Gas sensor characteristics.....	92
5.3.2. Gas sensing mechanism.....	99
5.4 CONCLUSIONS.....	99
5.5 REFERENCES	101
CHAPTER 6	104
SUMMARY AND FUTURE WORK	104
6.1 SUMMARY	104
6.2 FUTURE WORK.....	105

CHAPTER 1

BACKGROUND

1.1 INTRODUCTION

Rare earth oxides (REO's) have been extensively explored for several cutting-edge applications. Cerium is one of the most plentiful nontoxic elements on the earth. Cerium oxide (CeO_2) has a wide bandgap and has been extensively applied and researched in many fields such as catalysts [1], optics [2], and gas sensors [3] because of its unique properties, arising peculiarly from its 4f shells [4]. For instance, CeO_2 is adopted in three-way catalysts for reducing the emission of the toxic pollutants (CO , NO_x , and hydrocarbons, etc.) from automobile exhaust [5][6], owing to its high oxygen storage capacity, associated with its rich oxygen vacancies and low redox potential between Ce^{3+} and Ce^{4+} [7]. Also, these properties have made it a suitable candidate for sensing material as the operational process of a semiconducting metal oxide gas sensors (SMO) based on changes in resistance upon exposure to reducing or oxidizing gases [8][9]. SMO's are widely used for the detection of various combustible and lethal gases such as methane (CH_4) and carbon monoxide (CO).

The industrial safety requirements and environmental pollution have generated a high request to develop gas sensors for monitoring combustible and toxic gases. As per the specifications of the World Health Organization (WHO) and Occupational Safety and Health Administration (OSHA), lengthy exposure to these gases leads to death toll which can be avoided [10]. CH_4 and CO fall into a group of inert gases that are odorless, colorless, non-irritating, and tasteless. Exposure at a concentration below 800 ppm can lead to dizziness,

headache, or loss of judgment, above that higher health risk, such as convulsions and nausea, are possible. Thus, it is necessary to develop sensors for the detection of these toxic gases at room temperature, below the acceptable exposure limit, with fast alarming feedback [11].

A great deal of investigation has been completed into developing different categories of gas sensors such as catalytic combustion [12], optical fiber [13], and electrochemical sensors [14]. There is a broad range of applications for these gas sensors to be applied in any field. The progress of semiconductor based sensors have fascinated a great number of researchers [15]. The key attention with MOs in terms of gas-sensing studies is the necessity of their electrical conductivity on the ambient gas [16]. Most MOs semiconductors are naturally of n-type conductivity due to the existence of a huge number of oxygen vacancies [17]. When such a material is exposed to gas which is under detection, oxygen molecules are adsorbed at the grain boundaries, then collect electrons from the conduction band to generate a space charge layer between the grains [18]. This leads to the creation of Schottky barriers at the surfaces of the grains and increases the resistivity of the material [19]. Exposure of the material to reducing gases such as CO causes a reaction of these toxic gases with the adsorbed oxygen, increasing the electronic conduction and reducing the resistance [20]. The sensing properties are based on surface reactions and are significantly affected by the microstructure of the material [21].

During the last decade, many efforts have been carried out to overcome the disadvantages of metal oxide sensors by improving stability, selectivity, and sensitivity [18][22]. The fabrication of fast-responding sensitive gas sensors with high selectivity is the subject of continuous investigation, boosted by strategies based on nanotechnology [23]. The synthesis of one dimensional nanostructures has gained considerable attention in the gas-sensing study,

mostly due to their high surface area to volume ratio, which generates highly active surfaces [24]. Additionally, metal oxide nanostructures have been reported to display new and improved functions relative to the bulk oxide as a result of the quantization effect, which leads to unique chemical and physical properties [25]. To improve the gas-sensing performance of metal oxide nanostructures, additives are often added into the base metal oxides to form nanocomposites.

Despite some achievement in this area, there are still many disadvantages concerning the synthesis, structure, and fundamental understanding of metal oxide gas sensors [26]. Problems in terms of synthesis include the use of difficult synthesis procedures, expensive and toxic chemicals and lack of morphology control. The change from bulk to nanostructure materials, particularly one-dimensional (1D) structures also means that the gas-sensing mechanism becomes more difficult because structural parameters such as particle size, the surface availability for the exposed analytes and stability, need to be considered [27]. It is well recognized that nanostructured materials have larger surface areas, than bulk materials because of their very tiny size combined with high aspect ratio. Thus, the chemical reactivity is extremely strengthened [28]. Thus, searching for sensor materials with tailored properties requires systematic studies. Therefore, gas sensors based on 1D nanostructures may be important to open the way to discover cheap, but high performing, stable gas sensors [29]. In this work, we develop CeO₂ sensor for detection of CO and CH₄ at ambient operating temperatures.

1.2 AIMS AND THE OUTLINES OF THE THESIS

The focus of this research is to synthesize and fabricate a gas sensor based on CeO₂ nanostructures and their superior selectivity towards CH₄, among other interfering gases, such as ethanol, CO, H₂S and CH₄ gases at room temperature. To achieve the goal of this study, the following have to be done:

- Synthesis of the CeO₂ nanoparticles using an inorganic precursor such as cerium nitrate hexahydrate and sodium hydroxide.
- To study the effect of calcination temperatures on the phase transformation of CeO₂.
- Characterize the synthesized CeO₂ nanostructures with analytical techniques such as X-ray diffraction (XRD), High resolution scanning electron microscopy (HRSEM), high-resolution transmission electron microscopy (HRTEM), energy dispersive spectroscopy (EDS), Raman spectroscopy, X-ray photoelectron spectroscopy (XPS), Photoluminescence (PL) and Electron spin resonance (EPR).
- Fabricate the device on interdigitated electrodes.
- Testing of the device for their sensitivity towards CO, H₂S, ethanol and CH₄ gases.
- Study the electrical resistance and gas response mechanism of nanocrystalline CeO₂ films in a wide operating temperature range.
- Develop various ways to improve the sensitivity of metal oxide gas sensors, e.g. by calcination of the CeO₂ nanoparticles at different temperatures.

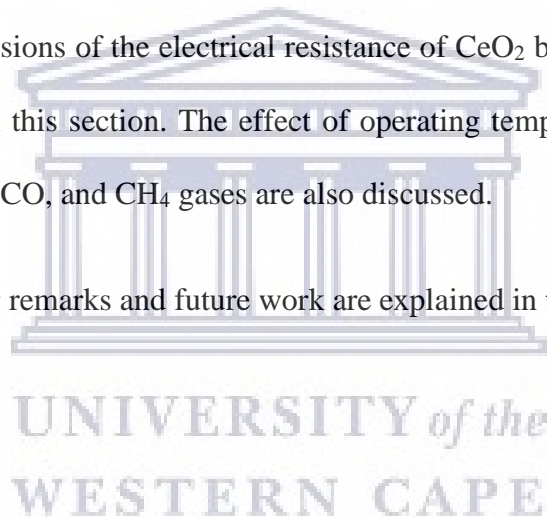
Chapter 2: Provides an in-depth review of the various aspects of gas sensors including the types of gas sensors, the types of metal oxides used in gas sensors, the principle operation of gas-sensors, and its parameters.

Chapter 3: Explain in detail the experimental methods for synthesizing CeO₂. Analytical techniques that were used to characterize synthesized CeO₂ nanomaterials are also presented in this section.

Chapter 4: Results obtained from different analytical techniques used in this study are discussed in this section.

Chapter 5: Detailed discussions of the electrical resistance of CeO₂ based gas sensor exposed to CO and CH₄ gas are in this section. The effect of operating temperature on gas response behaviour is discussed for CO, and CH₄ gases are also discussed.

Chapter 6: The concluding remarks and future work are explained in this section.



1.3 REFERENCES

- [1] Avgouropoulos, G. and Ioannides, T., 2003. Selective CO oxidation over CuO-CeO₂ catalysts prepared via the urea–nitrate combustion method. *Applied Catalysis A: General*, 244(1), pp.155-167.
- [2] Orel, Z.C. and Orel, B., 1994. Optical properties of pure CeO₂ and mixed CeO₂/SnO₂ thin film coatings. *physica status solidi (b)*, 186(1), pp. K33-K36.
- [3] Liao, L., Mai, H.X., Yuan, Q., Lu, H.B., Li, J.C., Liu, C., Yan, C.H., Shen, Z.X. and Yu, T., 2008. Single CeO₂ nanowire gas sensor supported with Pt nanocrystals: gas sensitivity, surface bond states, and chemical mechanism. *The Journal of Physical Chemistry C*, 112(24), pp.9061-9065.
- [4] Hirano, M. and Kato, E., 1996. Hydrothermal synthesis of cerium (IV) oxide. *Journal of the American Ceramic Society*, 79(3), pp.777-780.
- [5] Kašpar, J., Fornasiero, P. and Graziani, M., 1999. Use of CeO₂-based oxides in the three-way catalysis. *Catalysis Today*, 50, pp.285-298.
- [6] Trovarelli, A. and Fornasiero, P. eds., 2013. *Catalysis by ceria and related materials* (Vol. 12). World Scientific.
- [7] Liu, B., Li, C., Zhang, G., Yao, X., Chuang, S.S. and Li, Z., 2018. Oxygen vacancy promoting dimethyl carbonate synthesis from CO₂ and methanol over Zr-doped CeO₂ nanorods. *ACS Catalysis*, 8, pp.10446-10456.
- [8] Liangyuan, C., Shouli, B., Guojun, Z., Dianqing, L., Aifan, C. and Liu, C.C., 2008.

- Synthesis of ZnO–SnO₂ nanocomposites by microemulsion and sensing properties for NO₂. *Sensors and Actuators B: Chemical*, 134, pp.360-366.
- [9] Tang, H., Yan, M., Zhang, H., Li, S., Ma, X., Wang, M. and Yang, D., 2006. A selective NH₃ gas sensor based on Fe₂O₃–ZnO nanocomposites at room temperature. *Sensors and Actuators B: Chemical*, 114, pp.910-915.
- [10] Majumder, D. and Roy, S., 2018. Development of low-ppm CO sensors using pristine CeO₂ nanospheres with high surface area. *ACS omega*, 3, pp.4433-4440.
- [11] Krzyzanowski, M., 2008. WHO air quality guidelines for Europe. *Journal of Toxicology and Environmental Health, Part A*, 71, pp.47-50.
- [12] Han, C.H., Hong, D.W., Han, S.D., Gwak, J. and Singh, K.C., 2007. Catalytic combustion type hydrogen gas sensor using TiO₂ and UV-LED. *Sensors and Actuators B: Chemical*, 125, pp.224-228.
- [13] Arregui, F.J., Claus, R.O. and Cooper, K.L., 2001. Optical fiber gas sensor based on self-assembled gratings. *Journal of lightwave technology*, 19, p.1932.
- [14] Mhlongo, G.H., Motaung, D.E. and Swart, H.C., 2015. Pd²⁺ doped ZnO nanostructures: Structural, luminescence and gas sensing properties. *Materials Letters*, 160, pp.200-205.
- [15] Seiyama, T., Kato, A., Fujiishi, K. and Nagatani, M., 1962. A new detector for gaseous components using semiconductive thin films. *Analytical Chemistry*, 34, pp.1502-1503.
- [16] Sankar, C., Ponnuswamy, V., Manickam, M., Suresh, R., Mariappan, R. and Vinod,

- P.S., 2017. Structural, morphological, optical and gas sensing properties of pure and Ce doped SnO₂ thin films prepared by jet nebulizer spray pyrolysis (JNSP) technique. *Journal of Materials Science: Materials in Electronics*, 28, pp.4577-4585.
- [17] Chiodelli, G., Flor, G. and Scagliotti, M., 1996. Electrical properties of the ZrO₂-CeO₂ system. *Solid State Ionics*, 91, pp.109-121.
- [18] Kim, I.J., Do Han, S., Singh, I., Lee, H.D. and Wang, J.S., 2005. Sensitivity enhancement for CO gas detection using a SnO₂-CeO₂-PdO_x system. *Sensors and Actuators B: Chemical*, 107, pp.825-830.
- [19] Khodadadi, A., Mohajerzadeh, S.S., Mortazavi, Y. and Miri, A.M., 2001. Cerium oxide/SnO₂-based semiconductor gas sensors with improved sensitivity to CO. *Sensors and Actuators B: Chemical*, 80, pp.267-271.
- [20] Pourfayaz, F., Khodadadi, A., Mortazavi, Y. and Mohajerzadeh, S.S., 2005. CeO₂ doped SnO₂ sensor selective to ethanol in presence of CO, LPG and CH₄. *Sensors and Actuators B: Chemical*, 108, pp.172-176.
- [21] Barreca, D., Comini, E., Ferrucci, A.P., Gasparotto, A., Maccato, C., Maragno, C., Sberveglieri, G. and Tondello, E., 2007. First example of ZnO- TiO₂ nanocomposites by chemical vapor deposition: structure, morphology, composition, and gas sensing performances. *Chemistry of Materials*, 19, pp.5642-5649.
- [22] Devi, G.S., Manorama, S. and Rao, V.J., 1995. High sensitivity and selectivity of an SnO₂ sensor to H₂S at around 100° C. *Sensors and Actuators B: Chemical*, 28, pp.31-37.

- [23] Zhang, J., Liu, X., Neri, G. and Pinna, N., 2016. Nanostructured materials for room-temperature gas sensors. *Advanced Materials*, 28, pp.795-831.
- [24] Wang, C., Yin, L., Zhang, L., Xiang, D. and Gao, R., 2010. Metal oxide gas sensors: sensitivity and influencing factors. *Sensors*, 10, pp.2088-2106.
- [25] Shipway, A.N., Katz, E. and Willner, I., 2000. Nanoparticle arrays on surfaces for electronic, optical, and sensor applications. *ChemPhysChem*, 1, pp.18-52.
- [26] Wang, Z.L., 2004. Zinc oxide nanostructures: growth, properties and applications. *Journal of physics: condensed matter*, 16(25), p. R829.
- [27] Vander Wal, R.L., Hunter, G.W., Xu, J.C., Kulis, M.J., Berger, G.M. and Ticich, T.M., 2009. Metal-oxide nanostructure and gas-sensing performance. *Sensors and Actuators B: Chemical*, 138(1), pp.113-119.
- [28] Kumar, E., Selvarajan, P. and Muthuraj, D., 2013. Synthesis and characterization of CeO₂ nanocrystals by solvothermal route. *Materials Research*, 16(2), pp.269-276.
- [29] Gangopadhyay, S., Frolov, D.D., Masunov, A.E. and Seal, S., 2014. Structure and properties of cerium oxides in bulk and nanoparticulate forms. *Journal of Alloys and compounds*, 584, pp.199-208.

CHAPTER 2

LITERATURE REVIEW

2.1 HISTORY OF GAS SENSOR

The first catalytic combustion gas sensor was developed in the early 1920s, which was later commercialized in 1923. This particular gas sensor used a single platinum wire heated to high temperatures to enable stable reaction with the analyte gases [1]. The operating process is simply to measure the resistance change resulting from the rise in temperature from gas sensing. An improved catalytic combustion gas sensor using a catalyst of palladium was introduced in the form of a bead. However, such a sensor was mostly used by professional experts working in quite limited fields [2].

In the 1960s there was enormous demand for highly sensitive, low-cost domestic gas sensors following the liquefied petroleum (LP) gas (popularly used for heating and cooking) bottle explosions in Japan [3]. Seiyama *et al.* reported on the first semiconductor gas sensor in 1962 [4][5], shortly after Taguchi proposed the use of semiconducting oxides as sensing materials for the detection of inflammable gases such as LPG [6]. This is because these oxides displayed a significant increase in conductivity at high temperatures. Taguchi and his colleagues later successfully developed the commercial production of semiconductor gas sensors based on tin oxide in 1968 [7].

Later on, they succeeded in optimizing the sensitivity of these sensors further by annealing the sensing material which increased the porosity of the material and rising the operating temperature [8]. Since then, many investigations have been carried out to find new ways of enhancing the sensitivity of the commercial sensor or to search for new types of

semiconducting oxide materials, and to gain further understanding of their sensing mechanisms [9].

The development of other sensors, such as oxygen and humidity sensors, are as a result of the success of semiconductor gas sensors. For example, an oxygen gas sensor is based on the findings of Wagner, and Kiukolla was developed using a stabilized zirconia electrolyte which measures the standard free energy of the formation of metal oxides or the activity of oxygen in molten metals. The original idea for this sensor comes from the findings of Kiukolla and Wagner [10]. They demonstrated the dependency of the electromotive force of (EMF) an electrochemical cell based on stabilized zirconia electrolyte on the oxygen partial pressure at high temperatures [11].

Humidity sensors have been widely used in many various industrial applications including fibre processing, electronic materials, precision instruments, and food monitoring, and also in many domestic devices such as air conditioners. In 1976, the market for humidity sensor 10 was stimulated by the release of electronic ovens equipped with a ceramic humidity sensor by Matsusita Electric Industrial Co. for automated cooking [12]. This kind of humidity sensor utilized a porous composite metal oxide which varied its AC impedance according to the change in humidity at high temperature. Gas sensor technology is continually being improved with the discoveries in nanostructures, nanocomposites, conductive polymers, and many other sensing materials.

2.2 GAS SENSOR TYPES

Gas sensors are devices that can change the concentration of an analyte gas into an electronic signal [13] and are an important component of devices commonly known as “electric noses”

[14]. Based on the operating principles/mechanisms of the transducer, gas sensors can be categorized into several different classes.

2.2.1 Calorimetric gas sensors

Calorimetric gas sensors also known as “pellistors” detect the concentration of a combustible gas by measuring the change in the temperature of a heated catalytically active element after being exposed to a mixture of combustible gas (e.g. CH₄) and air [15]. The design of a calorimetric gas sensor consists of bare coiled shape platinum (Pt) wire heated at high temperatures (900-1000°C) to allow the sensor to react with the gases at a sufficiently high and stable rate[16]. Such design, however, generates many problems including high evaporation rate and softening of the Pt wire which alters its original coil shape, ultimately resulting in poor zero and span quality of the sensor as well significant reduction in the operating life of the sensor[17][18]. However, over the years many improvements have been made to the design of these sensors including coating the Pt wire with non-catalytically active metal and treating the finished sensors with a suitable catalyst such as platinum, palladium (Pd), or thoria (Th) compounds, to reduce the temperature needed to achieve stable signal for hydrocarbon gases from 900-1000 °C to 450-600 °C[19]. A schematic diagram of a Pellistor-type catalytic gas sensor is illustrated in Figure 2.1.

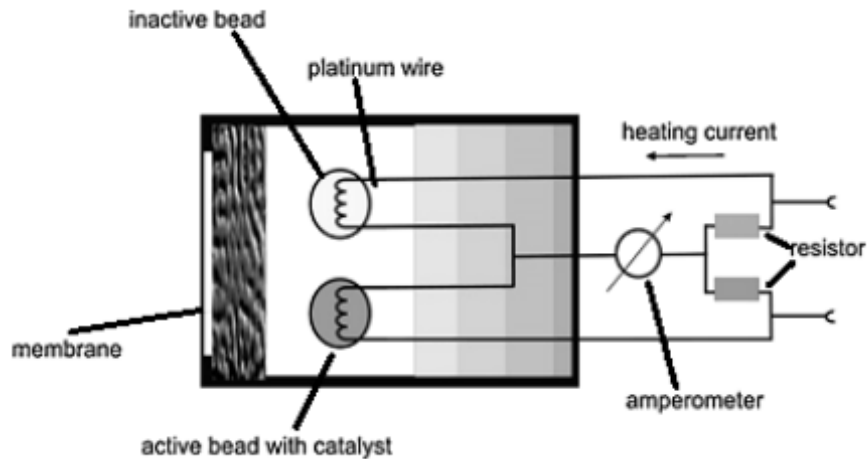


Figure 2.1: Schematic diagram of a Pellistor-type gas sensor [20].

2.2.2 Electrochemical gas sensors

Electrochemical gas sensors determine the gas concentration by oxidizing or reducing the target gas at the electrode and measuring the resulting current [21]. The typical components of these sensors include reference electrodes (anode and cathode), electrolytes, and gas permeable membranes. Figure 2.2 shows a schematic diagram of an electrochemical gas sensor illustrating all the components [22]. Electrochemical gas sensors require very little power to operate and are widely used in confined space. They are particularly suited for the reliable and selective detection of O_2 . Major drawbacks of these sensors include short operating life (1-3 years) and the relatively poor capability to detect gases that are not electrochemically active [23].

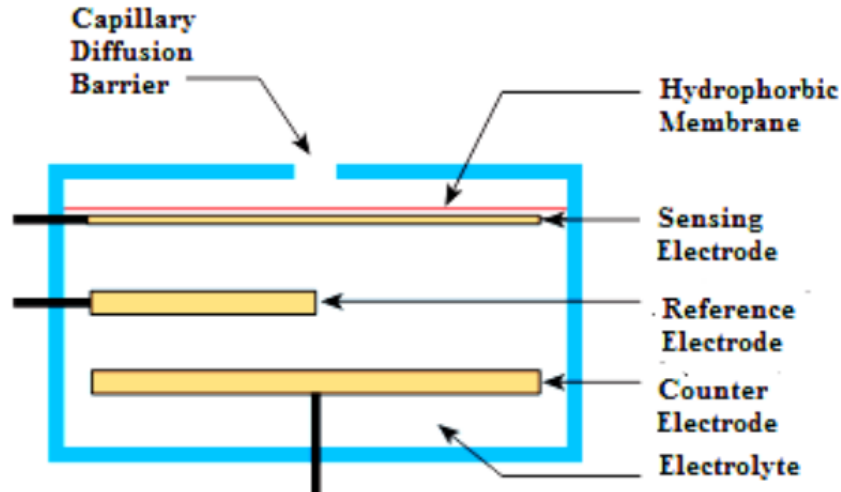


Figure 2.2: A schematic diagram electrochemical gas sensor [24].

2.2.3 Optical gas sensors

Optical gas sensors detect the concentration of the target gas by measuring the changes in optical properties as a result of the interaction between the sensing material and the analyte gas [25]. For example, one type of optical gas sensor measures the change in surface plasmon resonance (SPR) signals which are related to the refractive index close to the sensor surface, allowing for the measurement of bound gas molecules [26]. Another type of optical gas sensor measure is the optode; which measures gas concentration by relying on the changes in optical properties such as luminescence, reflection, absorbance, light polarization, etc [27]. A typical arrangement of an optical gas sensor consists of a laser diode and a very sensitive HgCdTe infrared (IR) detector. Optical gas sensors have high selectivity and specificity due to the unique features of the IR absorption of each gas. However, they are rather expensive owing to the high cost of the laser source and the IR detector, and they are also difficult to be packed in a portable device [28].

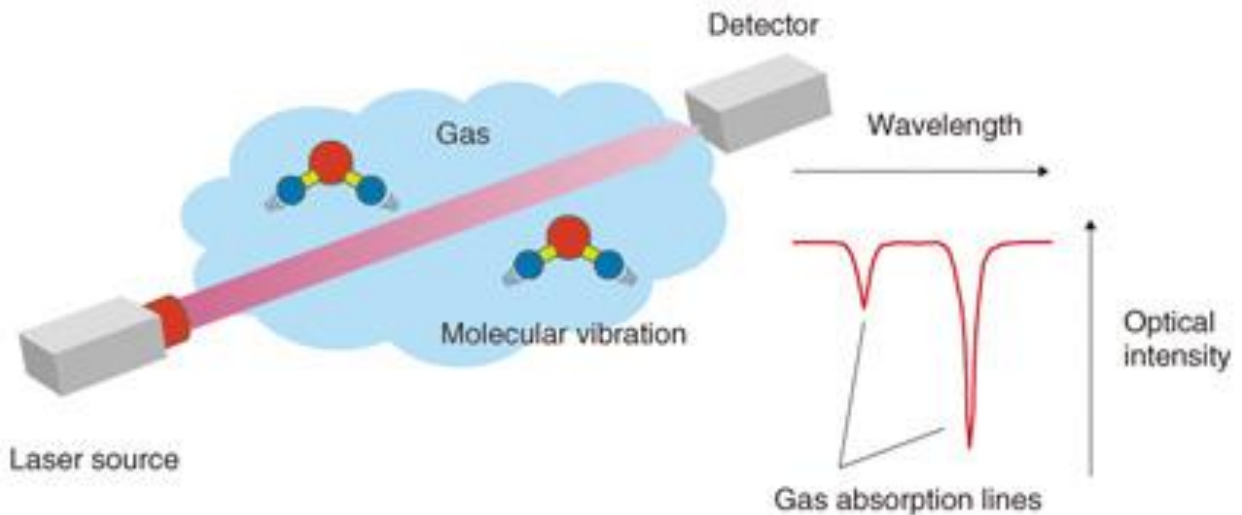


Figure 2.3: A schematic diagram of a laser-based trace gas sensor.[29]

2.2.4 Metal oxide semiconductors gas sensors

These sensors are made by an interdigitated electrode with a sensing material to bridge the gap between the two electrodes [30]. There are numerous types of sensing materials that have chemiresistive properties such as metal-oxide semiconductors, etc. [31][32][33].

The use of metal oxide semiconductors in gas sensors can be traced back to 1953 when Brattein and Bardeen [34] observed the change in electrical resistance of germanium (Ge) when impurities are present on its surface. This effect was later observed for ZnO by Seiyama et al., who noted a significant increase in adsorption and desorption processes on the surface of zinc oxide (ZnO) at high temperatures (near 400 °C), allowing for the detection of gaseous compounds. Through the pioneering works of Taguchi and Seiyama, the first chemiresistive gas sensor was developed based on SnO₂ and released commercially in 1968 for the detection of inflammable and reducing gases such as liquefied propane (LP).

These early metal-oxide based sensors, however, often suffer from problems such as long response time, cross-sensitivity, sensitivity to humidity and poor long-term stability [35].

Since then, many studies have been carried out on SnO₂ along with other metal oxides to address these issues and a substantial increase in the understanding of the sensing mechanism of metal oxide has been developed. However, up until now many semiconducting metal oxide-based sensors still frequently suffer from poor selectivity and high operating temperatures. Despite these issues, they remain the most commercially successful gas sensors owing to their ease of processing and fabrication, reliable performance, and cheap manufacturing cost.

2.3 METAL OXIDES

Metal oxides have been the subject of numerous investigations in gas-sensing research for more than three decades, with many of the early research primarily focused on the tin oxide. In the last two decades, however, the focus has shifted to other promising metal oxide materials and their composites.

The advantages of using metal oxides as gas sensor materials include simplicity in device structure, low fabrication cost, robustness in practical applications, and adaptability to a wide variety of reducing and oxidizing gases [36]. The gas detection method using semiconducting metal oxides is largely based on the change in their electrical resistance caused by the adsorption and reactions of oxidizing and reducing gaseous species. The final resistance of the sensor will be highly influenced by the gas atmosphere and the operating temperature.

2.3.1 Tin oxide (SnO₂)

Tin oxide has a tetragonal crystal structure, with lattice parameters, $a = 0.4734$ nm and $c = 0.3185$ nm[37]. Each unit cell of SnO₂ is assembled of two tin atoms and four oxygen atoms,

with the octahedral sharing edges and forming linear chains along the *c*-axis. In its intrinsic form, SnO₂ is an *n*-type semiconductor with a wide band-gap (E_g of ~3.4 eV). The main natural growth facets of SnO₂ are (100) and (110) planes [38]. Thermodynamically, the surface of the (110) plane of SnO₂ is the most stable, largely because of the bridging of oxygen ions lying above the main surface plane, which can be easily removed by either heating the material to high temperatures or by high energy particle bombardment [39].

Among the semiconducting metal oxides, SnO₂ has been the most popular material in gas-sensing research as well as in commercial gas-sensors. The advantages of SnO₂ include low cost, high sensitivities to various gases, and can be miniaturized for possible integration into micromachined substrates. Different morphologies of SnO₂ nanostructures have been reported and tested for the detection of ethanol [40][41], acetone [42], H₂ [43], CO [44], etc. Although these pure SnO₂ sensors may exhibit high sensitivity toward such gases, they tend to suffer from poor selectivity, as they often detect a range of gases rather than just a single specific gas. So to address such issue, usually metal or metal oxide additives are implemented into the material (i.e. the combination of these materials is often referred to as nanocomposites), to induce electronic and chemical sensitization.

Although the addition of dopants to the SnO₂ nanomaterials have been shown to improve their sensitivity and/or recovery and recovery times, the optimum operating temperatures of many additive-modified SnO₂ gas sensors are still relatively high. Therefore, more research should be carried out on the search for the appropriate additive materials to SnO₂ gas sensors to further decrease their operating temperatures[45].

2.3.2 Zinc oxide (ZnO)

In most cases, zinc oxide has a hexagonal crystal structure with lattice parameters $a = 0.3253$ nm, and $c = 0.5213$ nm [46]. The structure of hexagonal wurtzite ZnO consists of several alternating planes of tetrahedrally arranged O^{2-} and Zn^{2+} , stacked along the c -axis. The oppositely charged ions result in positively charged Zn-(0001) and negatively charged O-(0001), which subsequently give rise to normal dipole moment and spontaneous polarization along the c -axis, along with a divergence in surface energy. In its pure form, ZnO is a wide bandgap ($E_g \sim 3.3$ eV) n -type semiconductor exhibiting various unique properties, including piezoelectricity, and room-temperature luminescence [47].

ZnO has three possible growth directions: $\langle 2110 \rangle$ ($\pm[2110], \pm[1210], \pm[1120]$), $\langle 0110 \rangle$ ($\pm[0110], \pm[1010], \pm[1100]$) and $\pm[0001]$ [48]. Different morphologies of ZnO can be grown by tuning the growth rates along with these directions, and therefore, it is important to consider the relative surface activities of the various facets under the given reaction conditions [49]. As each crystal has varying kinetic parameters for different crystal planes, one can obtain a specific morphology of ZnO, by controlling the growth conditions of these planes. ZnO is one of the most popular materials for gas-sensing applications next to SnO_2 [50]. Their use as a gas sensor which relied on surface conductivity changes in response to adsorbed gases made them an ideal candidate in the early days of surface science. Point defects on ZnO surfaces can produce very large changes in their surface conductivity. These changes typically occur at the surface of the grains as a result of charge transfer and band bending caused by the adsorbates. O vacancies are the dominant defects identified in these films and are usually created by high-temperature treatment of the ZnO films [51]. In its pure form, ZnO has been used for the detection of various gases. However, ZnO-based sensors

often suffer from problems such as poor long-term stability, high operating temperatures, and sensitivity to ambient humidity, and poor selectivity. By adding certain impurities it is possible to lower the detection temperature to around 200 °C [52].

2.3.3 Cerium oxide (CeO₂)

CeO₂ is a rare earth oxide of cerium that is a pale yellowish colour. The unique chemical, physical and optical properties have created significant attention in the research community. MOs have oxygen deficiency, oxygen storage capacity, and electron conductivity [53]. Furthermore, with a bandgap of ≈ 3.2 eV and its extremely efficient UV absorber, it also has a high refractive index with a sharp absorption edge [54]. Resulting in a wide variety of application in many areas such as fuel cells [55], catalysis [56], biomedical [57], nanobiology and nanomedicine [58], etc. sensitive materials are coated with it to protect from corrosion.

Figure 2.4 illustrates the cubic (fluorite) structure of CeO₂ with the cubic unit cell depicting how the coordination of cerium (big spheres) is a cubic arrangement of eight oxide ions (small spheres) [56]. CeO₂ crystallizes in a face-centered cubic (FCC) structure with a space group of Fm-3m. The F.C.C. unit cell consists of cations and anions that occupy the octahedral interstitial sites. Each cerium cation (Ce⁴⁺) is coordinated by eight nearest-neighbour oxygen anions (O²⁻). Four nearest neighbour cerium cations coordinate each of these oxygen anions in turn [59]. The positions of the cerium and oxygen atoms are at the 4a 0, 0, 0 and 8c $\frac{1}{4}, \frac{1}{4}, \frac{1}{4}$ sites respectively in a cubic fluorite structure. It has a lattice constant of 5.410 Å at room temperature [57].

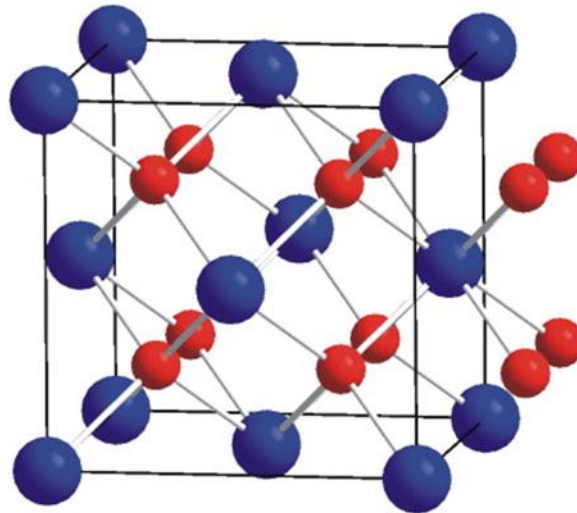


Figure 2.4: The unit cell of CeO_2 the big balls and the small balls represent cerium and oxygen respectively [55].

Cerium oxide also exhibit excellent adhesion, high thermal shock resistance [60], and no apparent aging under changing gas compositions and at temperatures between 700-1100 °C. Doping with SnO_2 can enhance the sensitivity to H_2S at low temperatures (7-127 °C) [61]. Mixing with BaCO_3 and CuO can enhance the sensitivity to CO_2 in the temperature range of 550-600 °C. Doping with Pt or TiO_2 can improve the sensing activity to gases such as O_2 and CO [62].

2.4 FACTORS AFFECTING THE PERFORMANCE OF MO GAS SENSORS

2.4.1 Grain size effect

Numerous papers report the “small size effect” of MOS [63][64][65]. Figure 2.5, shows a sensor and the sensing particles being compacted as if connected to their neighbours. Those interconnected particles form larger aggregates that are connected to their neighbours by grain boundaries [66]. Xu et al. explain this by a semi-quantitative model. Basically, on the

surface of the grains, adsorbed oxygen molecules extract electrons from the conduction band and trap the electrons at the surface in the form of ions, which produces a band bending and an electron depleted region called the space-charge layer. When the particle size of the sensing film is close to or less than double the thickness of the space-charge layer, the sensitivity of the sensor will increase remarkably [67].

Three different cases can be distinguished according to the relationship between the particle size (D) and the width of the space-charge layer (L) that is produced around the surface of the crystallites due to chemisorbed ions [68][69].

- When $D \gg 2L$, the inner mobile charge carriers are responsible for the conductivity of the entire structure. The electrical conductivity is determined from the barrier height. It is not responsive to the charges acquired from surface reactions.
- When $D \geq 2L$, the conductivity not only depends on the particle boundaries barriers but also the cross-section area of those channels and so it is responsive to reaction charges. Therefore, the particles are sensitive to ambient gas composition.
- When $D < 2L$, the entire particle is surrounded by the space-charge layer and there is depletion of mobile charge carriers in the crystallites. Which then, flattens the energy bands throughout the entire structure of the interconnected grains. Thus, conductivity is controlled by the intercrystallite conductivity since there is essentially no boundaries.

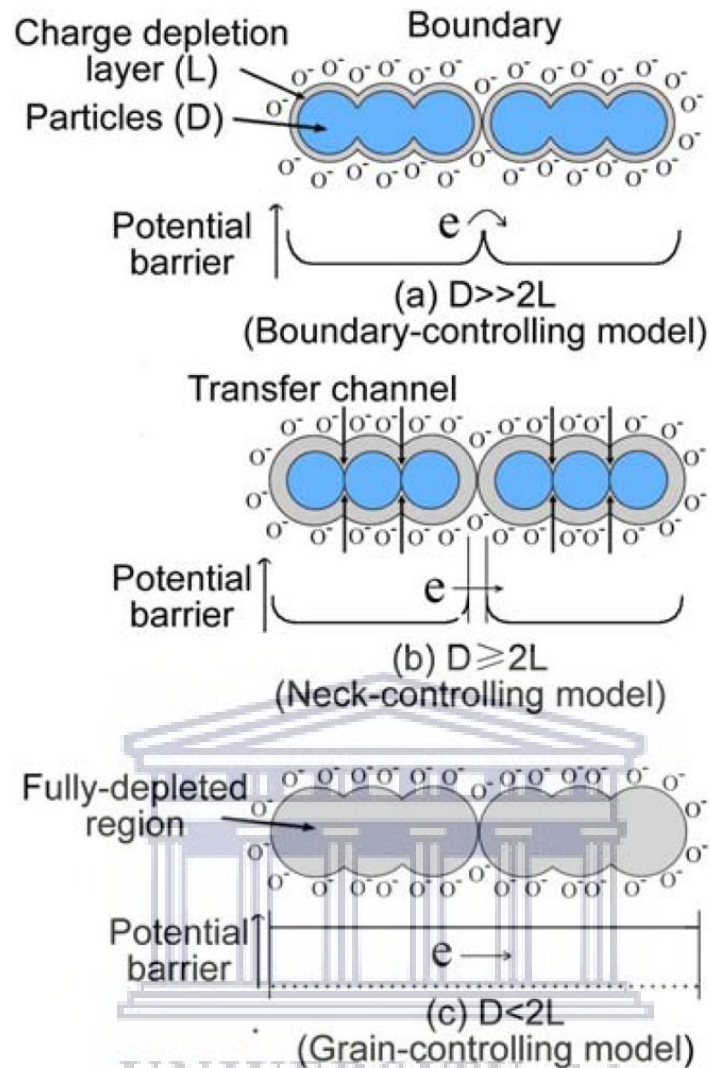


Figure 2.5: Schematic model of the effect of the crystallite size on the sensitivity of metal-oxide gas sensors: (a) $D \gg 2L$; (b) $D \geq 2L$; $D < 2L$ [70].

2.4.2 Temperature

Temperature is an important factor that affects the sensitivity of a chemiresistive gas sensor. The absorption and desorption of oxygen, as well as gas molecules, are highly influenced by the operating temperature, and therefore, it also affects the active properties of the sensors (response and recovery times) which depend exponentially on the operating temperature [71].

Different characteristics may be observed with varying temperatures, chemical decomposition [72], surface coverage [73], co-adsorption, and other reactions are temperature-dependent processes [74]. Apart from chemical effects, there is also a change in the physical properties attributed to the temperature of the semiconducting metal oxides, including the charge-carrier concentration [75], the Debye length, and the work function [76]. For example, at higher temperatures, the concentration of the charge carriers is higher, and therefore, the conductivity of the oxide material is increased. However, at very high temperatures, the Debye length tends to decrease and this may have contributed to the decreasing sensitivity of some metal oxide sensors at higher temperatures. At low temperatures, most gas sensor materials, including metal oxides are insulators rather than semiconductors.

2.5 GAS SENSOR PARAMETERS

The performance of a gas sensor is quantified by its sensing parameters such as sensitivity, selectivity, and reversibility of its sensing response. Scientists have been done extensive research to develop sensing materials to meet the growing demand for selective, stable, and reliable, sensitive, portable, and low-powered sensors.

2.5.1 Sensitivity

The change in electrical resistance of a metal oxide gas sensor (i.e. whether it decreases/increases) when exposed to an analyte gas largely depends on the type of gas (reducing or oxidizing) and the nature of the semiconducting oxide material (n-type or p-type) [77]. In an n-type semiconductor, the charge carriers are electrons. Hence, when exposed to air, oxygen molecules capture electrons from the conduction band of the n-type

oxide sensing material, creating a depletion layer [78]. Subsequently, when exposed to an analyte gas, for example, a reducing gas (e.g. CO, H₂), the reducing gas molecules interact with the adsorbed oxygen, releasing the trapped electrons back into the conduction band of the n-type oxide sensing material[79]. This increases the density of charge carriers, producing a decrease in resistance of the sensor.

In comparison, for a p-type semiconductor, the charge carriers are holes. Thus, when O₂ molecules adsorb on the surface of the metal oxide, they still capture electrons from the conduction band of the material; however, this increases the density of charge carriers (holes) and ultimately decreases its resistance in air. However, upon exposure to a reducing gas, the resistance of the material increases [80]. The complete opposite behaviour will occur, if the analyte gas is an oxidizing gas, i.e. the resistance increases for an n-type semiconductor and decreases for a p-type semiconductor, as summarized in Table 2.1.

Table 2.1. The dependency of the resistance behaviours of semiconducting gas-sensors on the nature of the semiconducting oxide sensing material and the type of gases.

Type of gases	n-type	p-type
Reducing gases	Resistance decreases	Resistance increases
Oxidizing gases	Resistance increases	Resistance decreases

The sensitivity (S) of a metal oxide gas sensor is determined by measuring the change in electrical resistance of the sensor as a result of the interaction between the analyte gas and the metal oxide surface. The sensitivity of a metal oxide gas sensor is typically expressed as the

ratio of the resistance measured in air to the resistance measured in the gas atmosphere for n-type semiconductors or vice versa for p-type semiconductors:

$$S = \frac{R_a}{R_g} \quad \text{for n-type semiconductor} \quad 2.1$$

$$S = \frac{R_g}{R_a} \quad \text{for p-type semiconductor} \quad 2.2$$

A high S value indicates the good sensing capability of the tested metal oxide gas sensor toward a particular analyte gas. Alternatively, sensitivity can also be measured in terms of percentage:

$$S(\%) = 100 \times \left[\frac{R_g - R_a}{R_a} \right] \quad \text{for n-type semiconductor} \quad 2.3$$

A positive value indicates that the resistance of the film decreases upon exposure to the gas and vice versa.

2.5.2 Selectivity

Selectivity is defined as the ability of the sensor to selectively detect a single analyte gas or a group of analyte gases. Selectivity toward a single particular gas is highly desirable, however, in most cases, metal oxide gas sensors tend to detect a group of analytes rather than just a single analyte. The selectivity (Q) of a metal oxide gas sensor can be approximated:

$$Q = \frac{\text{sensitivity of the sensor toward interfering gases}}{\text{sensitivity toward the desired gas}} \quad 2.4$$

2.5.3 Response and recovery times

The response time (τ_{res}) of a gas sensor is commonly defined as the time needed to reach 90% of the saturation resistance of the sensor after being exposed to a target gas (Figure 2.6). On the contrary, the recovery time (τ_{rec}) refers to the time needed by the sensor to return to 10% of its initial resistance after being exposed to air. Short response and recovery time are highly desirable properties in a gas sensor, to enable quick detection of the target gas and the subsequent recovery after the gas has been successfully detected [81][82].

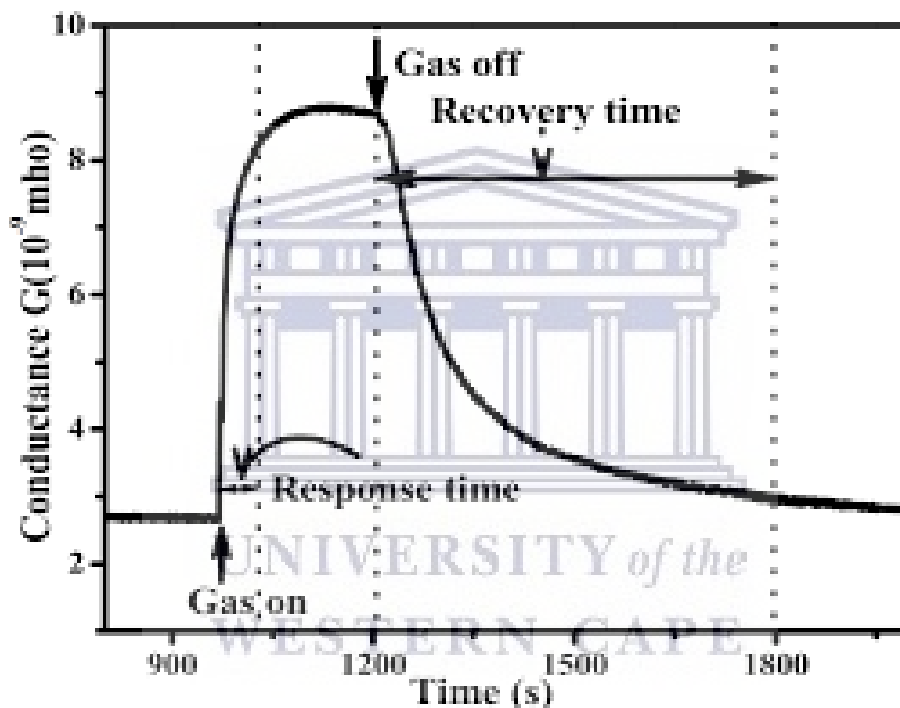


Figure 2.6: Schematic response-recovery curve of a chemiresistive gas sensor.

2.5.4 Stability

Stability refers to be the ability of a gas sensor to generate reproducible results over a certain period. This includes retaining/maintaining the sensitivity, selectivity, and response and recovery time. Stability, in particular, is a very important criterion for gas sensors as they are continuously heated, undergo response and recovery by detecting a certain concentration of

gas in the surrounding atmosphere, and occasionally operate in hostile environments. High stability in terms of parameters such as sensitivity, selectivity, and response and recovery time is highly crucial for the long-term operation of the sensor [83].

2.5.5 Other parameters

There are several other important parameters which can be used to characterize the performance of a gas sensor:

- The detection limit is defined as the lowest possible concentration of the target gas which can be detected by the gas sensor. In industrial/environmental monitoring applications, a detection limit in ppb level is usually desirable.
- Working temperature usually corresponds to the optimum temperature at which the sensor can achieve the maximum sensitivity toward the target gas.
- The life cycle refers to the duration of time over which the sensor will continuously operate.

Metal oxide gas sensors are versatile gas detection devices due to their compact size, low cost and easy production, and simple measuring electronics [84][85]. Despite that, there are drawbacks as the performance is affected by the structure and morphology of the sensing material, which imposes a hurdle with sensors that utilizes bulk or dense sensing materials that reduce the sensing properties (sensitivity, selectivity and response time) [86]. Nanoscience and nanotechnology have developed gas sensing technology as we can control the structure and morphology of nanostructures resulting in improved sensing properties [87].

2.6 MECHANISM FOR GAS SENSING

The sensing process of MOs semiconductors consists of two main functions receptor and transducer function. Figure 2.7 illustrates the mechanism leading to the MOs sensor response to oxidizing and reducing gases [88]. A space-charge layer forms and oxygen anions cover the surface of the MOs when the device is exposed to air under high temperature. When the sensor is exposed to carbon monoxide gas, the gas molecules react with the pre-adsorbed oxygen species. The electrons that were initially trapped by oxygen anions are released back onto the surface increasing the conductivity of the sensor.



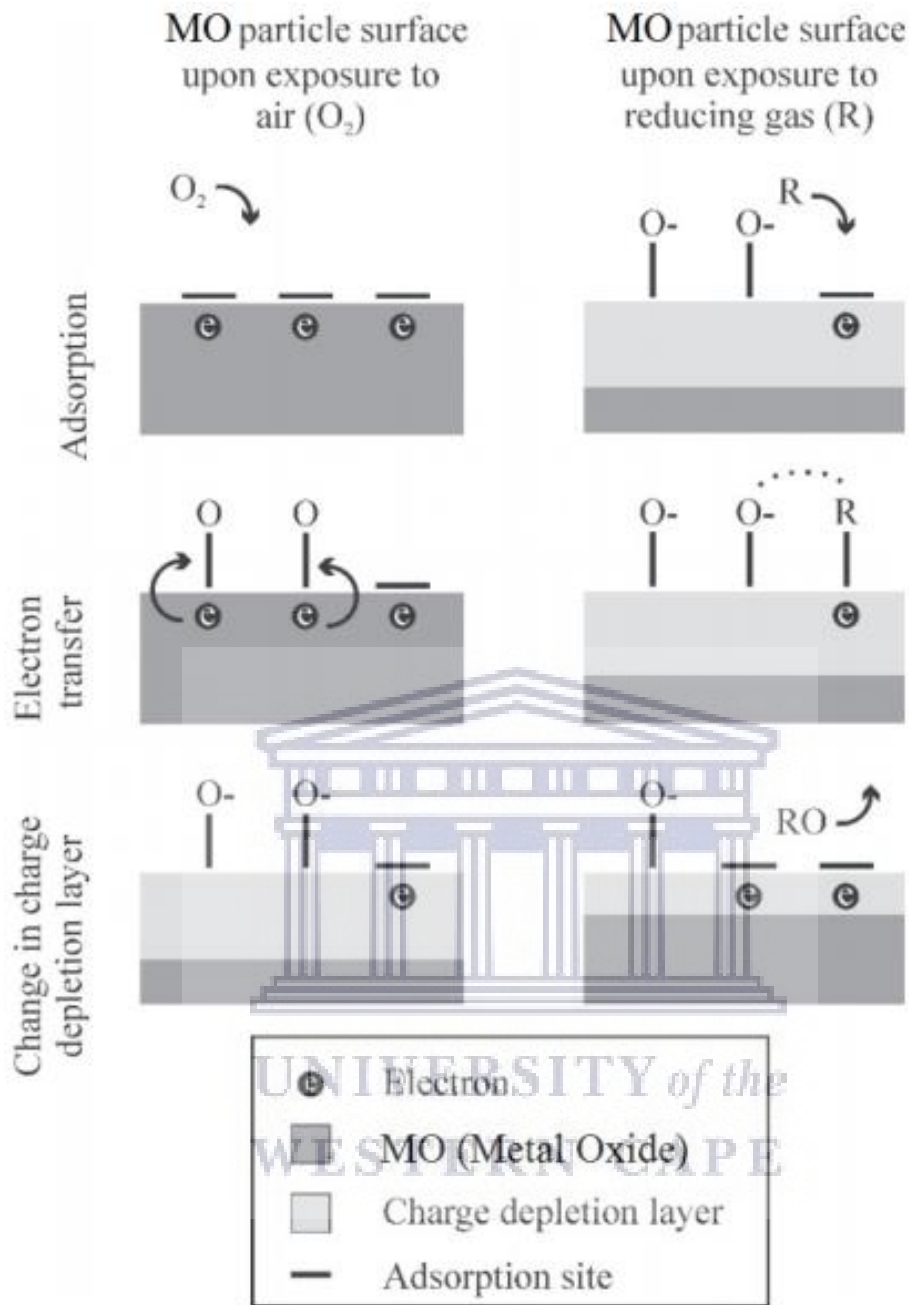


Figure 2.7: Illustrates the MOs sensor response to reducing and oxidizing gases [89].

2.7 REFERENCES

- [1] Han, C.H., Hong, D.W., Han, S.D., Gwak, J. and Singh, K.C., 2007. Catalytic combustion type hydrogen gas sensor using TiO₂ and UV-LED. *Sensors and Actuators B: Chemical*, 125(1), pp.224-228.
- [2] Yamazoe, N., Sakai, G. and Shimanoe, K., 2003. Oxide semiconductor gas sensors. *Catalysis Surveys from Asia*, 7(1), pp.63-75.
- [3] Sakamoto, J., Sato, R., Nakayama, J., Kasai, N., Shibutani, T. and Miyake, A., 2016. Leakage-type-based analysis of accidents involving hydrogen fueling stations in Japan and USA. *International journal of hydrogen energy*, 41(46), pp.21564-21570.
- [4] Seiyama, T., Kato, A., Fujiishi, K. and Nagatani, M., 1962. A new detector for gaseous components using semiconductive thin films. *Analytical Chemistry*, 34(11), pp.1502-1503.
- [5] Seiyama, T. and Kagawa, S., 1966. Study on a Detector for Gaseous Components Using Semiconductive Thin Films. *Analytical chemistry*, 38(8), pp.1069-1073.
- [6] Anthony S., 2018. United States Patent : 5861366. *New York*, 1, pp.1–29
- [7] Miura, N. and Yamazoe, N., 1992. Development of new chemical sensors based on low-temperature proton conductors. *Solid State Ionics*, 53, pp.975-982.
- [8] Lu, L., Li, R., Fan, K. and Peng, T., 2010. Effects of annealing conditions on the photoelectrochemical properties of dye-sensitized solar cells made with ZnO nanoparticles. *Solar Energy*, 84(5), pp.844-853.

- [9] Yamazoe, N., 1991. New approaches for improving semiconductor gas sensors. *Sensors and Actuators B: Chemical*, 5(1-4), pp.7-19.
- [10] Ono, K., Oishi, T. and Moriyama, J., 1981. Measurements on galvanic cells involving solid-sulphide electrolytes. *Solid State Ionics*, 3, pp.555-558.
- [11] Zha, S.W., Xia, C.R. and Meng, G.Y., 2001. Calculation of the emf of solid oxide fuel cells. *Journal of applied electrochemistry*, 31(1), pp.93-98.
- [12] Nitta, T., Terada, Z. and Hayakawa, S., 1980. Humidity-Sensitive Electrical Conduction of MgCr₂O₄-TiO₂ Porous Ceramics. *Journal of the American Ceramic Society*, 63(5-6), pp.295-300.
- [13] Wang, Z.L. and Kang, Z.C., 2012. *Functional and smart materials: structural evolution and structure analysis*. Springer Science & Business Media.
- [14] Berna, A., 2010. Metal oxide sensors for electronic noses and their application to food analysis. *Sensors*, 10(4), pp.3882-3910.
- [15] Fergus, J.W., 1997. The application of solid fluoride electrolytes in chemical sensors. *Sensors and Actuators B: Chemical*, 42(2), pp.119-130.
- [16] Jones, E., 1987. The pellistor catalytic gas detector. *Techniques and mechanism in gas sensing*, pp.17-31.
- [17] Gall, M., 1993. The Si-planar-pellistor array, a detection unit for combustible gases. *Sensors and Actuators B: Chemical*, 16(1-3), pp.260-264.
- [18] Gall, M., 1991. The Si planar pellistor: a low-power pellistor sensor in Si thin-film

- technology. *Sensors and Actuators B: Chemical*, 4(3-4), pp.533-538.
- [19] Bartlett, P.N., Guerin, S., Marwan, J., Gardner, J.W., Lee, S.M., Willettc, M.J. and Leclerc, S.A.A., 2002, May. A micromachined planar pellistor using an electrochemically deposited nanostructured catalyst. In *Proceedings for the Symposium on Microfabricated Systems and MEMS VI. Springmeeting of the Electrochemicals society, Philadelphia, USA* (pp. 24-31).
- [20] Korotcenkov, G., 2007. Practical aspects in design of one-electrode semiconductor gas sensors: Status report. *Sensors and Actuators B: Chemical*, 121(2), pp.664-678.
- [21] Guth, U., Vonau, W. and Zosel, J., 2009. Recent developments in electrochemical sensor application and technology—a review. *Measurement Science and Technology*, 20(4), p.042002.
- [22] Korotcenkov, G., Han, S.D. and Stetter, J.R., 2009. Review of electrochemical hydrogen sensors. *Chemical reviews*, 109(3), pp.1402-1433.
- [23] Azad, A.M., Akbar, S.A., Mhaisalkar, S.G., Birkefeld, L.D. and Goto, K.S., 1992. Solid-state gas sensors: A review. *Journal of the Electrochemical Society*, 139(12), p.3690.
- [24] Velasco, G., Schnell, J.P. and Croset, M., 1981. Thin solid state electrochemical gas sensors. *Sensors and Actuators*, 2, pp.371-384.
- [25] Wang, L., Ma, W., Zhang, P., Zhu, L., Yang, D., Wang, X. and Dai, S., 2019. Mid-Infrared Gas Detection Using a Chalcogenide Suspended-Core Fiber. *Journal of Lightwave Technology*, 37(20), pp.5193-5198.
- [26] Mohebati, A. and King, T.A., 1988. Remote detection of gases by diode laser spectroscopy. *Journal of modern optics*, 35(3), pp.319-324

- [27] Lübbers, D.W., 1995. Optical sensors for clinical monitoring. *Acta Anaesthesiologica Scandinavica*, 39, pp.37-54.
- [28] Hyseni, G., Caka, N. and Hyseni, K., 2010. Infrared thermal detectors parameters: semiconductor bolometers versus pyroelectrics. *WSEAS Transactions on circuits and systems*, 9(4), pp.238-247.
- [29] Kerstel, E. and Gianfrani, L., 2008. Advances in laser-based isotope ratio measurements: selected applications. *Applied Physics B*, 92(3), pp.439-449.
- [30] Wohltjen, H., Barger, W.R., Snow, A.W. and Jarvis, N.L., 1985. A vapor-sensitive chemiresistor fabricated with planar microelectrodes and a Langmuir-Blodgett organic semiconductor film. *IEEE transactions on electron devices*, 32(7), pp.1170-1174.
- [31] Kaur, G., Adhikari, R., Cass, P., Bown, M. and Gunatillake, P., 2015. Electrically conductive polymers and composites for biomedical applications. *Rsc Advances*, 5(47), pp.37553-37567.
- [32] Sun, Y.F., Liu, S.B., Meng, F.L., Liu, J.Y., Jin, Z., Kong, L.T. and Liu, J.H., 2012. Metal oxide nanostructures and their gas sensing properties: a review. *Sensors*, 12(3), pp.2610-2631.
- [33] Vander Wal, R.L., Hunter, G.W., Xu, J.C., Kulis, M.J., Berger, G.M. and Ticich, T.M., 2009. Metal-oxide nanostructure and gas-sensing performance. *Sensors and Actuators B: Chemical*, 138(1), pp.113-119.
- [34] Brattain, W.H. and Bardeen, J., 1953. Surface properties of germanium. *The Bell System Technical Journal*, 32(1), pp.1-41.

- [35] Bochenkov, V.E. and Sergeev, G.B., 2010. Sensitivity, selectivity, and stability of gas-sensitive metal-oxide nanostructures. *Metal oxide nanostructures and their applications*, 3, pp.31-52.
- [36] Eranna, G., Joshi, B.C., Runthala, D.P. and Gupta, R.P., 2004. Oxide materials for development of integrated gas sensors—a comprehensive review. *Critical Reviews in Solid State and Materials Sciences*, 29(3-4), pp.111-188.
- [37] McGinley, C., Al Moussalami, S., Riedler, M., Pflughoeft, M., Borchert, H., Haase, M., De Castro, A.R.B., Weller, H. and Möller, T., 2001. Pure and Sb-doped SnO₂ nanoparticles studied by photoelectron spectroscopy. *The European Physical Journal D-Atomic, Molecular, Optical and Plasma Physics*, 16(1), pp.225-228.
- [38] Habte, A.G., Hone, F.G. and Dejene, F.B., 2020. Influence of annealing temperature on the structural, morphological and optical properties of SnO₂ nanoparticles. *Physica B: Condensed Matter*, 580, p.411760.
- [39] Nütz, T. and Haase, M., 2000. Wet-chemical synthesis of doped nanoparticles: optical properties of oxygen-deficient and antimony-doped colloidal SnO₂. *The Journal of Physical Chemistry B*, 104(35), pp.8430-8437.
- [40] Sun, P., Zhao, W., Cao, Y., Guan, Y., Sun, Y. and Lu, G., 2011. Porous SnO₂ hierarchical nanosheets: hydrothermal preparation, growth mechanism, and gas sensing properties. *CrystEngComm*, 13(11), pp.3718-3724.
- [41] Xi, G. and Ye, J., 2010. Ultrathin SnO₂ nanorods: template-and surfactant-free solution phase synthesis, growth mechanism, optical, gas-sensing, and surface adsorption properties. *Inorganic chemistry*, 49(5), pp.2302-2309.
- [42] Chen, D., Xu, J., Xie, Z. and Shen, G., 2011. Nanowires assembled SnO₂ nanopolyhedrons

- with enhanced gas sensing properties. *ACS Applied Materials & Interfaces*, 3(6), pp.2112-2117.
- [43] Huang, J., Matsunaga, N., Shimano, K., Yamazoe, N. and Kunitake, T., 2005. Nanotubular SnO₂ templated by cellulose fibers: synthesis and gas sensing. *Chemistry of Materials*, 17(13), pp.3513-3518.
- [44] Sun, P., Cao, Y., Liu, J., Sun, Y., Ma, J. and Lu, G., 2011. Dispersive SnO₂ nanosheets: hydrothermal synthesis and gas-sensing properties. *Sensors and Actuators B: Chemical*, 156(2), pp.779-783.
- [45] Liangyuan, C., Shouli, B., Guojun, Z., Dianqing, L., Aifan, C. and Liu, C.C., 2008. Synthesis of ZnO–SnO₂ nanocomposites by microemulsion and sensing properties for NO₂. *Sensors and Actuators B: Chemical*, 134(2), pp.360-366.
- [46] Wahab, R., Kim, Y.S. and Shin, H.S., 2009. Synthesis, characterization and effect of pH variation on zinc oxide nanostructures. *Materials transactions*, 50(8), pp.2092-2097.
- [47] Natsume, Y. and Sakata, H., 2000. Zinc oxide films prepared by sol-gel spin-coating. *Thin solid films*, 372(1-2), pp.30-36.
- [48] Wang, Z.L., 2004. Zinc oxide nanostructures: growth, properties and applications. *Journal of physics: condensed matter*, 16(25), p.R829.
- [49] Khorami, H.A., Keyanpour-Rad, M. and Vaezi, M.R., 2011. Synthesis of SnO₂/ZnO composite nanofibers by electrospinning method and study of its ethanol sensing properties. *Applied surface science*, 257(18), pp.7988-7992.
- [50] Kumar, R., Al-Dossary, O., Kumar, G. and Umar, A., 2015. Zinc oxide nanostructures for NO₂ gas–sensor applications: A review. *Nano-Micro Letters*, 7(2), pp.97-120.

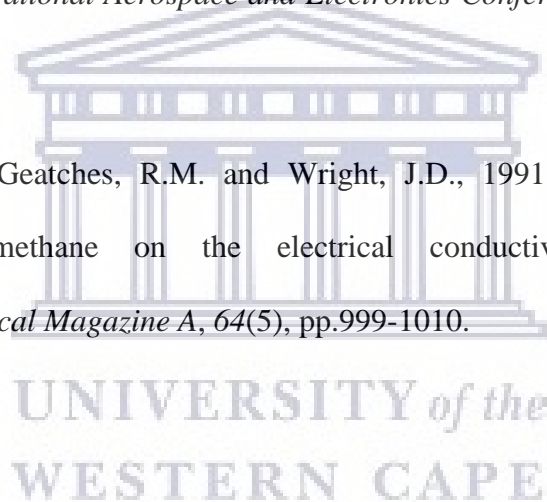
- [51] Geng, B., Fang, C., Zhan, F. and Yu, N., 2008. Synthesis of polyhedral ZnSnO₃ microcrystals with controlled exposed facets and their selective gas-sensing properties. *small*, 4(9), pp.1337-1343.
- [52] Al-Kuhaili, M.F., Durrani, S.M.A. and Bakhtiari, I.A., 2008. Carbon monoxide gas-sensing properties of CeO₂-ZnO thin films. *Applied Surface Science*, 255(5), pp.3033-3039.
- [53] Hirano, M. and Kato, E., 1996. Hydrothermal synthesis of cerium (IV) oxide. *Journal of the American Ceramic Society*, 79(3), pp.777-780.
- [54] Orel, Z.C. and Orel, B., 1994. Optical properties of pure CeO₂ and mixed CeO₂/SnO₂ thin film coatings. *physica status solidi (b)*, 186(1), pp.K33-K36.
- [55] Ivanova, A.S., 2009. Physicochemical and catalytic properties of systems based on CeO₂. *Kinetics and Catalysis*, 50(6), pp.797-815.
- [56] Walton, R.I., 2011. Solvothermal synthesis of cerium oxides. *Progress in Crystal Growth and Characterization of Materials*, 57(4), pp.93-108.
- [57] Yuan, Q., Duan, H.H., Li, L.L., Sun, L.D., Zhang, Y.W. and Yan, C.H., 2009. Controlled synthesis and assembly of ceria-based nanomaterials. *Journal of colloid and interface science*, 335(2), pp.151-167.
- [58] Korotcenkov, G., 2007. Practical aspects in design of one-electrode semiconductor gas sensors: Status report. *Sensors and Actuators B: Chemical*, 121(2), pp.664-678.
- [59] Gangopadhyay, S., Frolov, D.D., Masunov, A.E. and Seal, S., 2014. Structure and properties of cerium oxides in bulk and nanoparticulate forms. *Journal of Alloys and compounds*, 584, pp.199-208.
- [60] Manorama, S.V., Izu, N., Shin, W., Matsubara, I. and Murayama, N., 2003. On the platinum

- sensitization of nanosized cerium dioxide oxygen sensors. *Sensors and Actuators B: Chemical*, 89(3), pp.299-304.
- [61] Liao, L., Mai, H.X., Yuan, Q., Lu, H.B., Li, J.C., Liu, C., Yan, C.H., Shen, Z.X. and Yu, T., 2008. Single CeO₂ nanowire gas sensor supported with Pt nanocrystals: gas sensitivity, surface bond states, and chemical mechanism. *The Journal of Physical Chemistry C*, 112(24), pp.9061-9065.
- [62] Mei, Z., Xidong, W., Fuming, W. and Wenchao, L., 2003. Oxygen sensitivity of nano-CeO₂ coating TiO₂ materials. *Sensors and Actuators B: Chemical*, 92(1-2), pp.167-170.
- [63] Khare, N., Singh, D.P., Gupta, A.K., Sen, S., Aswal, D.K., Gupta, S.K. and Gupta, L.C., 2005. Direct evidence of weak-link grain boundaries in a polycrystalline MgB₂ superconductor.
- [64] Barnes, M.A., 2012. *Integrating High Temperature Superconducting Yttrium Barium Copper Oxide with Silicon-on-Sapphire Electronics* (Doctoral dissertation, University of Cincinnati).
- [65] Kaur, M., Gupta, S.K., Betty, C.A., Saxena, V., Katti, V.R., Gadkari, S.C. and Yakhmi, J.V., 2005. Detection of reducing gases by SnO₂ thin films: an impedance spectroscopy study. *Sensors and Actuators B: Chemical*, 107(1), pp.360-365.
- [66] Rothschild, A. and Komem, Y., 2004. The effect of grain size on the sensitivity of nanocrystalline metal-oxide gas sensors. *Journal of Applied Physics*, 95(11), pp.6374-6380.
- [67] Xu, C., Tamaki, J., Miura, N. and Yamazoe, N., 1991. Grain size effects on gas sensitivity of porous SnO₂-based elements. *Sensors and Actuators B: Chemical*, 3(2), pp.147-155.
- [68] Ogawa, H., Nishikawa, M. and Abe, A., 1982. Hall measurement studies and an electrical conduction model of tin oxide ultrafine particle films. *Journal of Applied Physics*, 53(6), pp.4448-4455.

- [69] Van Duy, N., Van Hieu, N., Huy, P.T., Chien, N.D., Thamilselvan, M. and Yi, J., 2008. Mixed SnO₂/TiO₂ included with carbon nanotubes for gas-sensing application. *Physica E: Low-dimensional Systems and Nanostructures*, 41(2), pp.258-263.
- [70] Sharma, S. and Madou, M., 2012. A new approach to gas sensing with nanotechnology. *Philosophical Transactions of the Royal Society A: Mathematical, Physical and Engineering Sciences*, 370(1967), pp.2448-2473.
- [71] Eranna, G., Joshi, B.C., Runthala, D.P. and Gupta, R.P., 2004. Oxide materials for development of integrated gas sensors—a comprehensive review. *Critical Reviews in Solid State and Materials Sciences*, 29(3-4), pp.111-188.
- [72] Yu, J.H. and Choi, G.M., 1998. Electrical and CO gas sensing properties of ZnO–SnO₂ composites. *Sensors and Actuators B: Chemical*, 52(3), pp.251-256.
- [73] Korotcenkov, G., 2008. The role of morphology and crystallographic structure of metal oxides in response of conductometric-type gas sensors. *Materials Science and Engineering: R: Reports*, 61(1-6), pp.1-39.
- [74] Gong, J., Chen, Q., Lian, M.R., Liu, N.C., Stevenson, R.G. and Adami, F., 2006. Micromachined nanocrystalline silver doped SnO₂ H₂S sensor. *Sensors and Actuators B: Chemical*, 114(1), pp.32-39.
- [75] Fishchuk, I.I., Kadashchuk, A.K., Genoe, J., Ullah, M., Sitter, H., Singh, T.B., Sariciftci, N.S. and Bässler, H., 2010. Temperature dependence of the charge carrier mobility in disordered organic semiconductors at large carrier concentrations. *Physical Review B*, 81(4), p.045202.
- [76] Tanvir, N.B., Yurchenko, O., Laubender, E. and Urban, G., 2017. Investigation of low temperature effects on work function based CO₂ gas sensing of nanoparticulate CuO films. *Sensors and Actuators B: Chemical*, 247, pp.968-974.

- [77] Fine, G.F., Cavanagh, L.M., Afonja, A. and Binions, R., 2010. Metal oxide semi-conductor gas sensors in environmental monitoring. *sensors*, 10(6), pp.5469-5502.
- [78] Sun, Y.F., Liu, S.B., Meng, F.L., Liu, J.Y., Jin, Z., Kong, L.T. and Liu, J.H., 2012. Metal oxide nanostructures and their gas sensing properties: a review. *Sensors*, 12(3), pp.2610-2631.
- [79] Wang, C., Yin, L., Zhang, L., Xiang, D. and Gao, R., 2010. Metal oxide gas sensors: sensitivity and influencing factors. *sensors*, 10(3), pp.2088-2106.
- [80] Ouyang, W., Teng, F., He, J.H. and Fang, X., 2019. Enhancing the photoelectric performance of photodetectors based on metal oxide semiconductors by charge-carrier engineering. *Advanced Functional Materials*, 29(9), p.1807672.
- [81] Yamazoe, N., Sakai, G. and Shimano, K., 2003. Oxide semiconductor gas sensors. *Catalysis Surveys from Asia*, 7(1), pp.63-75.
- [82] Kumar, N., Srivastava, A.K., Nath, R., Gupta, B.K. and Varma, G.D., 2014. Probing the highly efficient room temperature ammonia gas sensing properties of a luminescent ZnO nanowire array prepared via an AAO-assisted template route. *Dalton Transactions*, 43(15), pp.5713-5720.
- [83] Korotcenkov, G. and Cho, B.K., 2011. Instability of metal oxide-based conductometric gas sensors and approaches to stability improvement (short survey). *Sensors and Actuators B: Chemical*, 156(2), pp.527-538. *Elsevier*
- [84] Tomchenko, A.A., Harmer, G.P., Marquis, B.T. and Allen, J.W., 2003. Semiconducting metal oxide sensor array for the selective detection of combustion gases. *Sensors and Actuators B: Chemical*, 93(1-3), pp.126-134.
- [85] Kanan, S.M., El-Kadri, O.M., Abu-Yousef, I.A. and Kanan, M.C., 2009. Semiconducting metal

- oxide based sensors for selective gas pollutant detection. *Sensors*, 9(10), pp.8158-8196.
- [86] Wang, C., Yin, L., Zhang, L., Xiang, D. and Gao, R., 2010. Metal oxide gas sensors: sensitivity and influencing factors. *sensors*, 10(3), pp.2088-2106.
- [87] Tricoli, A., Righettoni, M. and Teleki, A., 2010. Semiconductor gas sensors: dry synthesis and application. *Angewandte Chemie International Edition*, 49(42), pp.7632-7659.
- [88] Bright, V.M., Kolesar, E.S. and Hauschild, N.T., 1994, May. Investigation of the sensitivity, selectivity, and reversibility of the chemically-sensitive field-effect transistor (CHEMFET) to detect NO_2 , $\text{C}_3\text{H}_9\text{PO}_3$, and BF_3 . In *Proceedings of National Aerospace and Electronics Conference (NAECON'94)* (pp. 342-349).
- [89] Chadwick, A.V., Geatches, R.M. and Wright, J.D., 1991. The effect of carbon monoxide and methane on the electrical conductivity of TiO_2 single crystals. *Philosophical Magazine A*, 64(5), pp.999-1010.



CHAPTER 3

SAMPLE PREPARATION AND ANALYTICAL TECHNIQUES

3.1 HYDROTHERMAL TECHNIQUE

In this study, a one-pot hydrothermal technique was used to synthesize pure CeO₂ nanoparticles. In this chapter, the hydrothermal technique is discussed first. Secondly, the chemical reagents and synthesis procedures that were employed in the study are discussed. Lastly, characterization techniques that were utilized in the study are presented.

The hydrothermal technique is a high-temperature synthesis method in which aqueous reactants are allowed to react under “low” temperature and “high” pressure in a Teflon lined autoclave (Parr Instruments). It is one of the most effective ways of synthesizing morphologically controlled nanoparticles of high purity, high dispersion, and narrow size distribution [1]. As documented in the literature, crystal nucleation and growth in hydrothermal reactions are primarily a function of the reaction temperature and pressure [2][3]. although other factors such as the choice of solvent or concentration of the precursor reactants also play a big role [4]. The main advantage of this method is the ability to control particle size and shape of the nanoparticles by applying different reaction parameters [5]. The main disadvantage of using this method, however, is the fact that acquisition of the required equipment such as autoclaves and a high-temperature temperature-programmed box furnace is expensive in addition to the fact that reactions cannot be performed as quickly compared to other synthesis techniques such as chemical precipitation or thermal decomposition of metal precursor salts in high vacuum systems [6]. Figure 3.1 below shows the equipment needed to perform hydrothermal reactions.



Figure 3.1: Teflon cup and Stainless Steel Autoclave vessel

3.2 CHARACTERIZATION TECHNIQUES

The study of nanostructured materials and surface analysis requires accurate, sensitive, and well-understood experimental techniques. To study the surface morphology, Scanning Electron Microscopy was utilized, to probe the structural properties and internal structure, Powder X-ray Diffraction, and Transmission Electron Microscopy were considered. For chemical state and point defects analyses, such as oxygen vacancies, X-ray photoelectron spectroscopy (XPS), Photoluminescence and Raman Spectroscopy analyses were conducted. While the effect of surface area and pore diameter on the gas sensing performance were

probed using the Brunauer-Emmett-Teller-Surface Area analysis. Below is a detailed description of these techniques.

3.2.1 Scanning Electron Microscopy

3.2.1.1 Introduction

The scanning electron microscope (SEM) is a characterization technique used in diverse fields of science even having industry applications. The three-dimensional images formed during SEM gives accurate information of the surface morphology and topography of the sample up to the nanometer scale.

In an SEM, electrons are thermionically emitted from a cathode or a field emission gun (FEG), situated at the top of its electron-optical column. These emitted electrons form an electron cloud. A beam of electrons is formed by accelerating the electrons between the cathode (by the electron gun) and anode (by the specimen). This is done by applying high voltages towards anode from the cathode. As the beam of electrons is accelerated down the SEM column, which is then focused by electromagnetic lenses, coils, and apertures into a fine probe that systematically scans over the specimen surface, to produce an image [7].

From the SEM schematic shown in figure 3.2, the two condenser lenses, situated below the electron gun are used to focus the emerging beam into a smaller diameter size, which is then further aligned and focused by apertures and coils within the column until it reaches the objective lens. The objective lens then further demagnetizes the beam into a small spot of about 0.1-1 μm in diameter and moves it up and down in space until it reaches the specimen surface [7]. Aside from its focusing capabilities, the objective lens also determines the intensity of the incident beam on the specimen and thus controls the image brightness.

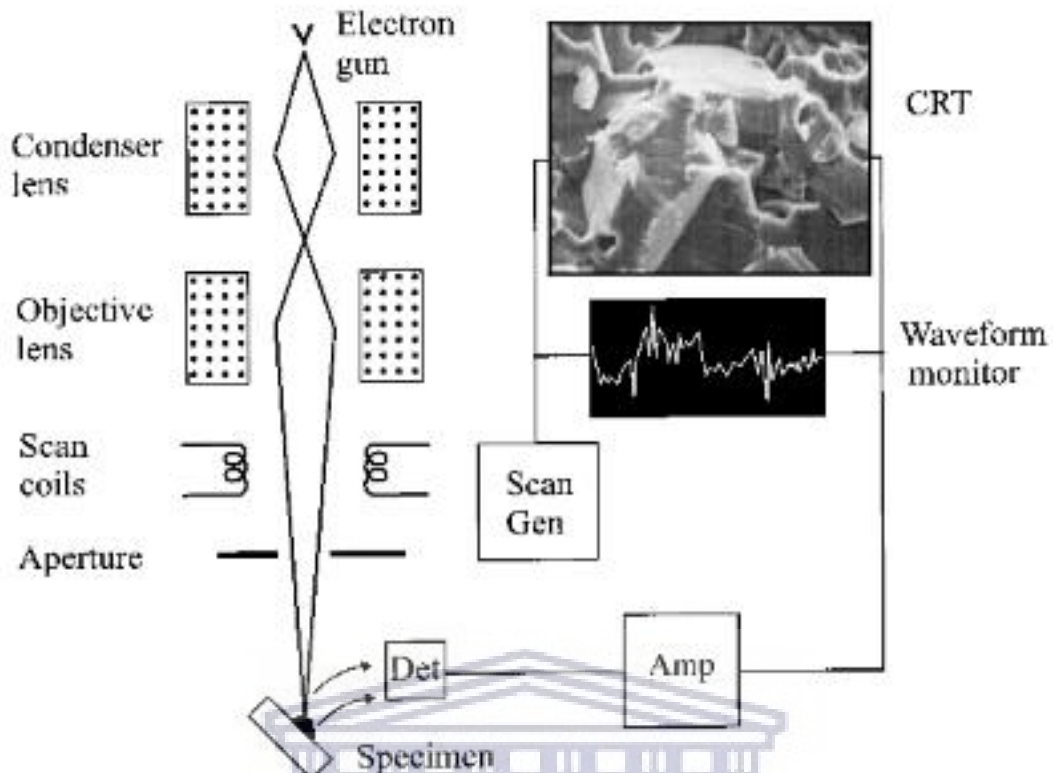


Figure 3.2: Schematic diagram showing the main components comprising an SEM [7].

3.2.1.2 Electron beam – specimen interaction signals

When an incident primary beam of electrons interacts with a specimen sample, several signals are generated within the sample and get detected within the SEM. These generated signals contain valuable information about the morphology and composition of the sample. The schematic diagram shown in figure 3.3 presents the types of signals generated during electron beam interaction with the sample. Signals such as the secondary, backscattered and transmitted electrons provide information about the surface morphology of the sample while characteristic x-rays, cathodoluminescence and Auger electron signals contain information about the chemical composition of the sample[8].

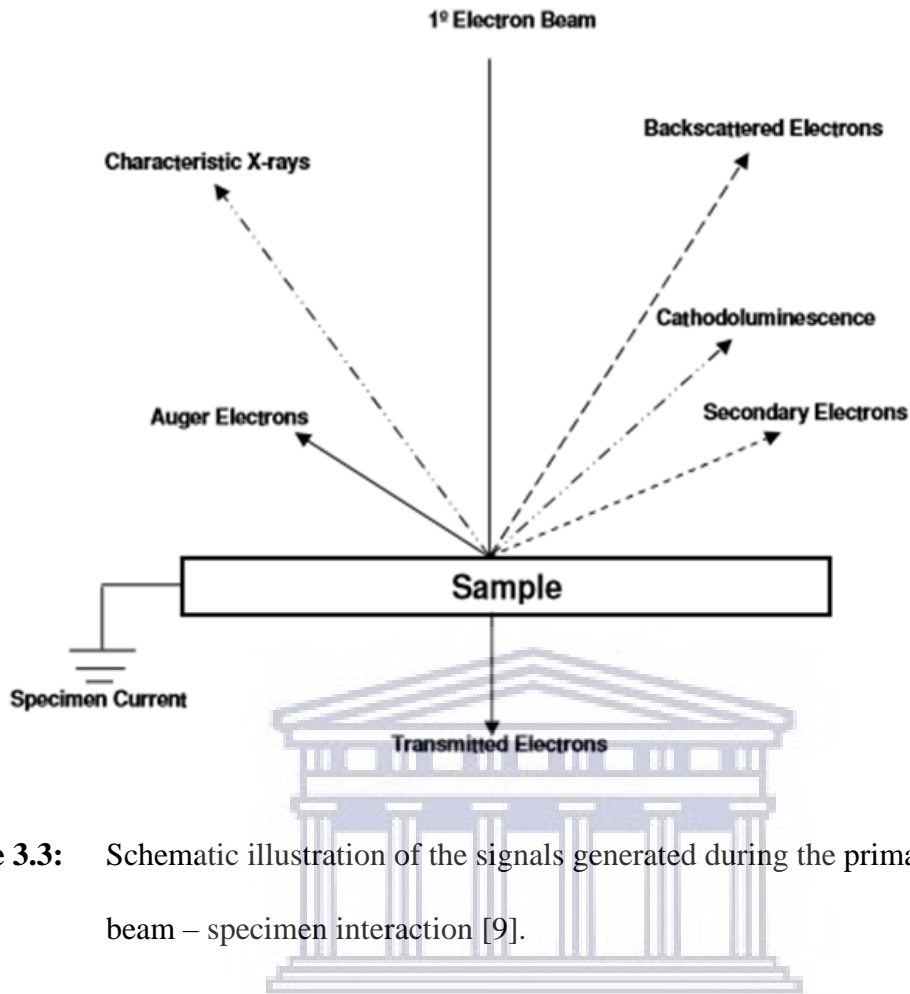


Figure 3.3: Schematic illustration of the signals generated during the primary electron beam – specimen interaction [9].

3.2.1.3 Characteristic x-ray and energy dispersive spectroscopy

From the schematic illustration of an atom shown in figure 3.4, it can be observed that the nucleus of an atom is surrounded by circular energy levels that can be referred to as ‘shells’. These shells are denoted by K, L, and M, which corresponds to the principal quantum number, $n = 1, 2, 3$. During electron beam and sample interaction, an inner electron from the K- shell may be knocked off leaving the atom in an excited state. For the atom to return to its normal ground state, the vacancy created in the K shell needs to be filled by an electron from the outer shells (L or M). When this recombination occurs, the outer electron undergoes a

discrete energy transition and the energy difference between the two energy states is discrete and characteristic of that particular atom. This surplus energy is then emitted as x-rays [10].

When the vacancy created in the K shell is filled by an electron from the neighbouring L shell, the emitted x-ray is referred to as the $K\alpha$ x-ray, while if the vacancy is filled by an M shell electron, $K\beta$ x-rays are emitted. A similar nomenclature is adopted when an L shell electron is knocked off and the vacancy is filled by an M shell electron. The α and β subscripts represent the first and second nearest neighbour shell respectively [11].

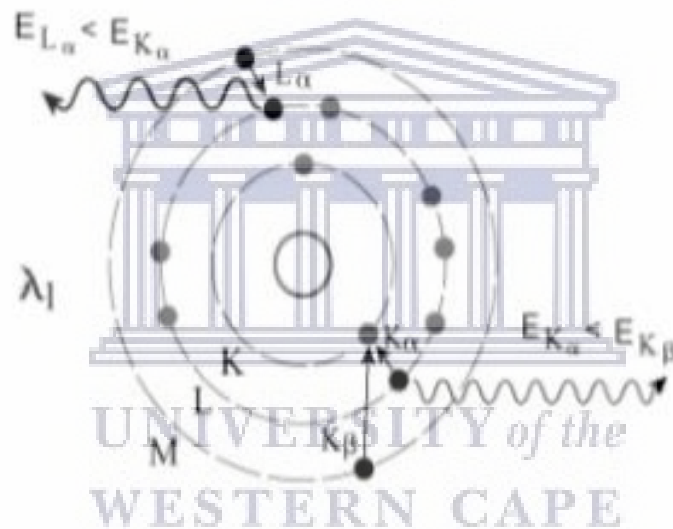


Figure 3.4: Characteristic x-ray emission by an atom [12].

Energy Dispersive X-ray Spectroscopy (EDS) is a qualitative and quantitative X-ray micro-analytical technique that employs energy dispersion, which is the separation of x-rays according to their energy. The separation is performed by a semiconductor detector. When an x-ray strikes a semiconductor crystal, electrons in the crystal absorb a given amount of energy and are excited. The absorbed energy is then converted to an electronic signal, which

is emitted and amplified. The amplified electrical pulses from the semiconductor are converted to digital form and fed into a multi-channel analyzer (MCA). The MCA sorts these signals and, in effect, counts the number of x-rays at each energy level that strikes the crystal. This information is then plotted as a spectrum [13].

High resolution scanning electron microscope (HR-SEM) brings some advantages over low-voltage SEM. For example, the (field-emission gun) FEG-SEM is capable of producing high primary electron brightness and small spot size even at low accelerating potentials [14]. HR-SEM is equipped with charge compensation (CC) used for viewing uncoated, non-conducting specimens. Moreover, HR-SEM has plasma cleaning (PC) which is only used in-situ in the HR-SEM but can be applied to all specimen's ex-situ. The advantage of PC is that it can be used to clean special surfaces after contamination build-up. Contamination free surfaces are vital for HR-SEM work.

3.2.1.4 Sample preparation

There are general properties that materials should have to be analyzed by a Scanning Electron Microscope (SEM) such as; conductivity, vacuum compliant, beam sensitivity, and sample size. Sample preparation is important in SEM analysis because poorly prepared samples produce inaccurate scientific results. There are hard materials (metals, ceramics, and minerals) and soft materials (polymers, biological and wet). Different types of samples can be prepared depending on whether topographical imaging or microanalysis is required which are; Nanoparticles, powders, bulk material, wafers, and IC devices [15].

3.2.2 Transmission Electron Microscopy

Transmission electron microscopy is a high-end scientific imaging technique that uses a high energy beam of electrons to image objects on a very fine scale. The technique can be used to give information about the topography (surface features), morphology (shape and size), composition (both qualitative and quantitative), and crystallographic information [16]. In this study, a JEOL2100 instrument equipped with an EDAX detector and an annular dark-field detector was used to collect microscopy data at an acceleration voltage of 200 kV. In a typical sample preparation procedure, the freshly prepared CeO₂ precipitate was lightly agitated for 30 seconds (while still in the Teflon cup) using a stirring rod to uniformly disperse the nanoparticles within the reaction solvent (H₂O). Immediately afterward, a holey carbon or copper grid was dipped into the reaction mixture for two seconds before it was removed. Samples were then placed inside the TEM for analysis.

3.2.3 X-ray diffraction

3.2.3.1 Introduction

X-rays are a form of electromagnetic radiation, which has a wavelength ranging from 0.01 to 10 nanometers. Characteristic X-rays are produced when an element is bombarded with high-energy particles, which can be photons, electrons or ions (such as protons). When the incident particle strikes a bound electron (the target electron) in an atom, the target electron is ejected from the inner shell of the atom. Bremsstrahlung radiation is given off by the electrons as they are scattered by the strong electric field near the High-Z (proton number) nuclei. These X-rays have a continuous spectrum [17].

Diffraction is a phenomenon that occurs when waves interfere with a structure whose repeat distance is about the same as that of the incident wavelength. Upon interaction, constructive and destructive interference patterns result due to the scattering of the incoming wave fronts by the structure. The wavelength range of x-rays is about the same as that of the interatomic spacing found in three-dimensional crystalline structures, meaning that x-rays can be diffracted by these crystalline structures with each atom in the crystalline structure serving as a scattering center for the incoming wave fronts. This phenomenon is known as x-ray diffraction (XRD) and can be used as a tool for the investigation of the fine, crystalline structure of matter [17].

3.2.3.2 Theory

3.3.3.2.1 Crystal Structure and Bravais's Lattices

The atoms found in materials can be either randomly distributed, thus making the material amorphous or they can be arranged in a periodic pattern in three dimensions, resulting in the material being crystalline. When thinking about the atomic arrangement within a crystal, it is best to imagine the atoms as a set of imaginary points with a fixed relation in space. Figure 3.5 illustrates the above concept, referred to as a point lattice and is defined as an array of points in space, so arranged that each point has identical surroundings [18].

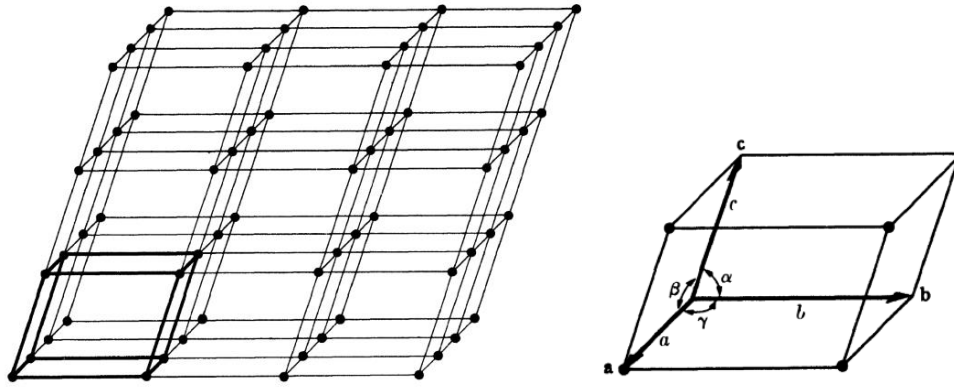


Figure 3.5: Schematic of a point lattice and primitive cell and the angles between the translation vectors [18].

By drawing three vectors and from the corner of any lattice point, one generates a point lattice unit cell. These vectors, known as the crystallographic axes of the unit cell can also be described in terms of their lengths (a , b and c) and the angle between them (α , β , and γ), known as the lattice constants or lattice parameters as shown in Figure 3.6. Not only do the crystallographic axes define the unit cell, but it also defines the whole point lattice, which can be produced by repeated action of the vectors [18]. Depending on the relationship between the lattice parameters (i.e. a , b , c , α , β , and γ) one can distinguish between fourteen different points or Bravais lattices, as described in Table 3.1. The direction of any vector within the Bravais lattice is given as a linear combination of the three crystallographic axes as:

$$\bar{x} = u\bar{a} + v\bar{b} + w\bar{c} \quad 3.1$$

where \bar{a} , \bar{b} and \bar{c} are any vector in the Bravais lattice and u , v and w are the coordinates of any point on the vector. In short, equation 3.1 can be written as $[u \ v \ w]$. However, $[u \ v \ w]$ are always converted to a set of smallest integer e.g. $[2 \ 2 \ 4]$ and $[3 \ 3 \ 6]$ represents the same

direction, with [1 1 2] the preferred notation. Collectively, all of these vectors form the reciprocal space of the lattice or reciprocal lattice.

Table 3.1: Description of the fourteen Bravais lattices [19].

	Axial length and angles	Bravais lattice
Cubic	Three equal axis at right angles $a = b = c, \alpha = \beta = \gamma = 90^\circ$	Simple, Body-centered and Face-centered
Tetragonal	Three angles at right angles, two equal $a = b \neq c, \alpha = \beta = \gamma = 90^\circ$	Simple and Body-centered
Orthorhombic	Three unequal axis at right angles $a \neq b \neq c, \alpha = \beta = \gamma = 90^\circ$	Simple, Body-centered, Face-centered and Base-centered
Rhombohedral	Three equal axes, equally inclined $a = b = c, \alpha = \beta = \gamma \neq 90^\circ$	Simple
Hexagonal	Two equal co-planar axes at 120° , third axis at right angles $a = b \neq c, \alpha = \beta = 90^\circ, \gamma = 120^\circ$	Simple
Monoclinic	Three unequal axes, one pair not at right angles	Simple and Body-centered

	$a \neq b \neq c, \alpha = \gamma = 90^\circ \neq \beta$	
Triclinic	Three unequal axes, unequally inclined and none at right angles $a \neq b \neq c, \alpha \neq \beta \neq \gamma \neq 90^\circ$	Simple

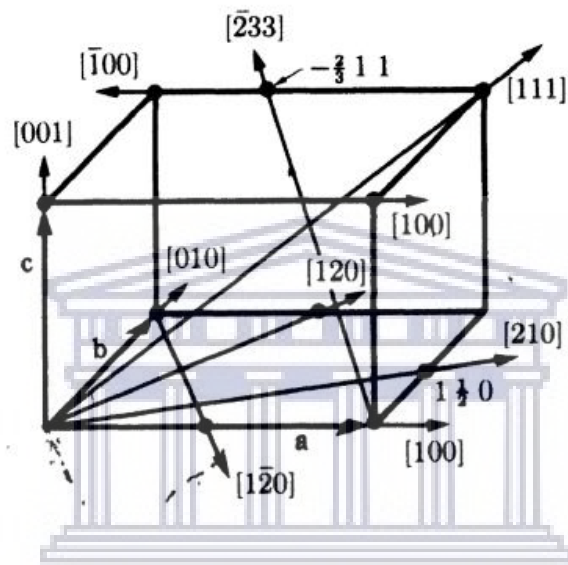


Figure 3.6: Indices for directions for a general unit cell [19].

A crystallographic lattice plane is a plane that contains a minimum of three non-collinear lattice points. The Miller indices are used to describe the orientation of a plane. The Miller indices can be defined as the reciprocals of the fractional intercepts which the plane makes with the crystallographic axes. A set of planes in a cubic system represented by Miller indices $(h k l)$ makes fractional intercepts of $\frac{a}{h}, \frac{b}{k}, \frac{c}{l}$ with the unit cell with axial lengths a, b and c .

There are, however, a set of parallel equidistant planes that have $(h k l)$ as Miller indices.

These planes are called planes of form and are denoted by $\{h\ k\ l\}$ [19]. The interplanar spacing between the set $\{h\ k\ l\}$ of planes in a cubic system is given by:

$$d = \frac{a}{\sqrt{h^2 + k^2 + l^2}} \quad 3.2$$

where a is the lattice parameter of the unit cell.

3.2.3.3 Bragg's law for diffraction

To understand the phenomenon of x-ray diffraction in crystals, known as Bragg's diffraction, consider a monochromatic beam of parallel x-rays, strikes a stack of planes $(h\ k\ l)$ spaced a distance d apart at an angle θ , Figure 3.7. Each plane consists of a series of equally spaced atoms, each of which is capable of scattering the incident radiation.

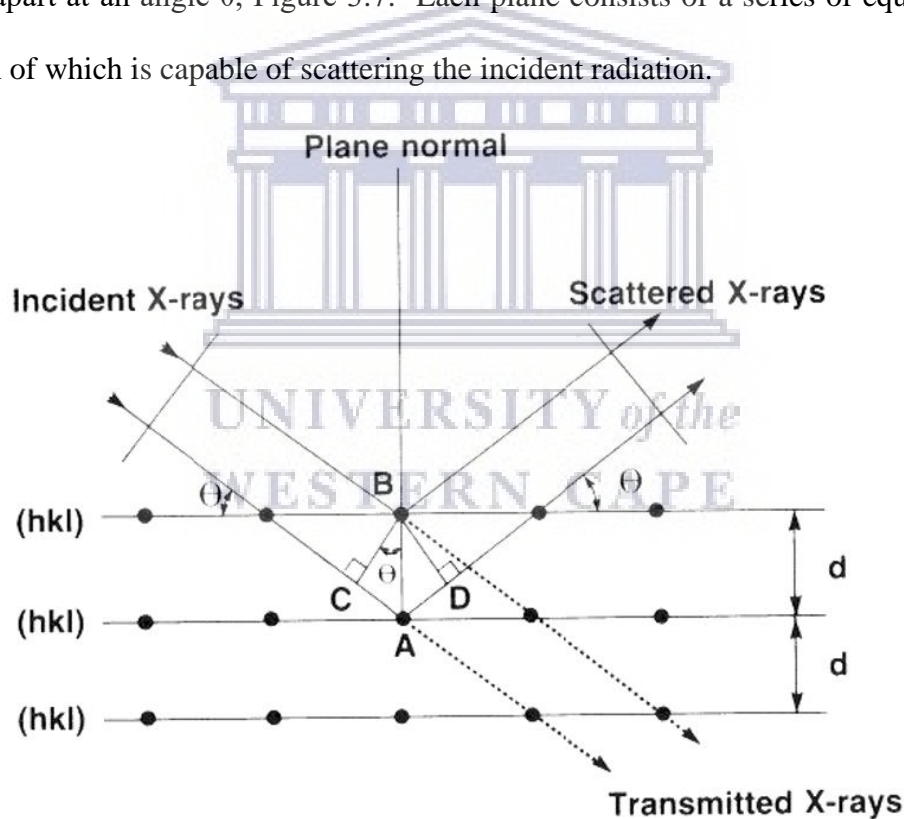


Figure 3.7: Interference of radiation between atomic planes in a crystal and Bragg's law [20].

The scattered rays, resulting from the interaction of the incident beam with the atoms of the parallel planes, will recombine to form a diffracted beam if and only if their path difference is an integer multiple of wavelengths.

$$AD + CD = \theta \sin d + \theta \sin d = n\lambda \quad 3.3$$

where n is the integer multiple (order of diffraction), λ is the wavelength of the radiation, d the interplanar spacing, θ the incident angle (Bragg angle). Equation 3.3 can be simplified to give,

$$2s \sin d = n\lambda \quad 3.4$$

which is known as Bragg's law. It also gives the angle θ at which a set of planes ($h k l$) of spacing d constructively reflects x-rays of wavelength λ in the n th order [20].

3.2.4 Raman spectroscopy

Raman spectroscopy is a distinct technique that is usually utilized to detect vibrational modes. According to Raman's influence, monochromatic light is in-elastically scattered by atoms in a medium [21]. Usually, it employs laser radiation in the visible frequency range to excite the sample. Once the incident light interrelates with the material, the molecules of the sample or material become excited to a higher energy level while absorbing the incident light photons and which later de-excited by the remission of re-emit the photon elastic or after in-elastic scattering. Once the scattered light is strong and has similar frequency like that of the incident light, elastic scattering occurs and is also referred to as Rayleigh scattering. In Raman scattering, the re-emitted light contains lower or higher frequency in comparison to that of the incident light that is considered as Stokes and anti-Stokes scattering [22].

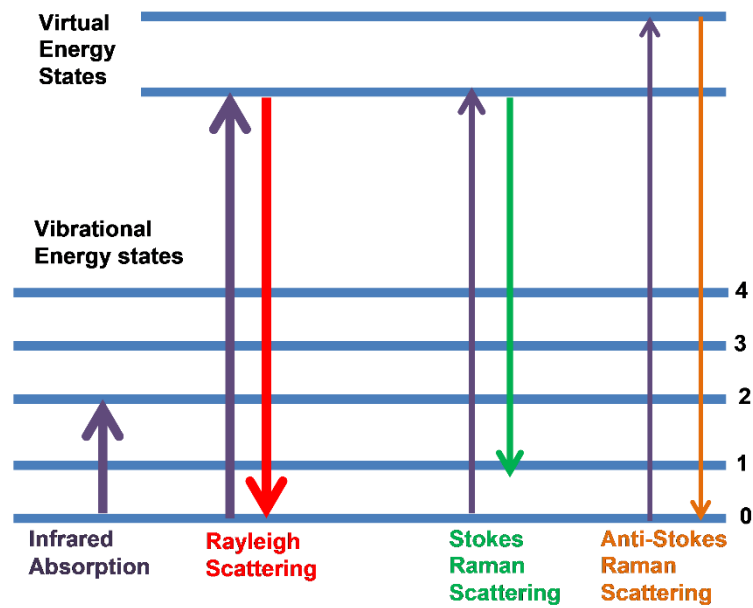


Figure 3.8: Schematic diagram showing the Rayleigh and Raman scattering.

Throughout the absorption of a photon by a Raman-active molecule, part of the photon's energy is transmitted to the Raman active modes, and the energy of the scattered photon decreases. This frequency is recognized as Stokes frequency. Furthermore, the Raman active mode that happens in the excited vibrational state absorbs a photon and emits a scattered photon at higher frequency (anti-Stokes frequency) and the scattered molecules return to the vibrational ground state, see figure 3.8 [23].

The theory behind Raman scattering is defined based on the following manner: Considering that a diatomic molecule is illuminated using an alternate electric field E :

$$E(t) = E_0 \cos\theta(2\pi\nu t) \tag{3.5}$$

an electric dipole moment P is induced:

$$P = \alpha E \tag{3.6}$$

The schematic illustrated in figure 3.9, wherever the incident beam laser is fixated onto the sample. In place of the grating is rotating, the light will be focused or directed to the charge-coupled device (CCD) and the spectrum will be easily recorded. With the present work, we used a Horiba Jobin – Yvon HR800 Raman microscope to analyze our CeO₂ nanomaterial.

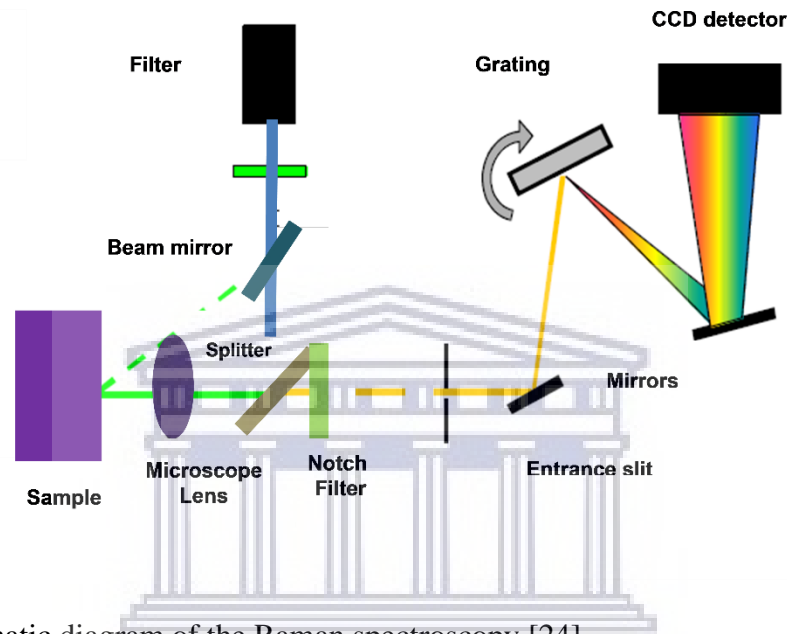


Figure 3.9: schematic diagram of the Raman spectroscopy [24].

3.2.5 X-ray photoelectron spectroscopy

X-ray photoelectron spectroscopy (XPS) is employed to analyze the elemental surface states, composition, chemical, and electronic states inside a nanomaterial. XPS is typically accepted as electron spectroscopy for chemical analysis (ESCA) [25]. It was stated in 1967 by Siegbahn and this was founded on the photoelectric effect that was described in 1905 by Sir Albert Einstein [26].

The photoelectric effect is related to the ejection of electrons from a metal surface once it is irradiated by the light. Sir Albert Einstein considered light not as a wave propagating through space, nonetheless as a collection of wave packets associated with photons with energy (E).

which is based on the following equation: $E = h\nu$ where h is the Planck constant, ν is the frequency. To eject an electron, the photon energy should be greater than the work function (ϕ) of a material. Nevertheless, if the energy is less, no electron may be ejected. As a result, the photoelectric effect equation [27] is captured as:

$$E_{k(\max)} = h\nu - \phi \quad (3.7)$$

where E_k is correlated to the maximum kinetic energy of the ejected electron. XPS is reliant on the photoemission due to the X-rays with an energy range of 100 eV- 100 keV. Accordingly, with the deeper understanding of the X-ray excitation energy in the binding energy (E_{BE}) of the precise orbital from that, an electron that is ejected may be measured employing the photoelectric effect equation. Ernest Rutherford proposed equation 3.8 as to get the BE of each of the emitted electrons [27]:

$$BE = E_p - E_{k(\max)} - \phi \quad (3.8)$$

Where E_{BE} is the energy of the emitted electron from each electron configuration inside the atom; E_p is the X-ray photon energy that is being used, E_k is the kinetic energy of the emitted electrons as measured by the instrument and lastly, ϕ is the work function of the samples. The characteristic spectral peaks observed on the XPS spectra are associated with the electronic configuration ($1s$, $2s$, $2p$, $3s$,) in atoms, and individually peak denotes the amount of the contained element. To compensate the long path length (1 m) between detectors and the sample measured, for the operation of the detectors, an ultra-high vacuum is required, otherwise, the excited electrons will result to recombination, trapping in excited states or

inelastic collision inside the material and lose kinetic energy, causing fewer electrons to escape.

3.2.6 Photoluminescence spectroscopy

PL spectroscopy is a non-destructive technique that is utilized to investigate the optical or light emission properties of nanostructures for photovoltaic and other optoelectronic applications. This technique can be used to study the electronic structures of different materials and also determine the quantum confinement effects in structures such as nanowires. In simpler terms, PL spectroscopy involves the excitation of electrons using a laser beam of known wavelength whereby the electrons absorb the laser photons and get excited into higher energy states in the conduction band. At the conduction band, these electrons de-excite through photon emission and move back into the valence band [28].

The experimental set-up

The main components of a PL system are an optical laser source, an optical system (lenses and mirrors), and a spectrophotometer as shown in the schematic diagram, figure 3.10. During PL measurement, a laser is generated at the source and is directed to the sample surface by the optical system. Upon reaching the sample, excitation and de-excitation occur resulting in the emission of a beam of luminescence photons and the optical system filters any reflected laser such that only the luminescence signal reaches the spectrometer and is processed into an electronic signal and displayed on the computer screen.

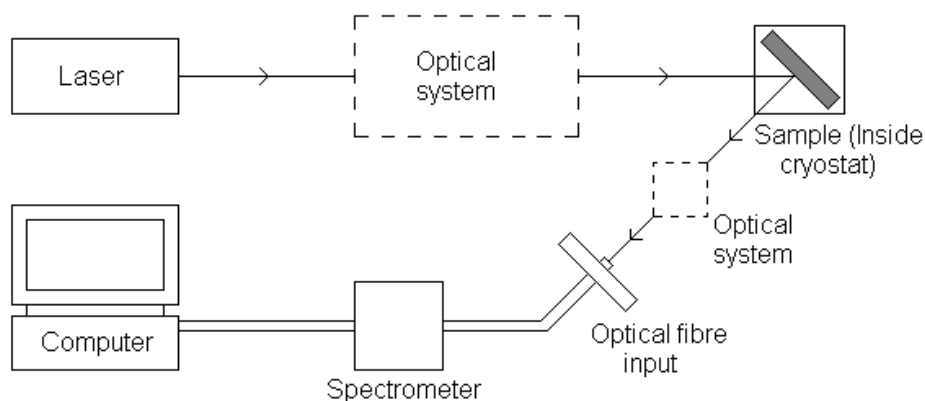


Figure 3.10: Schematic diagram Photoluminescence experimental set-up

3.2.7 Brunauer-Emmett-Teller Surface Area Analysis

The Brunauer-Emmett-Teller (BET) analysis is established on the gas molecules adsorption on a solid surface. It gives information on surface features, like the specific surface area, pore diameter, and pore volume of the materials. The BET theory was developed by Stephen Brunauer, Paul Emmett, and Edward Teller in 1938 as an addition of the Langmuir theory, which was established by Irving Langmuir in 1916 [29]. The theory of Langmuir justifies that the adsorbate acts as an ideal gas at isothermal conditions. And the amount of adsorbed adsorbate is a function of concentration or pressure, and all surface sites comprise the similar adsorption energy for the adsorbate, individually active site may be occupied by a single particle and the adsorbates form a monolayer. Whereas the BET theory is related to infinite-layer adsorption, no interaction between the individual layer and the Langmuir theory embraces on each layer. The adsorbents employed are non-corrosive gases, such as nitrogen, argon, carbon dioxide. The BET equation is set as:

$$\frac{1}{N\left(\frac{P_0}{P}\right)-1} = \frac{c-1}{NmC} \left(\frac{P}{P_0}\right) + \frac{1}{NmC} \quad (3.9)$$

where N is the gas adsorbed quantity, P and P_0 are the equilibrium and saturation pressures of the adsorbate at the temperature of adsorption, N_m is the monolayer adsorbed gas quantity and c is the BET constant. The adsorption isotherms alongside the partial pressure contain plots of $1/(N(P_0/P)-1)$.

3.3.9 Electron paramagnetic resonance spectroscopy

The theory of the electron spin resonance (ESR) is associated with the notions of nuclear magnetic resonance (NMR). Both EPR and NMR frequently focuses on relations between electromagnetic radiation and magnetic moments. As for the EPR, magnetic moments appear from electrons instead of nuclei. In brief, the EPR is used to probe paramagnetic properties of the samples and provides information related to the paramagnetic centers on various oxide surfaces, transitional metals, etc. The detected paramagnetic centers involve radicals, surface defects, metal complexes, etc. The presence of other species in the system changes the specific location of the species on a surface of the material (e.g. dopants or impurities). These additives, post-treatment such as annealing also influence the metal particle sizes.

When a composite with an unpaired electron link with a spin interacts, it generates a strong magnetic field. The spin of the unpaired electron may be prepared in only two probable alignments. The two orientations contain different magnetic potential energy that prompts a lift in the degeneracy of electron spin states, as presented in Figure 3.11. The alignment of the spin may either be parallel to the magnetic field with low energy state $m_s = -1/2$ or antiparallel to the magnetic field equivalent to high energy state $m_s = 1/2$ [30]. The difference in energy ΔE is provided by:

$$\Delta E = E_+ - E_- = h\nu = g_s \mu_B B \quad (3.10)$$

where, the h is the Planck's constant which is equal to $6.626 \times 10^{-34} \text{ J s}^{-1}$, ν is the frequency of radiation, μ_B is the Bohr magneton ($9.274 \times 10^{-24} \text{ J T}^{-1}$), B is the magnetic field strength in Tesla, and g_s is the electron spin g-factor.

During the ESR analyses the samples are exposed to a fixed microwave irradiation between a direct magnetic field in order to excite electrons in the highest occupied molecular orbitals (HOMO) to the lowest unoccupied molecular orbitals (LUMO). Because of the small magnetic field, the unpaired electrons will be aligned parallel to the applied magnetic field. The microwave irradiation generates a transformation in alignment for some of the unpaired electrons at a specific magnetic field strength, ensuing in the separation of energy states, as displayed in figure 3.11.

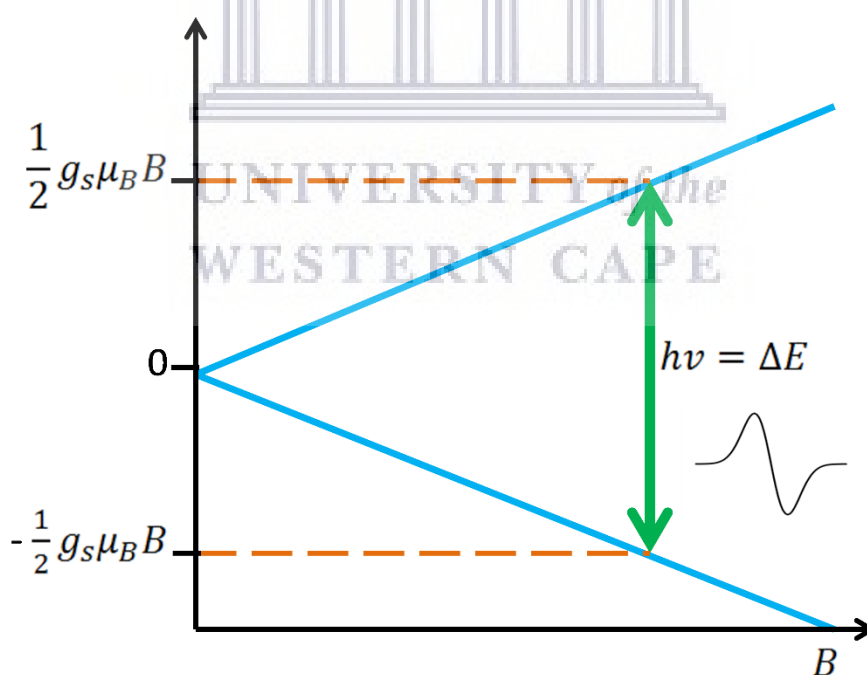


Figure 13.11: Energy levels for an electron spin ($m_s = \pm 1/2$) in an applied magnetic field B .

3.3 REFERENCES

- [1] Mai, H.X., Sun, L.D., Zhang, Y.W., Si, R., Feng, W., Zhang, H.P., Liu, H.C. and Yan, C.H., 2005. Shape-selective synthesis and oxygen storage behavior of ceria nanopolyhedra, nanorods, and nanocubes. *The Journal of Physical Chemistry B*, 109(51), pp.24380-24385.
- [2] Cundy, C.S. and Cox, P.A., 2005. The hydrothermal synthesis of zeolites: Precursors, intermediates and reaction mechanism. *Microporous and mesoporous materials*, 82(1-2), pp.1-78.
- [3] Shen, T., Wang, Q., Guo, Z., Kuang, J. and Cao, W., 2018. Hydrothermal synthesis of carbon quantum dots using different precursors and their combination with TiO₂ for enhanced photocatalytic activity. *Ceramics International*, 44(10), pp.11828-11834.
- [4] Zhou, X.D., Huebner, W. and Anderson, H.U., 2003. Processing of nanometer-scale CeO₂ particles. *Chemistry of materials*, 15(2), pp.378-382.
- [5] Masui, T., Hirai, H., Imanaka, N., Adachi, G., Sakata, T. and Mori, H., 2002. Synthesis of cerium oxide nanoparticles by hydrothermal crystallization with citric acid. *Journal of Materials Science Letters*, 21(6), pp.489-491.
- [6] Tok, A.I.Y., Du, S.W., Boey, F.Y.C. and Chong, W.K., 2007. Hydrothermal synthesis and characterization of rare earth doped ceria nanoparticles. *Materials Science and Engineering: A*, 466(1-2), pp.223-229.
- [7] Goodhew, P.J. and Humphreys, J., 2000. *Electron microscopy and analysis*. CRC Press.
- [8] Goldstein, J.I., Newbury, D.E., Echlin, P., Joy, D.C., Lyman, C.E., Lifshin, E.,

- Sawyer, L. and Michael, J.R., 2003. Qualitative X-ray analysis. In *Scanning Electron Microscopy and X-ray Microanalysis* (pp. 355-390).
- [9] Zhou, W., Apkarian, R., Wang, Z.L. and Joy, D., 2006. Fundamentals of scanning electron microscopy (SEM). In *Scanning microscopy for nanotechnology* (pp. 1-40).
- [10] OIKAWA, T., 2006. Energy dispersive x-ray spectroscopy. *Japanese journal of tribology*, 51(1), pp.33-38.
- [11] Wollman, D.A., Irwin, K.D., Hilton, G.C., Dulcie, L.L., Newbury, D.E. and Martinis, J.M., 1997. High-resolution, energy-dispersive microcalorimeter spectrometer for X-ray microanalysis. *Journal of Microscopy*, 188(3), pp.196-223.
- [12] Cairns, J.A., 1973. Characteristic X-ray production by heavy ion bombardment as a technique for the examination of solid surfaces. *Surface Science*, 34(3), pp.638-648.
- [13] Russ, J.C., 2013. *Fundamentals of Energy Dispersive X-Ray Analysis: Butterworths Monographs in Materials*. Butterworth-Heinemann.
- [14] Goldstein, J.I., Newbury, D.E., Echlin, P., Joy, D.C., Lyman, C.E., Lifshin, E., Sawyer, L. and Michael, J.R., 2003. Generation of X-Rays in the SEM Specimen. In *Scanning Electron Microscopy and X-ray Microanalysis* (pp. 271-296). Springer, Boston, MA.
- [15] Goldstein, J.I., Newbury, D.E., Michael, J.R., Ritchie, N.W., Scott, J.H.J. and Joy, D.C., 2017. *Scanning electron microscopy and X-ray microanalysis*. Springer.
- [16] Curtis, S.K., Goodhew, P.J., 1985. Specimen Preparation for Transmission Electron Microscopy of Materials. *Transactions of the American Microscopical Society* 104, 305.
- [17] Cullity, B.D., 'Elements of X-ray diffraction', 2nd edn; 1978, Reading, MA, Addison-Wesley Publishing Company Inc.

- [18] Mackay, A.L. and Pawley, G.S., 1963. Bravais lattices in four-dimensional space. *Acta Crystallographica*, 16(1), pp.11-19.
- [19] Whittaker, E.J.W., 2013. *Crystallography: an introduction for earth science (and other solid state) students*. Elsevier.
- [20] Tipa, R.S. and Baltag, O.I., 2008. STUDY ON A MODEL OF BRAGG DIFFRACTION USING MICROWAVES★. *Rom. Journ. Phys*, 53(1-2), pp.249-251.
- [21] Chowdhury, M.B., Hossain, M.M. and Charpentier, P.A., 2011. Effect of supercritical water gasification treatment on Ni/La₂O₃-Al₂O₃-based catalysts. *Applied Catalysis A: General*, 405(1-2), pp.84-92.
- [21] Raman, C.V. and Krishnan, K.S., 1928. A new class of spectra due to secondary radiation. Part I.
- [22] Smith, E. and Dent, G., 2005. The Raman experiment. *Modern Raman spectroscopy*.
- [23] Ferraro, J.R., 2003. *Introductory raman spectroscopy*. Elsevier.
- [24] Smith, E. and Dent, G., 2019. *Modern Raman spectroscopy: a practical approach*. John Wiley & Sons.
- [25] Crist, B.V., 2019. XPS in industry—Problems with binding energies in journals and binding energy databases. *Journal of Electron Spectroscopy and Related Phenomena*, 231, pp.75-87.
- [26] Joshi, M., Butola, B.S., Simon, G. and Kukaleva, N., 2006. Rheological and viscoelastic behavior of HDPE/octamethyl-POSS nanocomposites. *Macromolecules*, 39(5), pp.1839-1849.
- [27] Ma, J., Qi, Z. and Hu, Y., 2001. Synthesis and characterization of polypropylene/clay nanocomposites. *Journal of Applied Polymer Science*, 82(14), pp.3611-3617.

- [28] Schroder, D.K., 2015. Semiconductor material and device characterization. John Wiley & Sons.
- [29] Brunauer, S., Emmett, P.H. and Teller, E., 1938. Adsorption of gases in multimolecular layers. *Journal of the American chemical society*, 60(2), pp.309-319.
- [30] Weil, J.A. and Bolton, J.R., 2007. *Electron paramagnetic resonance: elementary theory and practical applications*. John Wiley & Sons.



CHAPTER 4

MORPHOLOGICAL, OPTICAL AND STRUCTURAL PROPERTIES OF CeO₂ NANOPARTICLES

4.1 INTRODUCTION

CeO₂ nanoparticles have attracted much attention due to their reported unique structure and physical properties attributed to the grain boundary and grain-size dependent non-stoichiometry [1]. Numerous methods have been developed for the synthesis of nanostructured material for various applications: liquid phase methods (hydrothermal, solvothermal, sol-gel) [2][3][4], and gas-phase methods (spray pyrolysis, electrospinning, CVD) [5][6][7]. Since the physical and chemical properties of the nanocrystalline material are different than that of bulk or microcrystalline, it is very important to study the variation in these properties in the nanoparticle range. This can lead to optimization of the properties obtained from nanoceria for specific applications of nanocrystalline materials in gas sensors and many newer applications. Although the properties are rarely investigated, because of the difficulties in controlling monodisperse particle size distribution at that range.

Up to now, several routes have been reported for the synthesis of CeO₂ nanostructures including solid-state reaction [8], co-precipitation [9], and sol-gel methods [10]. However, these methods typically require long reaction times (20-60 hours), expensive equipment with complex reaction mechanisms with multiple precursors to form Ceria. Moreover, the resultant products are not stable and well shape-controlled due to the temperature, concentration, and pH. Recently, CeO₂ nanostructures were shown to be readily synthesized via hydrothermal method. The method has attracted interest because of low fabrication costs,

ease of processing, high stability, and good detection capabilities [11][12]. This is due to the low temperature and high-pressure cooking process of the hydrothermal method that forms highly crystalline CeO₂ nanoparticles with a bandgap of 3.44eV [13].

Numerous researchers have shown that the reversible interaction of the gas with the surface of the material is a characteristic of conductometric semiconducting metal oxide gas sensors [14]. This reaction can be influenced by many factors, including internal and external causes, such as natural properties of base materials, surface areas, and microstructure of sensing layers, surface additives, temperature, and humidity, etc. Many papers about metal oxide gas sensors have been published in recent years [15][16][17][18]. The important parameters of gas sensors are sensitivity, selectivity, recovery, and stability, etc.

In this chapter, we report on the morphological, structural optical, and magnetic properties of CeO₂ nanoparticles prepared by a hydrothermal method. This study shows the annealing has significant optical and magnetic properties of CeO₂ nanoparticles.

4.2 EXPERIMENTAL DETAILS

CeO₂ nanoparticles were synthesized using a hydrothermal method. Cerium nitrate (Ce(NO₃)₂·6H₂O; 432.2 g/mole; 99.9% purity) and Sodium hydroxide (NaOH; 40 g/mole; 99.9% purity) were purchased from Sigma Aldrich Chemicals. These chemicals were used without further purification. Cerium oxide nanoparticles were prepared using a hydrothermal procedure [19]. In the synthesis process, 0.217 g of Cerium nitrate hexahydrate [Ce(NO₃)₂·6H₂O] and 0.280 g of Sodium hydroxide (NaOH) were taken in 5ml and 35ml of distilled water respectively. Then, these two solutions were mixed and this mixture was stirred at room temperature for 30 min. The solution obtained was transferred to a Teflon

lined autoclave (Parr Instruments) which was maintained at a constant temperature of 180 °C and prepared for 10 hrs. After the reaction, the contents were removed from the oven to cool to room temperature. The collected products were washed several times with deionized water and dried at 60 °C for 24 h to achieve the final products of CeO₂. Finally, the product was annealed at 300, 500, and 700 °C in an oven (heating rate: 5 °C/min) in air atmosphere for 2 h.

The morphology of the nanoparticles was examined by field-emission scanning electron microscopy (Auriga ZEISS) with a beam energy of 3 keV. A thin layer of Au was coated on the top of the samples to improve resolution and prevent charging. The crystal structure of the as-synthesized product was analyzed by x-ray diffraction analysis using a Panalytical X'pert PRO PW 3040/60 X-ray diffractometer with a Cu K_α ($\lambda = 0.154$ nm) monochromated radiation source. X-ray diffraction (XRD) spectra were collected in 2 θ reflection geometry, operating at 45 kV and 40 mA. The XRD spectra were collected at 2 θ - values ranging from 10 – 90 ° with a step size of 0.02 °. A high-resolution transmission electron microscope (HRTEM - JEOL-2000) was used to examine the microscopic structure of the product. The chemical compositions were determined using an energy dispersive x-ray spectrometer (EDS) attached to the SEM and HRTEM instruments, respectively. The optical features were measured using Jobin-Yvon NanoLog (France) photoluminescence (PL) spectrometer. Nitrogen (N₂) adsorption-desorption isotherms were conducted by utilizing a Micromeritics TRISTAR 3000 surface area analyzer (USA). Chemical composition was probed using PHI 5000 Versaprobe-Scanning ESCA Microprobe instrument (USA), X-ray photoelectron spectroscopy analysis. The paramagnetic and point defects analyses were examined using a JEOL X-band JES FA 200 electron paramagnetic resonance (EPR, Japan) spectrometer at

room temperature. Magnetization measurements were conducted using a Lakeshore 735 vibrating sample magnetometer (VSM) at room temperature. For details of how the measurements were done, see electronic supplementary information (ESI).

4.3 RESULTS AND DISCUSSION

SEM images of the as-prepared and annealed CeO₂ nanoparticles at 300 °C are shown in figure 4.1. For the as-prepared CeO₂ samples, porous agglomerates of nanoparticles are observed. However, in the case of the samples calcined at 300 °C, much larger particles are observed. This might be due to the aggregation of the CeO₂ into larger clusters during the annealing process. A few researchers have indicated that agglomeration of these nanoparticles will lead to failure or poor chemiresistive gas sensing performances due to the reduction of catalytic properties [20][21][22]. Korotcenkov *et al.* [23] also reported that agglomeration greatly affects gas sensing properties. Since gas sensing occurs on the surface of the metal oxide, the surface volume action area influences the performance of the sensor. The agglomeration of nanoparticles produces secondary particles which decrease the surface interaction volume, thus reducing the chemiresistivity.

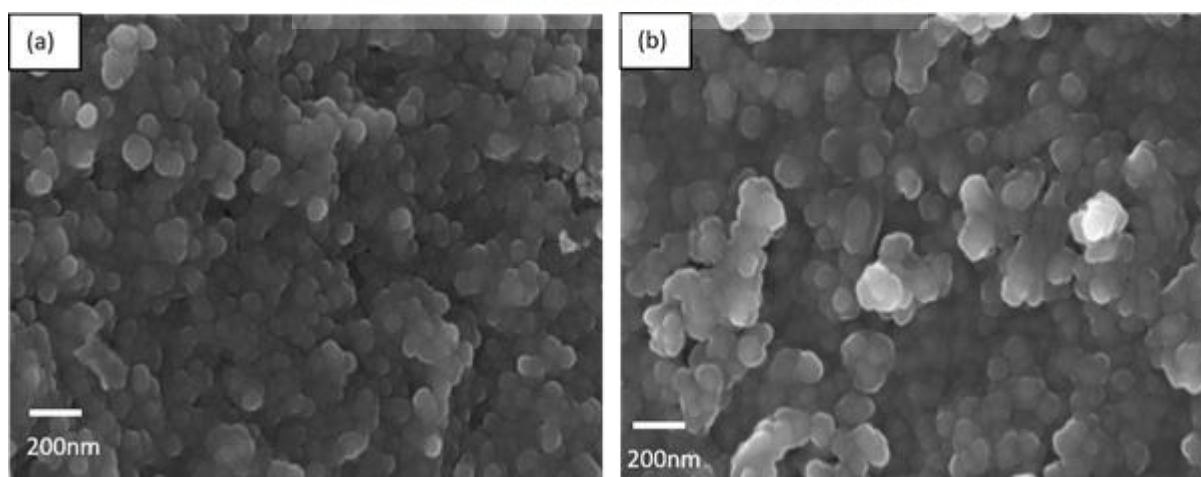
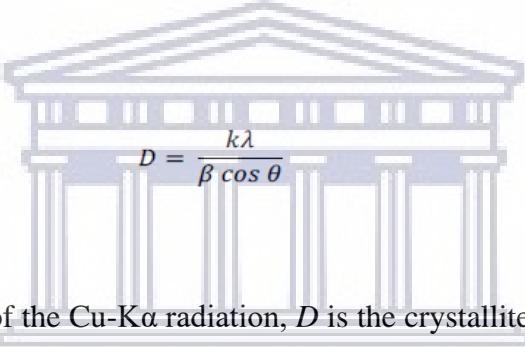


Figure 4.1: SEM images of (a) as-prepared and (b) annealed at 300 °C CeO₂ nanoparticles.

The crystal structure and phase evolution of the nanostructures during annealing were studied using the XRD technique as shown in the figure. 4.2. The main diffraction peaks were found at $2\theta \approx 28.56^\circ$; 33.08° ; 47.47° ; 56.36° and 59.09° correspond to the (111), (200), (220), (311), and (222) diffraction planes, respectively. All the diffraction peaks were indexed to the cubic fluorite structure (JCPDS card number 34-0394, and No.65-2975). Upon annealing, the intensity of the peaks slightly increases, denoting higher crystallinity. The average crystallite size (D) of CeO₂ nanoparticles were calculated by the Debye-Scherrer equation [24].


$$D = \frac{k\lambda}{\beta \cos \theta} \quad (4.1)$$

where λ is the wavelength of the Cu-K α radiation, D is the crystallite size, K is a constant and its value is taken as 0.9, θ is the diffraction angle and β is the full-width at half maximum (FWHM).

The average crystallite size is 9.4nm and 12.8, respectively for as-prepared CeO₂ nanoparticles and that calcined at 300 °C.

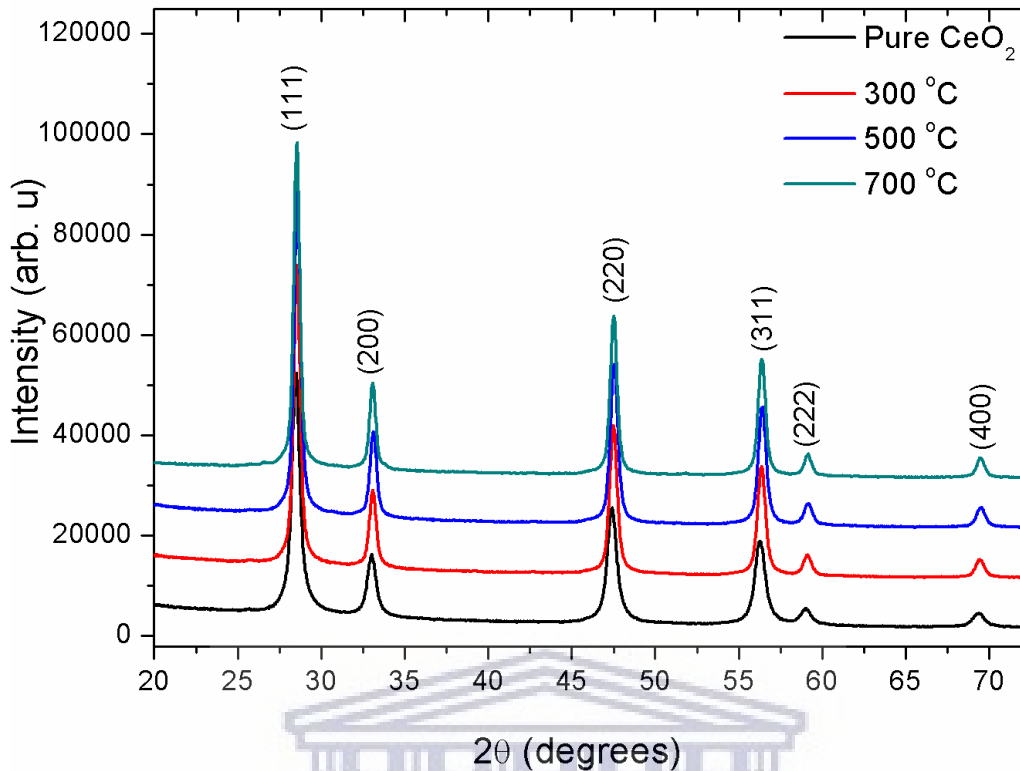


Figure 4.2: XRD patterns of as-prepared CeO₂ nanoparticles synthesized by the hydrothermal method compared with that calcined at different temperatures.

The structure of the nanoparticles synthesized was further characterized by TEM combined with the use of SAED patterns. Figure 4.3 (a) shows the low magnification TEM image of the as-prepared CeO₂ nanoparticles. The TEM micrographs confirm that the synthesized nanoparticles are in the range of 12 - 20 nm in size, which is in good agreement with that obtained by Chen et al [25]. While figure 4.3b and c display the high-resolution micrographs of the as-prepared CeO₂ and that annealed at 700 °C. The presence of an amorphous phase is also visible and is confirmed by the diffused Debye ring in the selected area electron diffraction (SAED) patterns, shown in the insets of figure 4. 3(b) and (c). Upon annealing at 700 °C figure 4.4(c), the size of the CeO₂ nanoparticles increases to an average diameter of

18 nm. The diffraction pattern of the 700 °C annealed sample indicates bright and continuous rings; confirming that the material is polycrystalline.

The composition of the CeO₂ nanoparticles was investigated by EDS. An EDS spectrum is shown below in figure 4.4. The major components of the CeO₂ nanoparticles, as expected, are cerium and oxygen. The copper peak in the EDS spectra is likely coming from the copper grids used for the TEM sample preparation. The chemical composition of the nanoparticles determined by the EDS is to be close to CeO₂, Table 4.1.

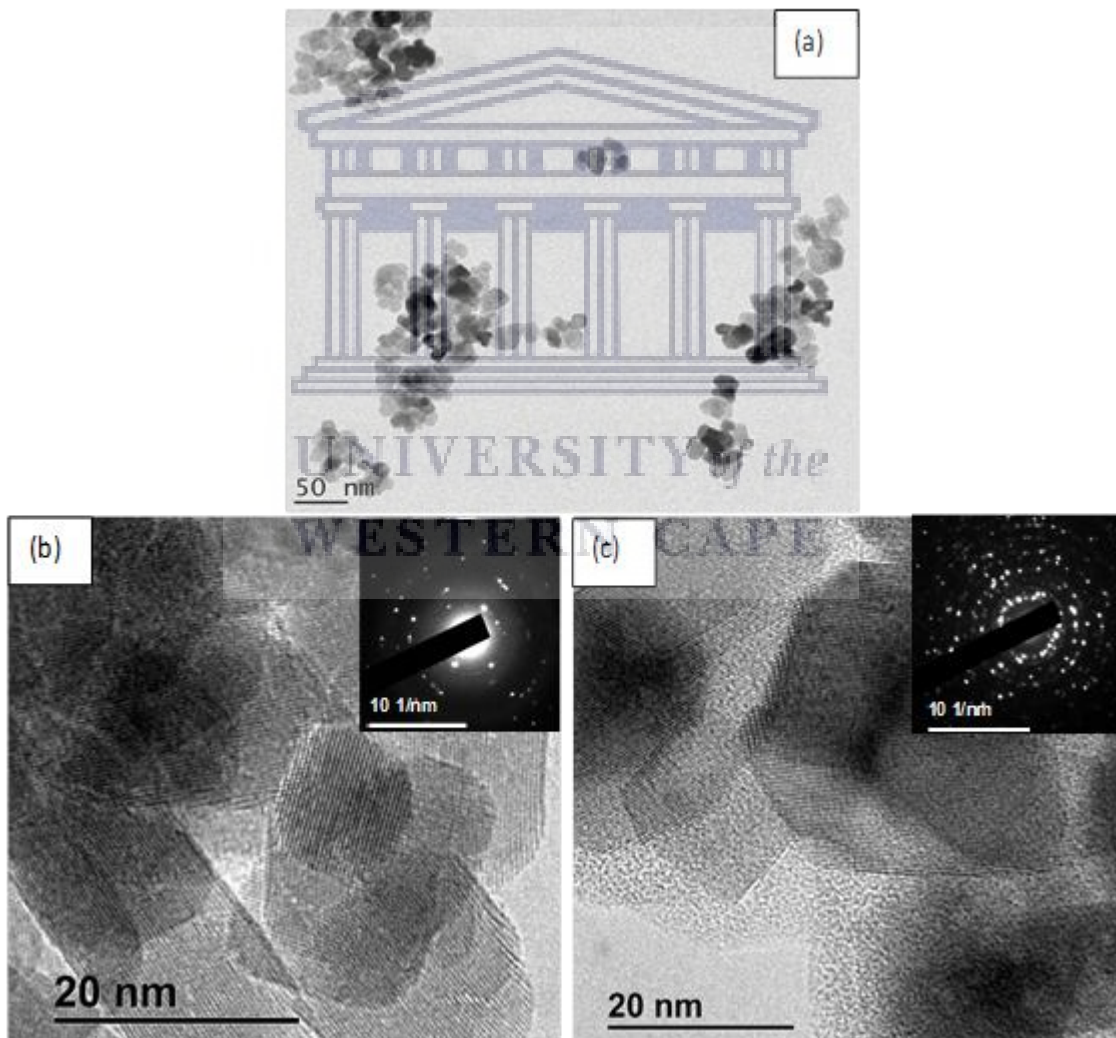


Figure 4.3: (a) shows the low magnification TEM image of the as-prepared CeO₂ nanoparticles, (b) and (c) high resolution TEM images of the as-prepared and annealed at 700 °C CeO₂ nanoparticles with a SAED pattern of the nanoparticles.

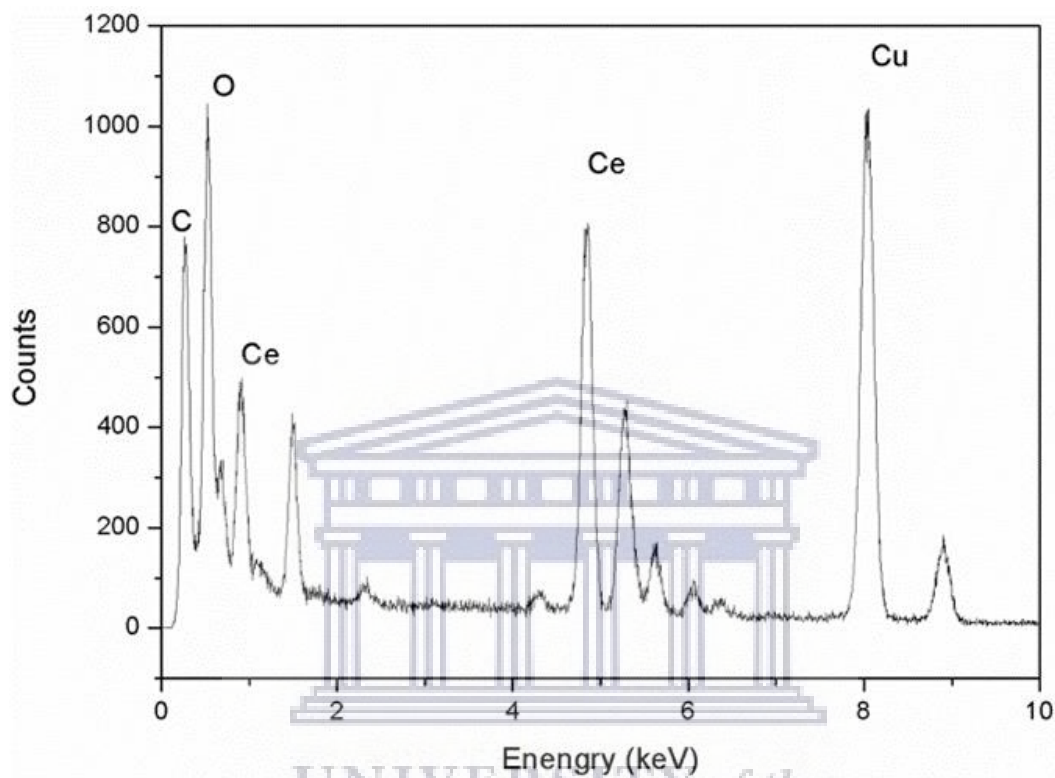


Figure 4.4: EDS analysis of the as-synthesized CeO₂ nanoparticles.

Table 4.1: Quantitative analysis of the CeO₂ nanoparticles.

Element	Wt%	Wt% Sigma	Ratio
O	18.02	0.36	2
Ce	81.98	0.36	1
Total:	100.00		1:2

The Raman spectra in Figure. 4.5 provide information on the intrinsic defect sites on the annealed CeO₂. A strong Raman band positioned at approximately 462 cm⁻¹ corresponds to the F_{2g} mode of the CeO₂ cube structure [26]. This band is associated with asymmetric breathing mode of the oxygen ions around each Ce⁴⁺ cation [26] [27]. The broad peak situated at approximately 550 – 600 cm⁻¹ is related to the defect-induced mode (i.e. oxygen vacancies) [28]. As shown in figure 4.5, upon annealing a trivial shift and increase in the intensity of the F_{2g} mode are observed due to the structural ordering. Moreover, the intensity of the peak related to the oxygen vacancies (V_O) is trivial for pure CeO₂, even after annealing as shown in the inset.

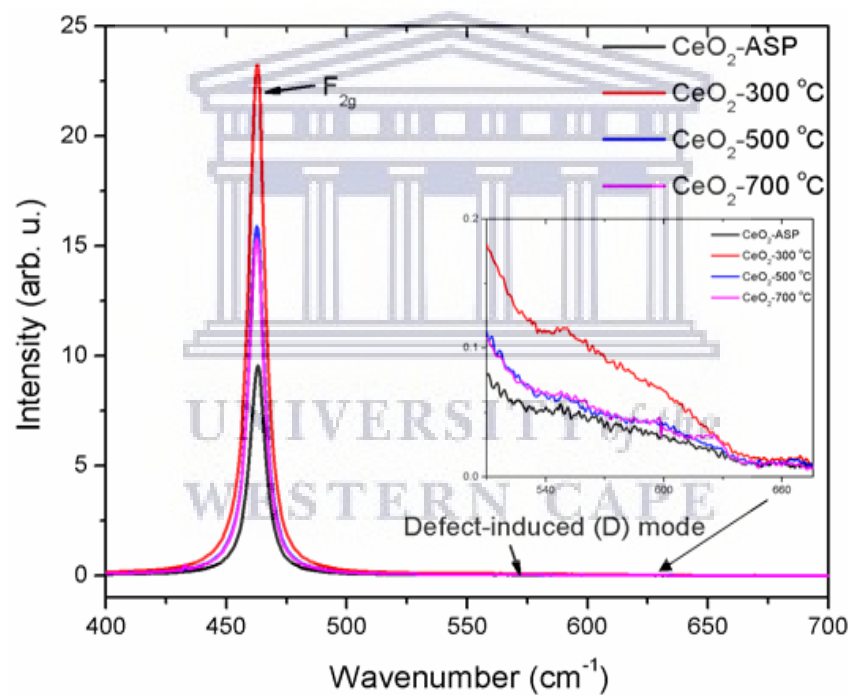


Figure 4.5: Raman spectra of the as-prepared CeO₂ nanostructures compared with that annealed at three different temperatures. Insets in figure 3.5 correspond to defect induced mode.

To explore what would be the nature of the influence of the defects concentration on the gas sensing properties, XPS analyses were carried out on the samples. Figure 4.6 represents the oxygen (O 1s) core level spectra of the as-prepared and annealed CeO₂ nanostructures at

various temperatures. The O 1s core-level spectra of the as-prepared CeO₂ spectrum displayed in figure 4.6 can be deconvoluted into three symmetrical peaks, located at lower binding (O_c) 529.4 eV, medium binding energy (O_a) 530.1 eV, and higher binding energy (O_b) 531.30 eV which are related to adsorbed oxygen, lattice oxygen in CeO₂, and oxygen vacancies (V_O) [29], respectively. Upon annealing at 500 °C, figure 4.6c, the peak broadening appears, however, at higher annealing temperature (700 °C), figure. 4.6d, the spectrum becomes narrow, due to improved crystal quality (see also XRD results).

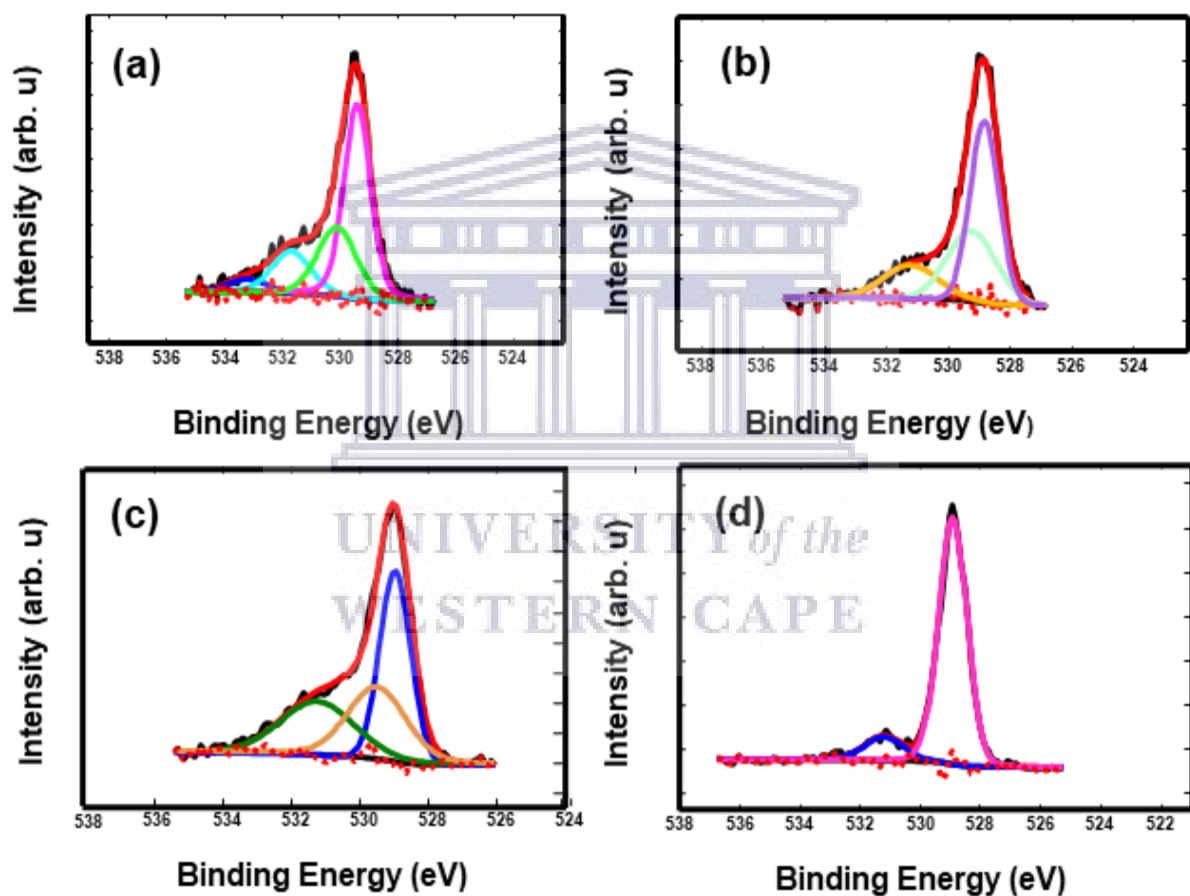
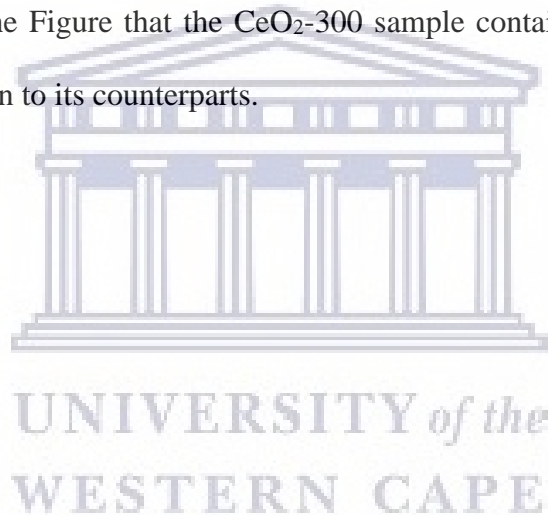


Figure 4.6: O 1s core levels of (a) CeO₂-ASP, (b) CeO₂-300 °C, (c) CeO₂-500 °C and (d) CeO₂-700 °C.

To further substantiate the XPS results, the more conclusive study of defect states was done using the PL. The PL spectra of the respective as-prepared and annealed NPS of CeO₂ at various temperatures are shown in figure 4.7. It is clear from figure 4.7 that all samples reveal a UV emission (around 410-415 nm) and a green emission (defect-related) around 500-675 nm. The UV emission at 410 nm is attributed to the excitonic recombination, which matches well with the near-band-edge (NBE) emission of CeO₂ [30]. The deconvoluted spectrum (results not shown) using Gaussian fit for the green emission peaks shows three peaks at 560, 590, and 643 nm for CeO₂ related to oxygen vacancies (V_O) in the crystal and cubic CeO₂ phase. To quantify the point defects we calculated the UV/Vis ratio as shown in Figure 4.7 (b). It is clear from the Figure that the CeO₂-300 sample contain high concentration of point defects in comparison to its counterparts.



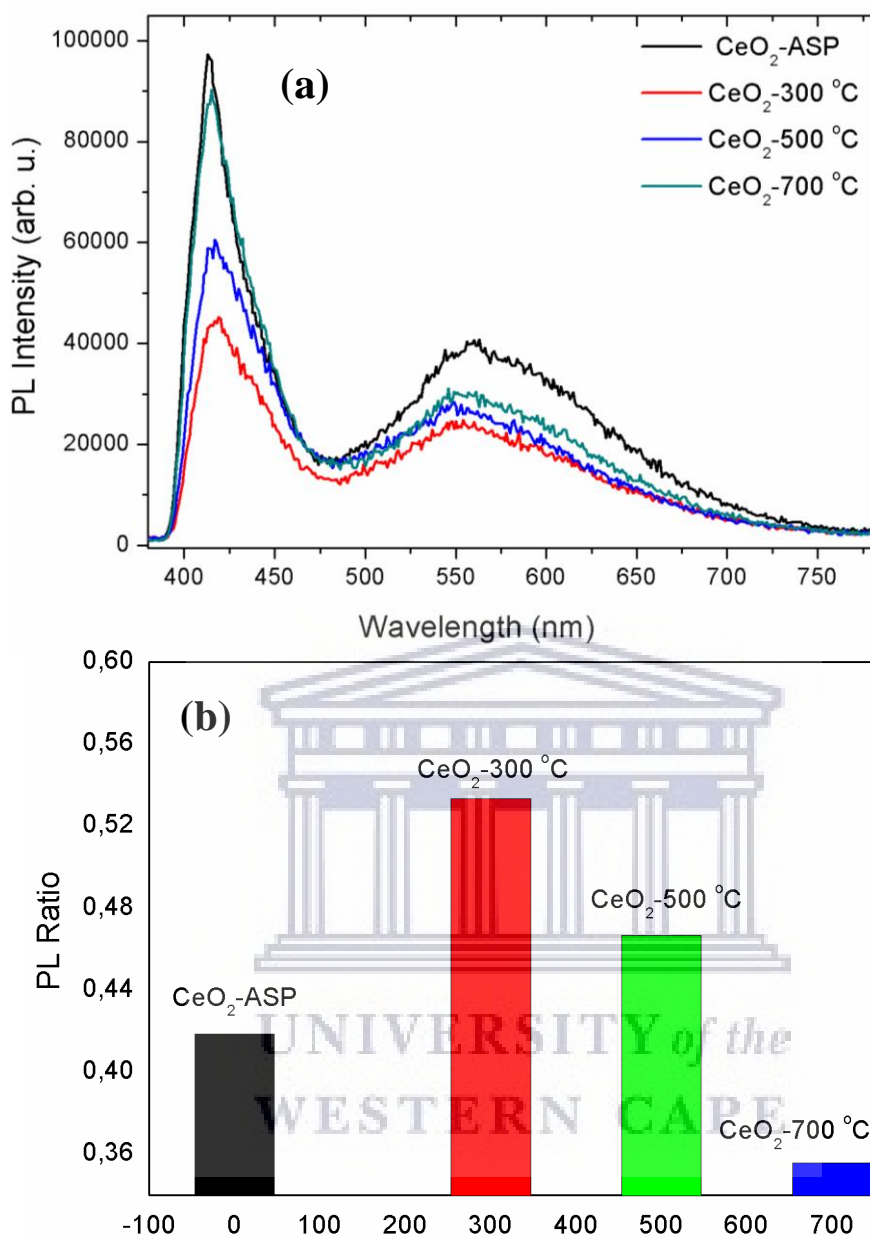


Figure 4.7: (a) Room Temperature PL spectra of as-prepared and annealed CeO₂ nanostructures and (b) PL intensity ratio of CeO₂ based samples.

To understand surface behavior of the material for sensing, BET surface area and porosity analyses of the as-prepared and annealed CeO₂ nanostructure were examined by the nitrogen adsorption/desorption experiment and the obtained results are shown in figure 4.8 and table 4.2, respectively. As shown in Figure. 4.8, the N₂ adsorption/desorption isotherms of the

annealed CeO₂ NPs display characteristics of mesoporous materials. Table 4.2 shows that the surface areas of the CeO₂ NPS decrease with annealing temperatures, while the pore diameter increases, which will be beneficial gas adsorption in gas sensing.

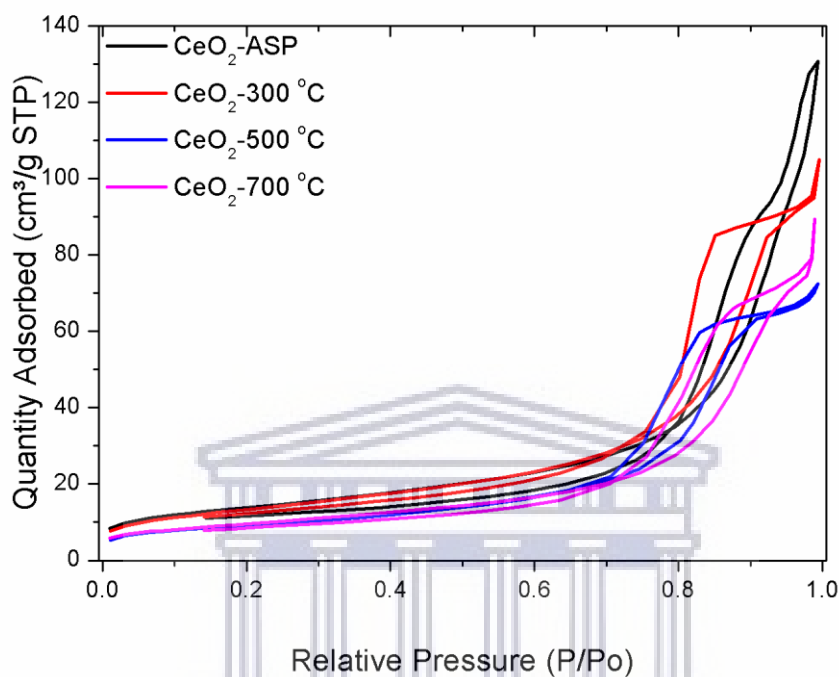


Figure 4.8: N₂ adsorption isotherms of un-annealed and annealed CeO₂, nanostructures.

Table 4.2: Summary of BET surface area analyses on the as-prepared and annealed CeO₂ nanostructures at various temperatures.

Sample	BET Surface area (m ² /g)	Pore Diameter (nm)	Pore Volume (cm ³ /g)
CeO ₂ -ASP	49.4280 ± 0.0905	18.0044	0.205801
CeO ₂ -300 °C	48.5683 ± 0.0887	13.6967	0.168914
CeO ₂ -500 °C	33.1726 ± 0.0608	12.0661	0.120056
CeO ₂ -700 °C	34.4341 ± 0.0905	15.9023	0.143396

The magnetization at room temperature for as-prepared and annealed CeO₂ structures were measured using a vibrating sample magnetometer (VSM). As presented in figure 4.9, it is clear that the CeO₂ samples show weak room temperature ferromagnetism (RTFM) features at low field, dominated by paramagnetism (PM) with very low coercivity and virtually linear increase of saturation magnetization. The domination of PM is due to a higher concentration of Ce⁴⁺ ions and as well as the low relative concentration of surface defects on clusters site (see Raman, PL, and XPS analyses) since non-magnetic and Ce⁴⁺ ions have zero magnetic moment. It is well documented that oxygen vacancies (V_O) and defects at the surface/interfaces allow a ferromagnetic coupling, giving rise to the RTFM. An RTFM with some PM behavior has been reported previously by Dimri et al. [31] for 20% Nd and Sm doped CeO₂. It is clear that upon annealing at higher temperatures, the appearance of FM is undeniably trivial, while that of PM is significant, disclosing that the concentration of Ce⁴⁺ ions in CeO₂ is substantial as confirmed by XPS analyses.

It is notable to note that upon annealing at 300 °C, the CeO₂-300 °C demonstrated higher coercivity and saturation magnetization (M_S) of 2749.1 Oe and 0.20973 emu/g compared to its counterparts. The observed M_S values are comparable to those reported by other researchers for CeO₂ [32][33]. At higher annealing temperatures (500-700 °C), the M_S and coercivity decrease, displaying values of 0.20881 emu/g and 454.09 Oe at 500 °C and 0.19061 emu/g and 268.64 Oe at 700 °C, respectively. This is most likely due to a decrease in the relative concentration of V_O induced by the transformation of Ce³⁺ to Ce⁴⁺ and higher possibility of a super exchange interaction contributing to antiferromagnetic behavior. Phokha et al. [34] reported that at higher annealing temperature the M_S decreases.

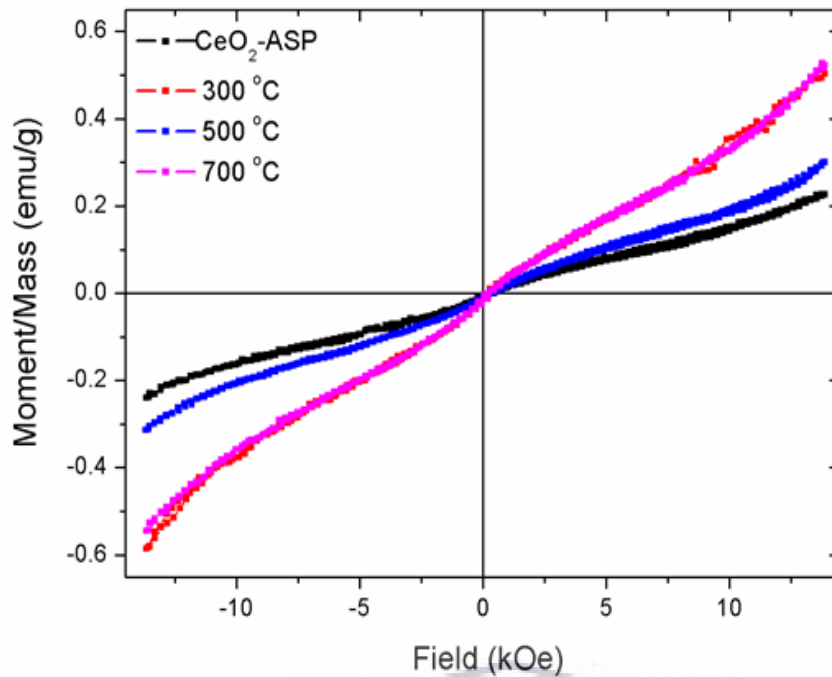


Figure 4.9: Room temperature magnetic field-dependent magnetization displaying a comparison of hysteresis in nanostructures annealed CeO₂ at various temperatures.

To further validate the VSM results, the more conclusive analyses were performed with EPR to classify the point defects in the samples. As shown in figure 4.10, the as-prepared CeO₂ NPs display a single EPR signal together with a sharper peak at 320 nm. This EPR signal is customarily measured as one of the appearances of FM in metal oxide materials [35][36]. The sharper peak can be ascribed to a paramagnetic feature, induced by clustering of CeO₂ NPs. However, upon annealing the CeO₂ at 300-500 °C, the intensity of the sharper peak reduces slightly. Additionally, the g-factor values shifted from 2.07562 (as-prepared) to 2.04454, 2.0068, and 1.99751 after annealing at 300, 500, and 700 °C, respectively. At higher annealing temperature (700 °C), the broad peak related to FMR becomes narrow and sharp, denoting that PM behaviour is dominating.

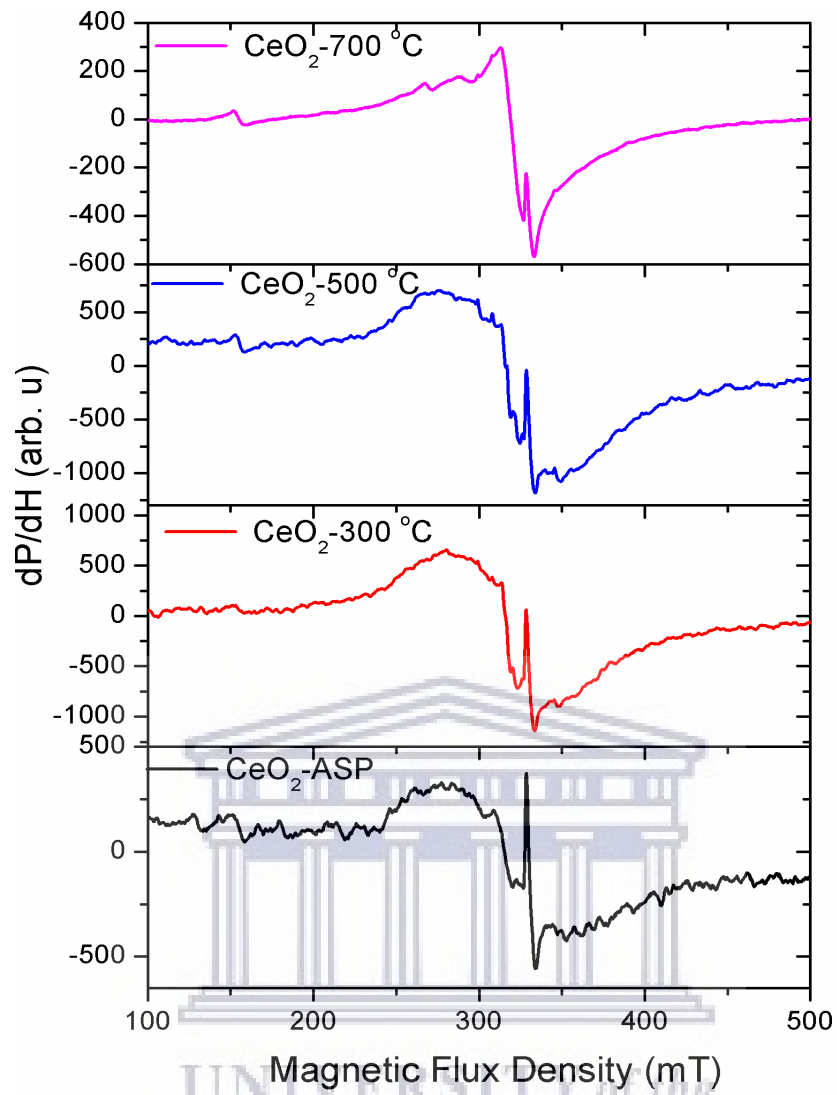


Figure. 4.10: EPR spectra of the as-prepared and annealed CeO₂ nanostructures at various temperatures.

4.4 CONCLUSIONS

CeO₂ nanoparticles were successfully synthesized by the hydrothermal method and annealed at various temperatures. The structural, electronic, and optical properties of the nanoparticles were characterized by various techniques. SEM images showed the formation of large agglomerated spheroidal structure with an average particle size ~10 nm. TEM images display that the particles are nearly spherical in shape. EDS analysis showed that the samples are purely Ce and O with a 1:2 weight ratio. XRD studies revealed that the CeO₂ nanoparticles are polycrystalline in nature and have a face centered cubic structure. The particle sizes for as-prepared sample and annealed sample were ~9.4nm and ~12.8nm, respectively. Annealing increases, the particle size and agglomeration resulting in the formation of secondary particles. Two intrinsic sites are observed from Raman spectra, one at 462 cm⁻¹ corresponding to the F_{2g} mode and the other at 550-600 cm⁻¹ related to defect-induced mode. There is a shift and increase in the intensity of the defects sites upon annealing. All the samples have two emission bands, UV emission at 410-415 nm and a green emission due to the presence of oxygen vacancy and oxygen interstitial defects at 500-650 nm. The emission intensity of the defect peak increases with the increase of annealing temperature, which indicates that the concentrations of oxygen vacancies increase with the annealing temperature increase. It is ascribed to the valence transition from Ce⁴⁺ to Ce³⁺, which also is consistent with the XPS results. The material depicted mesoporous characteristics shown by adsorption-desorption isotherm. The VSM showed weak RTFM and a dominant PM with very low coercivity and linear increase of saturation magnetization. Although, there is a decrease in the M_s value with the increase of the annealing temperature subsequent to the decrease in concentration of the V_O. This is further substantiated by the single sharp peak EPR signal

related to PM feature, that decreases slightly in intensity upon annealing. Moreover, our findings also revealed that the annealing temperature plays a vital role in tempering the surface defects, structure, particle size, and CeO₂ valence states.



4.4 REFERENCES

- [1] Gleiter, H., Weissmüller, J., Wollersheim, O. and Würschum, R., 2001. Nanocrystalline materials: a way to solids with tunable electronic structures and properties. *Acta materialia*, 49(4), pp.737-745.
- [2] Semagina, N. and Kiwi-Minsker, L., 2009. Recent advances in the liquid-phase synthesis of metal nanostructures with controlled shape and size for catalysis. *Catalysis Reviews*, 51(2), pp.147-217.
- [3] Feng, S. and Xu, R., 2001. New materials in hydrothermal synthesis. *Accounts of chemical research*, 34(3), pp.239-247.
- [4] Kaviyarasu, K., Manikandan, E., Paulraj, P., Mohamed, S.B. and Kennedy, J., 2014. One dimensional well-aligned CdO nanocrystal by solvothermal method. *Journal of alloys and compounds*, 593, pp.67-70.
- [5] Swihart, M.T., 2003. Vapor-phase synthesis of nanoparticles. *Current Opinion in Colloid & Interface Science*, 8(1), pp.127-133.
- [6] Kim, S.H., Liu, B.Y.H. and Zachariah, M.R., 2002. Synthesis of nanoporous metal oxide particles by a new inorganic matrix spray pyrolysis method. *Chemistry of materials*, 14(7), pp.2889-2899.
- [7] Khorami, H.A., Keyanpour-Rad, M. and Vaezi, M.R., 2011. Synthesis of SnO₂/ZnO composite nanofibers by electrospinning method and study of its ethanol sensing properties. *Applied surface science*, 257(18), pp.7988-7992.
- [8] Yu, X., Li, F., Ye, X., Xin, X. and Xue, Z., 2000. Synthesis of cerium (IV) oxide ultrafine particles by solid-state reactions. *Journal of the American Ceramic Society*, 83(4), pp.964-966.

- [9] Shih, C.J., Chen, Y.J. and Hon, M.H., 2010. Synthesis and crystal kinetics of cerium oxide nanocrystallites prepared by co-precipitation process. *Materials Chemistry and Physics*, 121(1-2), pp.99-102.
- [10] He, H.W., Wu, X.Q., Ren, W., Shi, P., Yao, X. and Song, Z.T., 2012. Synthesis of crystalline cerium dioxide hydrosol by a sol–gel method. *Ceramics International*, 38, pp.S501-S504.
- [11] Korotcenkov, G., 2007. Metal oxides for solid-state gas sensors: What determines our choice?. *Materials Science and Engineering: B*, 139(1), pp.1-23.
- [12] Fine, G.F., Cavanagh, L.M., Afonja, A. and Binions, R., 2010. Metal oxide semiconductor gas sensors in environmental monitoring. *sensors*, 10(6), pp.5469-5502.
- [13] Phoka, S., Laokul, P., Swatsitang, E., Promarak, V., Seraphin, S. and Maensiri, S., 2009. Synthesis, structural and optical properties of CeO₂ nanoparticles synthesized by a simple polyvinyl pyrrolidone (PVP) solution route. *Materials Chemistry and Physics*, 115(1), pp.423-428.
- [14] Barsan, N., Koziej, D. and Weimar, U., 2007. Metal oxide-based gas sensor research: How to?. *Sensors and Actuators B: Chemical*, 121(1), pp.18-35.
- [15] Korotcenkov, G., 2005. Gas response control through structural and chemical modification of metal oxide films: state of the art and approaches. *Sensors and Actuators B: Chemical*, 107(1), pp.209-232.
- [16] Rothschild, A. and Komem, Y., 2004. The effect of grain size on the sensitivity of nanocrystalline metal-oxide gas sensors. *Journal of Applied Physics*, 95(11), pp.6374-6380.
- [17] Barreca, D., Comini, E., Ferrucci, A.P., Gasparotto, A., Maccato, C., Maragno, C., Sberveglieri, G. and Tondello, E., 2007. First example of ZnO– TiO₂ nanocomposites

- by chemical vapor deposition: structure, morphology, composition, and gas sensing performances. *Chemistry of Materials*, 19(23), pp.5642-5649.
- [18] Yamazoe, N. and Shimanoe, K., 2009. New perspectives of gas sensor technology. *Sensors and Actuators B: Chemical*, 138(1), pp.100-107.
- [19] Yang, Z., Zhou, K., Liu, X., Tian, Q., Lu, D. and Yang, S., 2007. Single-crystalline ceria nanocubes: size-controlled synthesis, characterization and redox property. *Nanotechnology*, 18(18), p.185606.
- [20] Kašpar, J., Fornasiero, P. and Hickey, N., 2003. Automotive catalytic converters: current status and some perspectives. *Catalysis today*, 77(4), pp.419-449.
- [21] Izu, N., Shin, W., Murayama, N. and Kanzaki, S., 2002. Resistive oxygen gas sensors based on CeO₂ fine powder prepared using mist pyrolysis. *Sensors and Actuators B: Chemical*, 87(1), pp.95-98.
- [22] Zhou, X.D., Huebner, W. and Anderson, H.U., 2002. Room-temperature homogeneous nucleation synthesis and thermal stability of nanometer single crystal CeO₂. *Applied Physics Letters*, 80(20), pp.3814-3816.
- [23] Korotcenkov, G., 2008. The role of morphology and crystallographic structure of metal oxides in response of conductometric-type gas sensors. *Materials Science and Engineering: R: Reports*, 61(1-6), pp.1-39.
- [24] Koc, R., 1998. Kinetics and phase evolution during carbothermal synthesis of titanium carbide from ultrafine titania/carbon mixture. *Journal of materials science*, 33(4), pp.1049-1055.
- [25] Chen, H.I. and Chang, H.Y., 2004. Homogeneous precipitation of cerium dioxide nanoparticles in alcohol/water mixed solvents. *Colloids and Surfaces A: Physicochemical and Engineering Aspects*, 242(1-3), pp.61-69.

- [26] Zdravković, J., Simović, B., Golubović, A., Poleti, D., Veljković, I., Šćepanović, M. and Branković, G., 2015. Comparative study of CeO₂ nanopowders obtained by the hydrothermal method from various precursors. *Ceramics International*, 41(2), pp.1970-1979.
- [27] Swatsitang, E., Phokha, S., Hunpratub, S. and Maensiri, S., 2016. Characterization of Sm-doped CeO₂ nanoparticles and their magnetic properties. *Physica B: Condensed Matter*, 485, pp.14-20.
- [28] Meng, F., Zhang, C., Fan, Z., Gong, J., Li, A., Ding, Z., Tang, H., Zhang, M. and Wu, G., 2015. Hydrothermal synthesis of hexagonal CeO₂ nanosheets and their room temperature ferromagnetism. *Journal of Alloys and Compounds*, 647, pp.1013-1021.
- [29] Mai, H.X., Sun, L.D., Zhang, Y.W., Si, R., Feng, W., Zhang, H.P., Liu, H.C. and Yan, C.H., 2005. Shape-selective synthesis and oxygen storage behavior of ceria nanopolyhedra, nanorods, and nanocubes. *The Journal of Physical Chemistry B*, 109(51), pp.24380-24385.
- [30] Wang, L., Meng, F., Li, K. and Lu, F., 2013. Characterization and optical properties of pole-like nano-CeO₂ synthesized by a facile hydrothermal method. *Applied surface science*, 286, pp.269-274.
- [31] Dimri, M.C., Khanduri, H., Kooskora, H., Subbi, J., Heinmaa, I., Mere, A., Krustok, J. and Stern, R., 2012. Ferromagnetism in rare earth doped cerium oxide bulk samples. *physica status solidi (a)*, 209(2), pp.353-358.
- [32] Niu, G., Hildebrandt, E., Schubert, M.A., Boscherini, F., Zoellner, M.H., Alff, L., Walczyk, D., Zaumseil, P., Costina, I., Wilkens, H. and Schroeder, T., 2014. Oxygen vacancy induced room temperature ferromagnetism in Pr-doped CeO₂ thin films on silicon. *ACS applied materials & interfaces*, 6(20), pp.17496-17505.

- [33] Swatsitang, E., Phokha, S., Hunpratub, S. and Maensiri, S., 2016. Characterization of Sm-doped CeO₂ nanoparticles and their magnetic properties. *Physica B: Condensed Matter*, 485, pp.14-20.
- [34] Phokha, S., Swatsitang, E. and Maensiri, S., 2015. Room-temperature ferromagnetism in pure CeO₂ nanoparticles prepared by a simple direct thermal decomposition. *Electronic Materials Letters*, 11(6), pp.1012-1020.
- [35] Wang, L. and Meng, F., 2013. Oxygen vacancy and Ce³⁺ ion dependent magnetism of monocrystal CeO₂ nanopoles synthesized by a facile hydrothermal method. *Materials Research Bulletin*, 48(9), pp.3492-3498.
- [36] Nkosi, S.S., Kortidis, I., Motaung, D.E., Malgas, G.F., Keartland, J., Sideras-Haddad, E., Forbes, A., Mwakikunga, B.W., Sinha-Ray, S. and Kiriakidis, G., 2013. Orientation-dependent low field magnetic anomalies and room-temperature spintronic material—Mn doped ZnO films by aerosol spray pyrolysis. *Journal of alloys and compounds*, 579, pp.485-494.

CHAPTER 5

GAS SENSING CHARACTERISTICS OF CeO₂ NANOSTRUCTURES

5.1 INTRODUCTION

The gas detection in metal oxide semiconductor sensors is due to the charge transfer between the interacting gas molecules and surface sensing layer. Yamazoe & Shimano studied the relation between the electric resistance of a semiconductor gas sensor under exposure to a target gas [1][2], with many other researches having attempted to study the theory of sensing mechanism and the influencing factors in the gas sensor's performance. Over the years a number of semiconductors gas sensors have been commercialized and most of them have followed the preparation method and assembly described by Figaro engineering Inc. [3].

There is a large number of devices readily available on the market, however, there is a huge demand for compact size, low cost and easy production, and simple measuring electronics device [4]. Macro- and microelectromechanical system do not scale down well to the nanoscale due to resolution and fabrication limitations [5][6]. Therefore, with the scaling down the sensor become ineffective at making the fine precision measurements required in many nanoscale systems. Which lead to the improvement and development of new measurement techniques of NEMS devices [7]. Although, more research is required before the fabrication of nanoscale sensing devices; there still challenges in understanding of the electrical properties of interfaces between electrodes and one dimensional material [8][9]. The size reduction from conventional to nano-size will present a significant improvement in the sensing parameters [10].

In this study CeO₂ nanoparticles prepared in a paste suspended in ethanol have been drop casted onto the interdigitated Pt electrodes on an alumina (Al₂O₃) substrate. The gas sensing properties have been determined by different analyte gases, proving that metal-oxide nanosensors can be obtained with micro-drop casting. Gas sensing analysis at room temperature were also done on samples that were calcined at different temperatures.

5.2 EXPERIMENTAL DETAILS

5.2.1 Synthesis of CeO₂ nanostructures

CeO₂ nanoparticles were grown by a hydrothermal method at 180 °C for 12 hours and detailed synthesis analyses are described in section 4.2.

5.2.2 Pt interdigitated electrode

The microstructure has a key role in the sensing response of the sensor as it regulates the currents [11][12]. Reducing the diffusion path of the analyte gas leads to an increase in concentration which improves sensitivity. Figure 5.1 is schematic diagram of an interdigitated array (IDA) electrodes, which have been use in conductometric sensors since being developed in 1970 by Taguchi [13] . The sensing material is deposited onto the IDA electrode. The actual sensing is measured when the analyte gas interact with the sensing material infused with the IDA and changing the initial resistance. The manner in which the sensing material dispersed on the IDA electrodes surface will be indirectly affect the sensitivity of the sensor, due to the diffusion of the gas. Random macroporous are created when the material is dispersed randomly on the surface of the IDA electrode and assist in the diffusion of the gas.



Figure 5.1: Microstructure of an interdigitated array electrode.

5.2.3 Depositing of nanoparticles on Pt interdigitated substrates

The CeO₂ nanoparticles were carefully mixed with organic binders (ethyl cellulose: terpineol) in mortar to form a slurry, then the resulting slurry was pasted onto the IDA electrodes (Pt on its top surface and a micro-heater on its bottom surface, see figure 5.2). The organic binder was evaporated by calcination at 180 °C, resulting in a macroporous sensor film with a good adhesion [14].

5.2.3 Fabrication and testing of the gas sensor

In order to measure the electrical response of CeO₂ based sensors, they were placed inside an air tight sensing chamber containing electrical and gas feed. Then, the response of sensors tested towards reducing gases, such as carbon monoxide (CO), methane (CH₄), ethanol and hydrogen sulphide (H₂S) at various gas concentrations ranging from 5, to 100 ppm. The sensing measurements were carried out at different operating temperatures (RT, 250, 300, 350 and 400 °C) by varying the voltage, using KSGAS6S KENOSISTEC gas testing station. The desired concentration of CO, CH₄, ethanol and H₂S gases was controlled by properly

mixing the synthetic air as a gas carrier. The Pt heater on the backside of the substrate enables the operation of the sensor at well-controlled temperatures. Electrical characterization was carried out by volt-amperometric technique; the film resistance was measured by a Keithley 3706 source meter. The gas sensor response for adopted reducing gases was calculated using the following formula: ($S=R_a/R_g$, R_a : resistance in air, R_g : resistance in analyte gas).

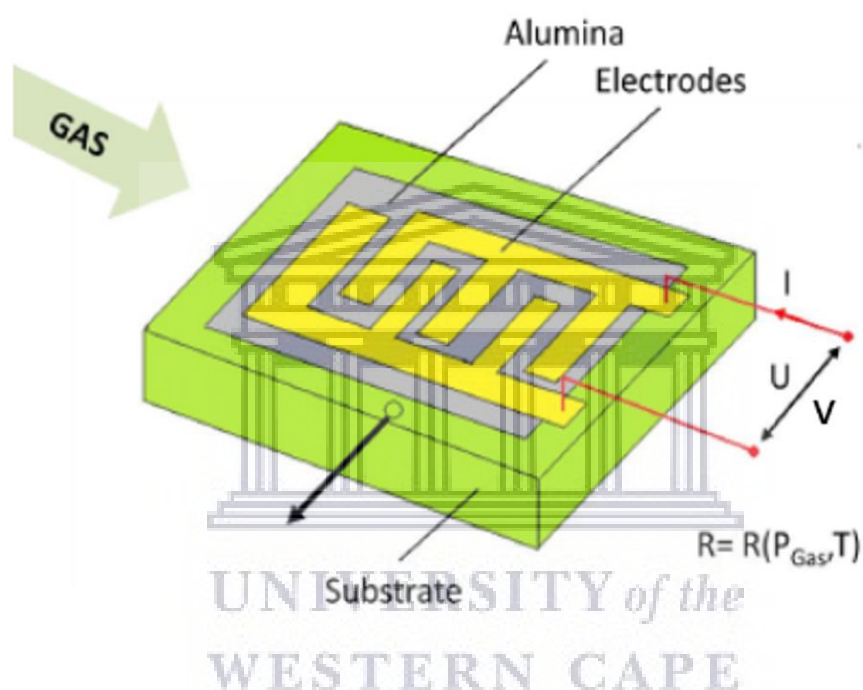


Figure 5.2: Set-up of micro reactor with interdigitated array electrodes.

5.3 RESULTS AND DISCUSSION

5.3.1 Gas sensor characteristics

In this study, we examined the optimal operating temperature of the sensing materials (CeO_2) and the maximum responses to target gases at various operating temperatures. Figure 5.3 shows the resistance in air (R_a) versus operating temperature of the CeO_2 nanostructures annealed at 300 °C. It should be pointed out that the as-prepared and those annealed at higher

operating temperatures showed no response at higher operating temperatures, hence graphs are not shown in this section. It is observed from the figure that the R_a decreases with operating temperature. At room temperature (i.e. 25 °C), R_a of 2.97Ω is noted, while it decreased to 1.19 Ω at 400 °C. Such decrease could be justified by electrons jumping to the conduction band, because of heat energy, where they move freely, and creating holes in the valence band, which also move freely.

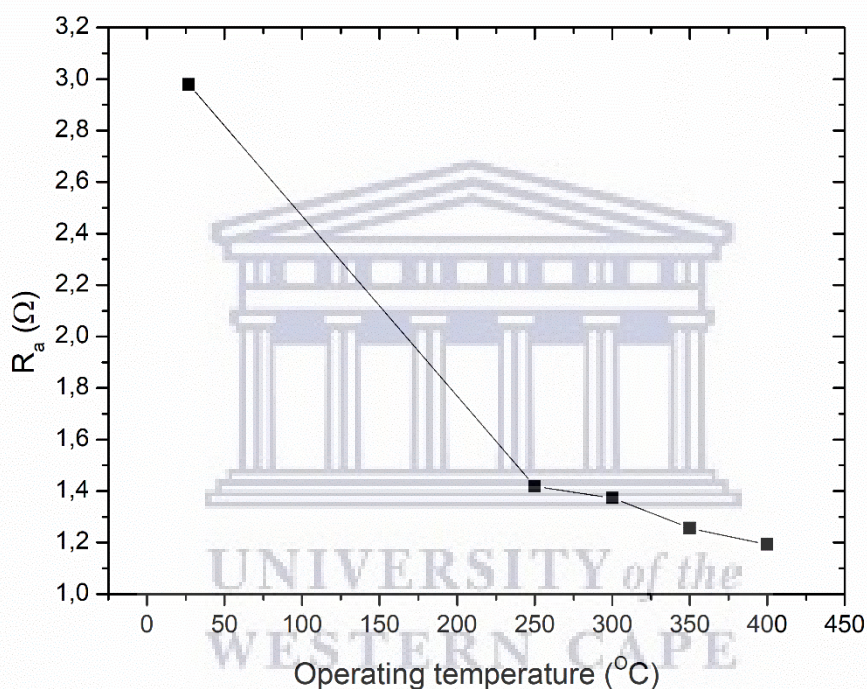


Figure 5.3: Resistance versus operating temperature of CeO₂ nanostructures.

Previous studies have shown that the sensing resistance in air of the various metal oxide based sensors decreases as the operating temperatures increases [15][16]. Although, in the current study the R_a is very small compared to that reported by previous studies [17], denoting that it could provide a significant variation in resistance when the sensor is exposed

to a target. These small resistances in air make the sensor attractive for possible device application.

For the semiconductor oxide sensors, the working temperature and gas concentrations are important factors. Figure 5.5 presents the relationship between the sensor responses towards different operating temperatures at different concentrations of methane and carbon monoxide gas. From Figure 5.5, it is observed that the CeO₂ based sensor displays improved response towards CH₄ gas (R_{air}/R_g ratio of 1028) compared to CH₄ (R_{air}/R_g ratio of 106) at RT. It is obvious that the responses of the tested sensor varied with operating temperature. In the range of RT – 400 °C, the sensor response to carbon monoxide and methane sharply decreases, signifying that their optimum temperature is 25 °C (RT). Previous studies attributed the decrease in response at higher temperatures (>25 °C) to the adsorption saturation [18][19]. This is due to the fact that as the operating temperature increases the target gas tends to be desorbed before its interacts with oxygen ions on the materials surface and thus lead to a decrease in the sensor response.



UNIVERSITY of the
WESTERN CAPE

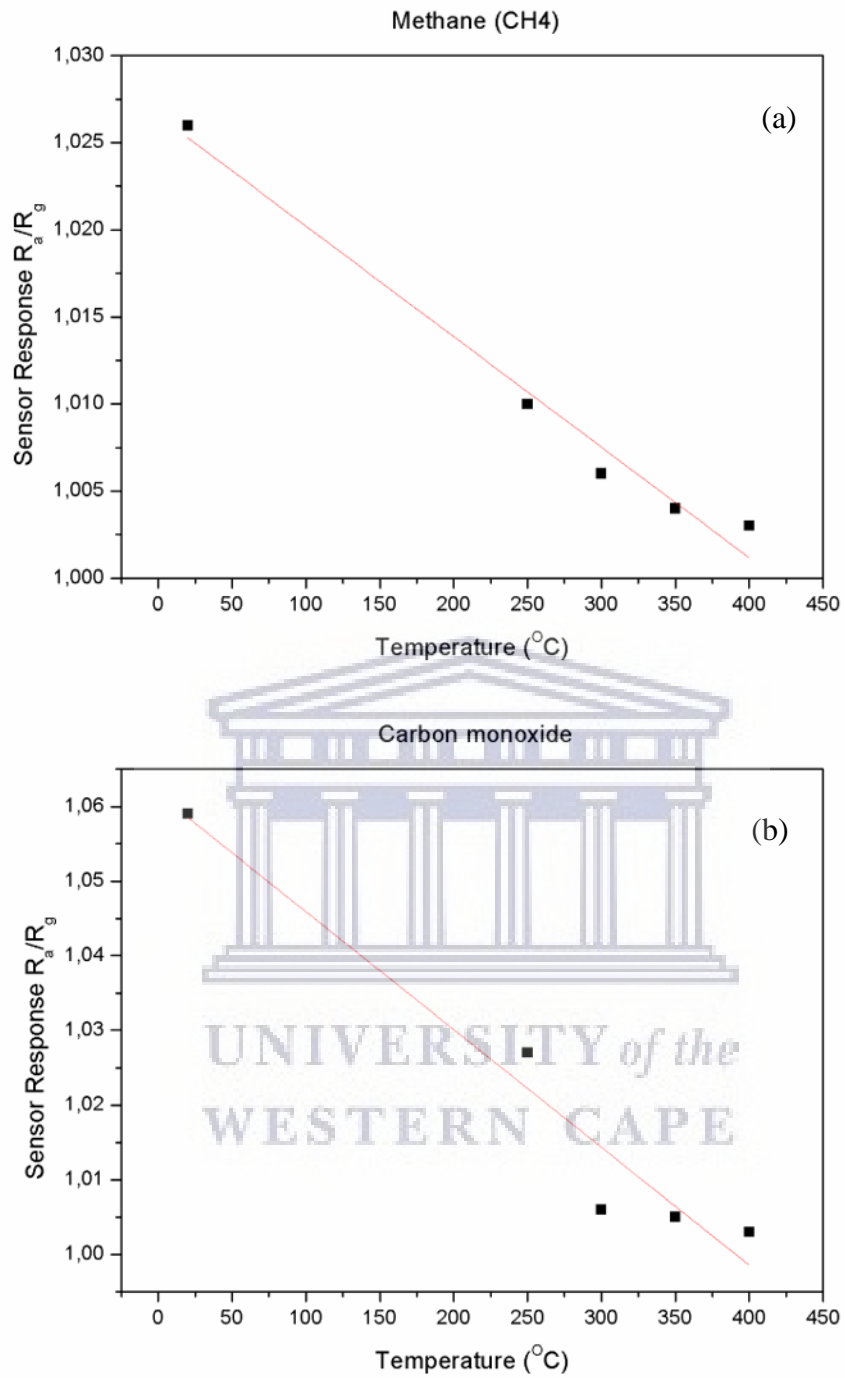


Figure 5.4: CeO₂ sensor response as a function of operating temperature after exposure to a) 40 ppm methane and b) carbon monoxide gases.

Figure 5.5 shows the real-time resistance behavior of the CeO₂ annealed at 300 °C and tested at room temperature. The graphs also indicate the different concentrations (i.e. 5-100 ppm) used during the testing of the device. It clearly shows that the sensor resistance increases when the gas is injected and further decreases when the gas is released justifying a usual behavior of an n-type metal oxide semiconductor.

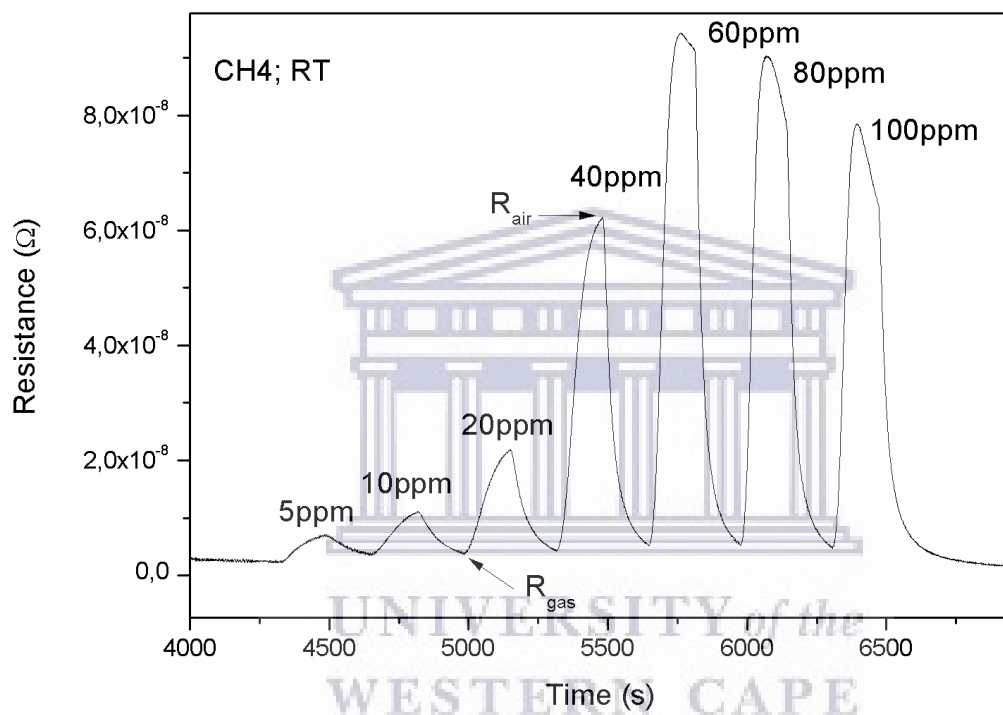


Figure 5.5: Resistance change of CeO₂ nanoparticles at RT (room temperature).

For real time application, a proper sensor should be able to respond and recover quickly without experiencing any gas poisoning. Figure 5.6 displays the response and recovery times of the CeO₂ based sensor annealed at 300 °C and measured at room temperature. It is evident from Figure 5.6 that the response time of the sensor decreases when increasing the gas concentration, while its recovery time increases with gas concentration. This is probably due

to a higher gas concentration and therefore the sensor is unable to release the adsorbed gas easily. Though, its long recovery time of roughly 240 s does not limit its possible application as a methane sensor.

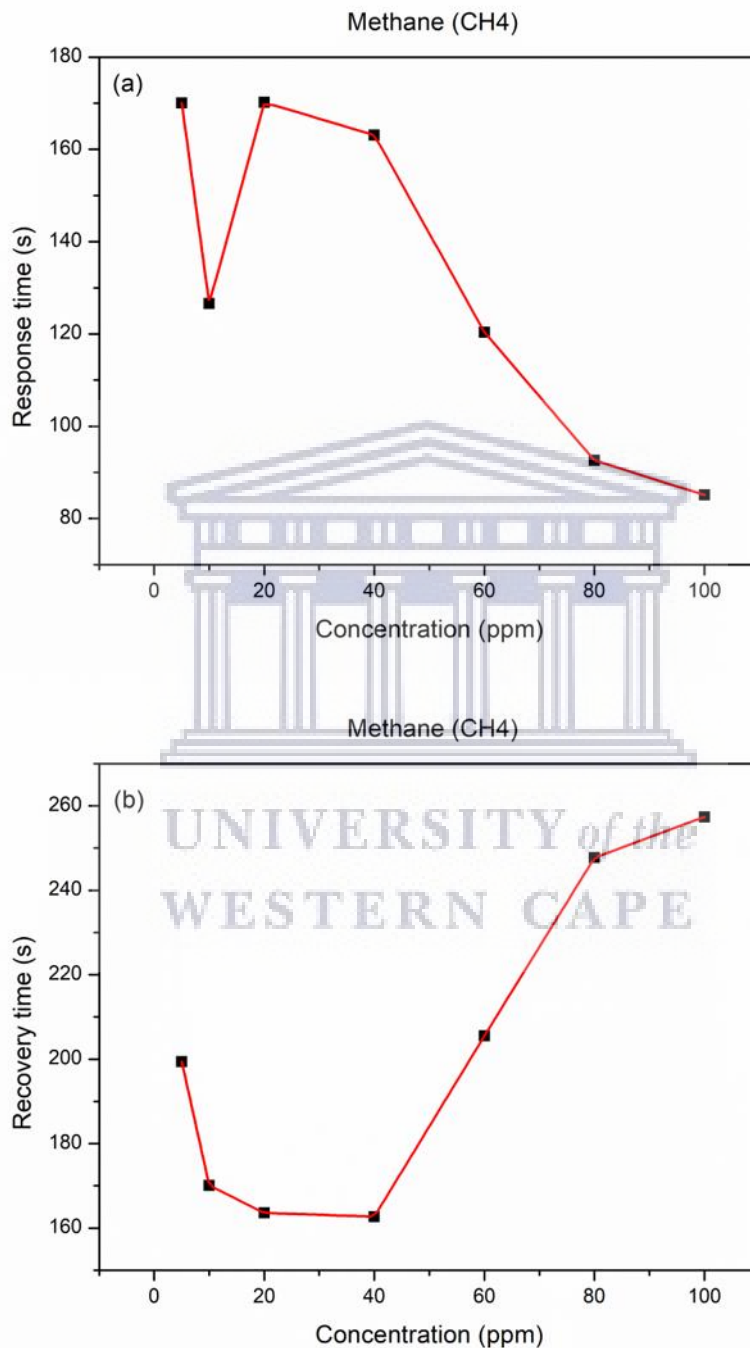


Figure 5.6: (a) response time and (b) recovery time versus CH₄ gas concentration.

The selectivity is another imperative benchmark to assess the gas sensors performance for practical applications. The response based on pure and annealed CeO₂ sensors was at 40 ppm of different test gases including ethanol, H₂S, CH₄ and CO gases at room temperature. As presented in Figure 5.7, the responses of CeO₂ annealed at 300 °C are significantly higher towards CH₄ gas in comparison to that of other gases. To be specific, the response is two times higher than other sensors, denoting that the CeO₂ based sensor annealed at 300 °C has superior selectivity to CH₄, making it a possible candidate for detection of CH₄ in mining industries. Bolokang et al. [20] and Tshabalala et el. [21] observed a similar results, where the TiO₂ based sensors showed a significant selectivity towards CH₄ at room temperature.

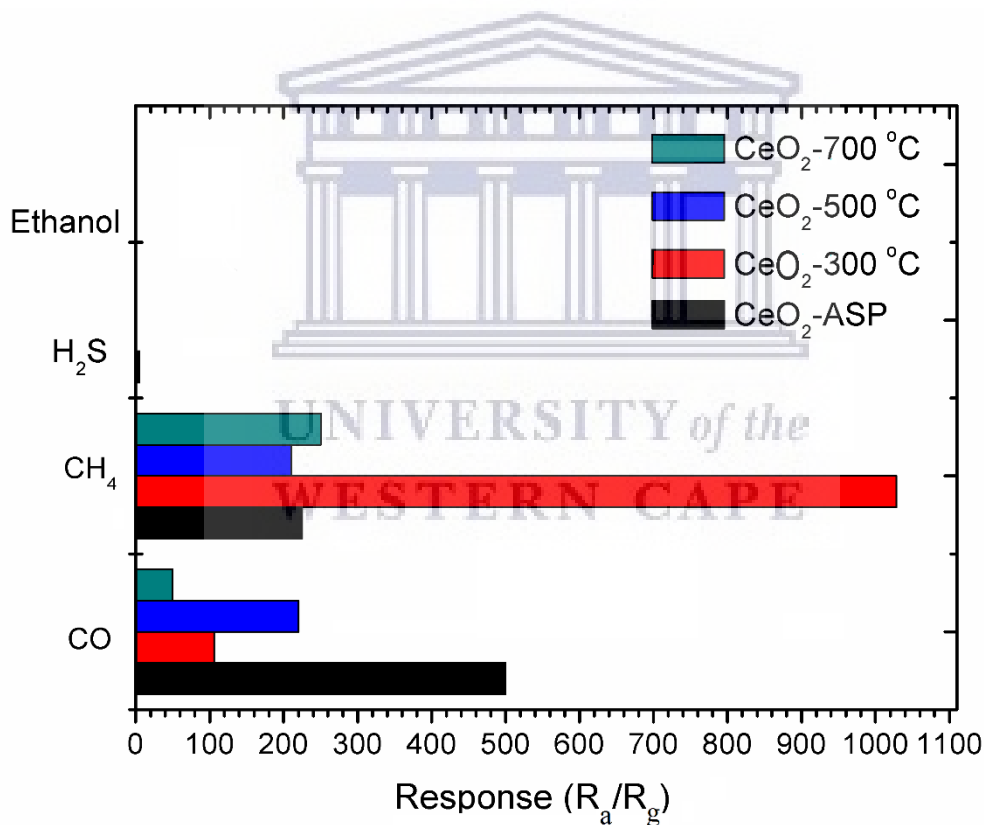
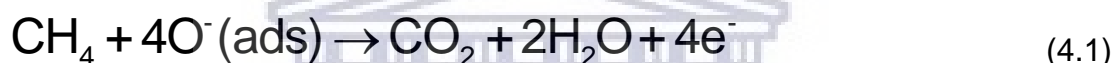


Figure 5.7: Selectivity of various CeO₂ sensors annealed at various temperatures and tested to various target gases.

5.3.2. Gas sensing mechanism

According to the literature, the sensing mechanism of semiconductor metal oxide is a surface phenomenon. Initially, upon exposing the CeO₂ sensor surface is exposed to air, the oxygen will be adsorbed on the CeO₂ surface. Then the adsorbed oxygen ions will be ionized creating, creating chemisorbed oxygen species, such as O₂⁻, O⁻ and O²⁻ on the CeO₂ surface, subject to the operating temperature. Therefore, this will result to an increase in the resistance of the sensor, because of the increasing in the electron depletion layer. Upon exposure to a reducing gas such as CH₄, a decrease in the sensor resistance will be observed. The by products, such as CO₂ and H₂O will be released, as shown in reaction of equation 4.1 [22].



5.4 CONCLUSIONS

Gas sensors were fabricated from the CeO₂ nanoparticles on the interdigitated platinum structures and tested to ethanol, H₂S, CH₄ and CO gases at various operating temperatures. Among the sensors the CeO₂ annealed at 300 °C demonstrated improved response and selectivity towards CH₄ at room temperature. Such response could be justified by improved surface area and points defects, such as oxygen vacancies, resulting to improved gas adsorption. It was further observed that the response time reduced with increased gas concentration. Thus, the finding showed that the present sensor structure can give a substantial benefit fabricating an advanced chemical gas sensor with high sensitivity and fast response and recovery times. Nonetheless, the fabrication of gas sensor devices using

nanoparticles still poses a key challenge and needs to be further developed, characterized and optimized.



5.5 REFERENCES

- [1] Yamazoe, N. and Shimanoe, K., 2008. Theory of power laws for semiconductor gas sensors. *Sensors and Actuators B: Chemical*, 128(2), pp.566-573.
- [2] Yamazoe, N., Fuchigami, J., Kishikawa, M. and Seiyama, T., 1979. Interactions of tin oxide surface with O₂, H₂O and H₂. *Surface Science*, 86, pp.335-344.
- [3] Utriainen, M., Kärpänoja, E. and Paakkanen, H., 2003. Combining miniaturized ion mobility spectrometer and metal oxide gas sensor for the fast detection of toxic chemical vapors. *Sensors and Actuators B: Chemical*, 93(1-3), pp.17-24.
- [4] Law, M., Goldberger, J. and Yang, P., 2004. Semiconductor nanowires and nanotubes. *Annu. Rev. Mater. Res.*, 34, pp.83-122.
- [5] Eranna, G., Joshi, B.C., Runthala, D.P. and Gupta, R.P., 2004. Oxide materials for development of integrated gas sensors—a comprehensive review. *Critical Reviews in Solid State and Materials Sciences*, 29(3-4), pp.111-188.
- [6] Oosthuizen, D.N., Motaung, D.E. and Swart, H.C., 2018. In depth study on the notable room-temperature NO₂ gas sensor based on CuO nanoplatelets prepared by sonochemical method: Comparison of various bases. *Sensors and Actuators B: Chemical*, 266, pp.761-772.
- [7] Wollenstein, J., Plescher, G., Kuhner, G., Bottner, H., Niemeyer, D. and Williams, D.E., 2002. Preparation, morphology, and gas-sensing behavior of Cr/sub 2-x/Ti/sub x/O/sub 3+ z/thin films on standard silicon wafers. *IEEE sensors journal*, 2(5), pp.403-408.
- [8] Darrietort, B., Pellet, C., Pibre, G. and Ayela, C., 2014. Elaboration of soft and flexible silicone stencils for the wafer-level micropatterning of polymers.

- [9] Font, J., Muntasell, J. and Cesari, E., 1999. Poly (butylene terephthalate) poly (ethylene terephthalate) mixtures formed by ball milling. *Materials research bulletin*, 34(1), pp.157-165.
- [10] Mokoena, T.P., Tshabalala, Z.P., Hillie, K.T., Swart, H.C. and Motaung, D.E., 2020. The blue luminescence of p-type NiO nanostructured material induced by defects: H₂S gas sensing characteristics at a relatively low operating temperature. *Applied Surface Science*, p.146002.
- [11] Kim, T.H., Jeong, S.Y., Moon, Y.K. and Lee, J.H., 2019. Dual-mode gas sensor for ultrasensitive and highly selective detection of xylene and toluene using Nb-doped NiO hollow spheres. *Sensors and Actuators B: Chemical*, 301, p.127140.
- [12] Oosthuizen, D.N., Motaung, D.E. and Swart, H.C., 2019. Selective detection of CO at room temperature with CuO nanoplatelets sensor for indoor air quality monitoring manifested by crystallinity. *Applied Surface Science*, 466, pp.545-553.
- [13] Jortner, J. and Rao, C.N.R., 2002. Nanostructured advanced materials. Perspectives and directions. *Pure and applied chemistry*, 74(9), pp.1491-1506.
- [14] Kortidis, I., Swart, H.C., Ray, S.S. and Motaung, D.E., 2019. Characteristics of point defects on the room temperature ferromagnetic and highly NO₂ selectivity gas sensing of p-type Mn₃O₄ nanorods. *Sensors and Actuators B: Chemical*, 285, pp.92-107.
- [15] Bolokang, A.S., Tshabalala, Z.P., Malgas, G.F., Kortidis, I., Swart, H.C. and Motaung, D.E., 2017. Room temperature ferromagnetism and CH₄ gas sensing of titanium oxynitride induced by milling and annealing. *Materials Chemistry and Physics*, 193, pp.512-523.
- [16] Tshabalala, Z.P., Shingange, K., Cummings, F.R., Ntwaeaborwa, O.M., Mhlongo, G.H. and Motaung, D.E., 2017. Ultra-sensitive and selective NH₃ room temperature

gas sensing induced by manganese-doped titanium dioxide nanoparticles. *Journal of colloid and interface science*, 504, pp.371-386.

- [17] Tshabalala, Z.P., Shingange, K., Dhonge, B.P., Ntwaeaborwa, O.M., Mhlongo, G.H. and Motaung, D.E., 2017. Fabrication of ultra-high sensitive and selective CH₄ room temperature gas sensing of TiO₂ nanorods: Detailed study on the annealing temperature. *Sensors and Actuators B: Chemical*, 238, pp.402-419.



CHAPTER 6

SUMMARY AND FUTURE WORK

6.1 SUMMARY

In this thesis, an n-type semiconducting metal oxide (Ce_2O) have been explored as potential gas-sensor material for detection of harmful inert gases. The influence of annealing on the material in order to optimize the material properties was carried out after hydrothermal synthesis process was performed. The samples were annealed at various temperatures (300,500 and 700°C). The sensing characteristics of these CeO_2 nanoparticles were studied by investigating their electrical response towards reducing analyte gases (carbon monoxide, methane, ethanol and hydrogen sulphide).

We found that highly crystalline CeO_2 nanoparticles have been successfully been synthesized by using a hydrothermal process at a growth temperature of 180°C for 12 hours and annealed at 300, 500 and 700°C. The microstructures and surface compositions of the nanoparticles were characterized by HRSEM-EDS, XRD and HRTEM. The HRSEM images show that nanoparticles are porous and agglomerates to form larger secondary particles. EDS showed that the samples are purely Ce and O with a 1:2 weight ratio. The average crystallite size is 9.4 nm and 12.8 nm, respectively for as-prepared CeO_2 nanoparticles and that calcined at 300 °C. From Raman, there is a shift and increase in the intensity of the two intrinsic defects sites upon annealing. PL shows UV emission at 410-415 nm and a green emission due to the presence of oxygen vacancy and oxygen interstitial defects at 500-650 nm. The emission intensity of the defect peak increases with the increase of annealing temperature, which indicates that the concentrations of oxygen vacancies increase with the annealing temperature

increase. The material depicted mesoporous characteristics shown by adsorption-desorption isotherm. The material is paramagnetic with very low coercivity and saturation magnetization value decreases with annealing. This is further substantiated by EPR results, the single EPR signal with a peak at 320nm is related to PM feature. And, the intensity of the peak reduces with the shift in the g-factor upon annealing.

Furthermore, gas sensors were fabricated from the CeO₂ nanoparticles on the interdigitated platinum structures and tested to ethanol, H₂S, CH₄ and CO gases at various operating temperatures. Among the sensors the CeO₂ annealed at 300 °C demonstrated improved response and selectivity towards CH₄ at room temperature, with a high sensitivity when concentration is increased. The response time decreases with high concentration as the sensor is unable to release the adsorbed gas easily, as the recovery increases with the concentration. The sensor response decrease with the increase in operating temperature due the evaporation of the analyte gas.

6.2 FUTURE WORK

From the present work on n-type semiconducting metal oxide nanostructures for gas-sensing applications, there are still many areas that have not yet been explored, which will form part of the PhD studies, such as:

- Furthermore, optimization on the synthesis of CeO₂ nanostructures through surface engineering, by forming various morphologies as to study the facet-dependent selectivity
- Incorporation of metal oxides nanocomposites as a sensing material.

- Surface modification, noble metal additives with high-effective oxidation catalytic activity can be used to enhance the sensitivity of pure metal oxides.
- Study the long-term stability of the sensor in the presence of relative humidity in order to mimic the actual environment.



UNIVERSITY *of the*
WESTERN CAPE